Realia et naturalia

DISSERTATIONES
CHIMICAE
UNIVERSITATIS
TARTUENSIS
136

KERSTI VAARMETS

Electrochemical and physical characterization of pristine and activated molybdenum carbide-derived carbon electrodes for the oxygen electroreduction reaction

TARTU ÜLIKOOL · UNIVERSITAS TARTUENSIS · 1632

DISSERTATIONES CHIMICAE UNIVERSITATIS TARTUENSIS
136

DISSERTATIONES CHIMICAE UNIVERSITATIS TARTUENSIS
136

KERSTI VAARMETS

Electrochemical and physical characterization of pristine and activated molybdenum carbide-derived carbon electrodes for the oxygen electroreduction reaction

UNIVERSITY OF TARTU
PRESS
1632

Institute of Chemistry, Faculty of Science and Technology, University of Tartu, Estonia

Dissertation is accepted for the commencement of the degree of Doctor of Philosophy in Chemistry on May 15th, 2014 by the Council of Institute of Chemistry, University of Tartu.

Supervisors: Prof. Enn Lust
Ph.D. Jaak Nerut
Institute of Chemistry, University of Tartu, Estonia

Opponent: Prof. Pawel J. Kulesza
Department of Chemistry, University of Warsaw, Poland

Commencement: June 30th, 2014 at 10:00 am
14a Ravila Str., Tartu, auditorium 1021

Publication of this dissertation is granted by University of Tartu, Estonia.

ISSN 1406-0299
ISBN 978-9949-32-597-9 (print)
ISBN 978-9949-32-598-6 (pdf)

University of Tartu Press
www.tyk.ee

To my dear supervisors Jaak and Enn

***

How needs gold, if you have Silver

TABLE OF CONTENTS

I. LIST OF PUBLICATIONS

I **K. Vaarmets**, S. Sepp, J. Nerut, E. Härk, I. Tallo, E. Lust, Electrochemical and physical characterization of Pt–Ru alloy catalyst deposited onto microporous–mesoporous carbon support derived from Mo_2C at 600 °C, Journal of Solid State Electrochemistry 17 (2013) 1729–1741.

II **K. Vaarmets**, J. Nerut, E. Härk, E. Lust, Electrochemical and physical characterisation of Pt-nanocluster activated molybdenum carbide-derived carbon electrodes, Electrochimica Acta 104 (2013) 216–227.

III E. Lust, **K. Vaarmets**, J. Nerut, I. Tallo, H. Kurgi, P.Valk, E. Härk, Influence of specific surface area and microporosity-mesoporosity of pristine and Pt-nanoclusters modified carbide-derived carbon electrodes on the oxygen electroreduction, Electrochimica Acta (2014) DOI:10.1016/j.electacta.2014.04.054.

Author's contribution

Paper I: The author performed the electrochemical measurements. The author participated in the analysis of data and writing the papers.

Paper II: The author performed the electrochemical measurements. The author participated in the analysis of data and writing the papers

Paper III: The author performed the electrochemical measurements. The author participated in the analysis of data and writing the papers.

2. ABBREVIATIONS AND SYMBOLS

ABBREVIATIONS

2D – second-order peak of D-band
AC – alternating current
AFC – alkaline fuel cell
BDD – boron doped diamond
BET – Brunauer-Emmett-Teller
B-MWCNT – bamboo multi walled carbon nanotube
BPPG – basal plane pyrolytic graphite
C(Mo_2C) – carbon synthesized from Mo_2C
C(TiC) – carbon synthesized from TiC
CDCs – carbide-derived carbons
CV – cyclic voltammetry method
CVs – cyclic voltammograms
D – disordered-induced peak in Raman spectra
DMFC – direct methanol fuel cell
EDL – electrical double layer
EELS – electron energy loss spectroscopy
EIS – electrochemical impedance spectroscopy
EPPG – edge plane pyrolytic graphite
FC – fuel cell
G – graphitic Raman peak
GAI – generalized adsorption isotherm
GC – glassy carbon
GCDE – glassy carbon disk electrode
H-MWCNT – hollow multi walled carbon nanotube
HOPG – highly oriented pyrolytic graphite
HRTEM – high resolution transmission electron microscopy
MCFC – molten carbonate fuel cell
MSE – $Hg|Hg_2SO_4|K_2SO_4$ (sat.) reference electrode
NHE – normal hydrogen electrode
NLDFT – non-local density functional theory
OMC – ordered mesoporous carbon
OPG – ordinary pyrolytic graphite
ORR – oxygen electroreduction
PAFC – phosphoric acid fuel cell
PEMFC – polymer electrolyte membrane fuel cell
RDE – rotating disk electrode
RHE – reversible hydrogen electrode
SAED – selected area electron diffraction
SAPG – stress-annealed pyrolytic graphite
SEM-EDX – scanning electron microscopy with energy-dispersive X-ray spectroscopy

SHE – standard hydrogen electrode
SOFC – solid oxide fuel cell
SWCNT – single walled carbon nanotube
TEM – transmission electron microscopy
XPS – X-ray photoelectron spectroscopy
XRD – X-ray diffraction method
XRF – X-ray fluorescence method

ROMAN SYMBOLS

A – flat cross-section (geometric) surface area of the electrode
a – lattice parameter from XRD data
A_{CS} – molecular cross-section area of adsorbate (0.162 nm^2 for N_2 at 77 K)
b – slope of the Tafel plot
c – constant in BET theory describing the adsorbent-adsorbate interactions
c_O^b – concentration of oxidized species in the bulk solution
$c_{O_2}^b$ – concentration of O_2 in the bulk solution (1.3×10^{-6} mol cm^{-3} in 0.5 M H_2SO_4 at 25 °C)
C – capacitance
C_{ad} – adsorption capacitance
C_{CV} – capacitance calculated from CV data
C_d – differential capacity of double layer
C_{dl} – double layer capacitance
C_{far} – faradaic capacitance
C_p – parallel capacitance
C_s – series capacitance
$C(\lambda)$ – wavelength dependent parameter ($C \approx C_0 + \lambda C_1$, where $C_0 = -12.6$ nm and $C_1 = 0.033$)
c_f – O_2 concentration in the Nafion® film
d – Pt crystallite size calculated by Scherrer method (Pt(220) reflection) from XRD data
D_f – O_2 diffusion coefficient in the Nafion® film
D_O – diffusion coefficient of substance O
D_{O_2} – diffusion coefficient for O_2 (1.8×10^{-5} cm^2 s^{-1} in 0.5 M H_2SO_4 at 25 °C)
$E(t)$ – AC voltage as a function of time
E_0 – amplitude of the sinusoidal voltage
E – potential
$E_{½}$ – half-wave potential
ECA – electrochemically active surface area
E_{eq} – equilibrium potential
$E^{\circ\prime}$ – formal potential

E_{ox} – peak potential of oxidation reaction
E_p – peak potential
E_{red} – peak potential of reduction reaction
f – AC frequency
F – Faraday constant (96490 C mol^{-1})
f – number of disk revolutions per second
$f(W)$ – pore size distribution function
I_D – heights or integrated intensity of the D-peak
I_G – heights or integrated intensity of the G-peak
I – current
$I(t)$ – AC current as a function of time
I_0 – amplitude of the sinusoidal current
I_C – capacitive current
I_f – faradic current
I_p – peak current
j – current density
j_c – ORR current densities corrected for Ar-saturated electrolyte data
j_{cat} – cathodic current density
j_D – diffusion step limited charge transfer current density
j_f – current density in the Nafion® film
j_K – kinetic current density
K – constant in the Scherrer equation ($K = 0.93$)
k_0 – rate constant
k_{het} – electrochemical rate constant for ORR
L – linear dimension of particle
L_a – in-plane correlation length
L_f – Nafion® film thickness
m – mass of adsorbent
M – molar mass of adsorbate
n – number of electrons transferred per electroreduction of one O_2 molecule
n^* – total number of electrons transferred
$N(P/P_0)$ – experimental adsorption isotherm
$N(P/P_0, W)$ – kernel of the theoretical isotherms in the pores with different widths
n' – number of electrons transferred in rate determining step
N_A – Avogadro constant ($6.023 \cdot 10^{23}$ molecules per mole)
O – oxidized species
P – pressure
P/P_0 – relative pressure
Q_{cal} – calculated charge required for hydrogen adsorption from the Pt surface
$Q_{Pt\text{-}poly}$ – polycrystalline Pt surface (210 μC cm^{-2})

R – ideal gas constant (8.314 J mol^{-1} K^{-1})
R – reduced species
R_P – parallel resistance
R_S – series resistance
S_{BET} – specific surface area
S_{ext} – external surface area
S_{meso} – mesoporous area
S_{micro} – microporous area
T – temperature
t_{stat} – statistical thickness of the adsorbed layer
t_{synt} – synthesis temperatures
v – kinematic viscosity of the solution (0.01 cm^2 s^{-1} in H_2O at 20 °C)
V_{ads} – volume of adsorbate
V_{meso} – mesoporous volume
V_{micro} – microporous volume
V_{molar} – molar volume of adsorbate (34.7 cm^3 mol^{-1} for N_2 at 77 K)
V_{tot} – total pore volume
W – mass of gas adsorbed at relative pressure
W – pore width
W_m – mass of gas absorbed in monolayer
Z – impedance
$|Z|$ – magnitude of impedance
Z' – real part of the impedance
Z'' – imaginary part of the impedance

GREEK SYMBOLS
α_c – cathodic transfer coefficient
θ – phase difference between the voltage and the current
λ – X-rays wave-length
$\chi/2$ – Bragg angle ($\theta = \chi/2$)
ω – angular velocity of rotation ($\omega=2\pi f$)
v – potential scan rate

3. INTRODUCTION

Fuel cell (FC) is an electrochemical device that converts chemical energy in fuels directly into electrical and heat energy with high efficiency and low emission of pollutants. Typical reactants for FC are hydrogen and oxygen. FC consists of an electrolyte layer in contact with an anode and a cathode on either side. Hydrogen oxidizes electrochemically at the anode and the oxygen electro-reduction (ORR) occurs at the cathode. [1–4] The electrochemical reactions occur on the surface of the catalyst, which usually is platinum nanoparticles supported onto the porous carbon. To minimize the use of platinum in the catalyst layer and through that the cost of a FC, it is important to design a catalyst structure, which has small Pt-nanoparticles (4 nm or smaller) with large surface area finely dispersed at the porous surface of the catalyst support (1.0…4.0 mg Pt cm^{-2}).

Various carbon materials, e.g. carbon black, carbon nanotubes, pyrolytic and highly orientated pyrolytic graphite, boron-doped diamond, etc. have been studied to improve the performance of ORR. Influence of the porous carbon support on the ORR kinetics has been extensively studied, but there are only very little data discussing the ORR at microporous-mesoporous carbon materials with exact pore size distribution and well-defined hierarchical structure. The porous carbide-derived carbons (CDCs) have tuneable specific surface area, micro- and mesoporosity, good electrical conductivity and corrosion stability at the positive electrode potentials, which are perfect properties for a catalyst support material. Typical support material for FC is Vulcan® XC72 (produced by Cabot), which has low specific surface area, S_{BET}, 240 m^2g^{-1} and moderate mesoporous volume, V_{meso}, 90 m^2g^{-1} [5]. The CDCs materials have high S_{BET} > 940 m^2g^{-1} and V_{meso} > 160 m^2g^{-1} values, being probably very promising support material.

For this work the CDCs were prepared from Mo_2C (noted as C(Mo_2C)) at six different fixed chlorination temperatures from 600 °C to 1000 °C and the main aim of this work was to study the influence of the micro- and mesoporosity, pore size distribution and crystallinity (amount of amorphous and graphitic layers) of different pristine C(Mo_2C) and Pt-nanoclusters activated composite Pt-C(Mo_2C) and Pt-Ru alloy nanoclusters activated Pt-Ru-C(Mo_2C) electrode materials on the ORR kinetics in 0.5 M H_2SO_4 solution at 22 ± 1°C.

4. LITERATURE OVERVIEW

4.1 Fuel Cells

Fuel cells are electrochemical devices that convert chemical energy storaged in fuels into electrical and heat energy with high efficiency and low environmental impact. The intermediate step of producing mechanical work, typical of most conventional power generation methods, is avoided, and thus, FCs are not limited by the thermodynamic limitations of the heat engines such as the Carnot cycle efficiency. FCs generate electricity in single step without involving any moving parts and with minimal generation of pollutants [1–4]. Typical reactants for FCs are hydrogen and oxygen, neither has to be in its pure form. Hydrogen may be present either in a mixture with other gases (CO_2, N_2 and CO) or as the gaseous hydrocarbons (e.g. CH_4) or in liquid hydrocarbons (e.g. CH_3OH, CH_2OH_5, etc.). Ambient air contains enough oxygen to be used in FCs. However, FCs generates by-products − heat and pure water (if H_2 is used as fuel) [1], applicable for modern technological systems.

The first observation of a FC was made by C.F. Schönbein in 1838 and based on this work the first FC was demonstrated by Sir W. Grove in 1839. In 1842, Grove developed the first primitive FC, which produced electrical energy by combining hydrogen and oxygen. Since 1896, W.F. Ostwald provided many theoretical understandings of how FC operates. He realized that energy conversion in combustion engines is limited by the Carnot cycle efficiency and FCs are highly efficient, silent devices and generate no pollution if H_2 is used as fuel. Thus, F.T. Bacon started working on practical FC in 1932 and completed construction and evaluation of a 5 kW FC stack in 1952. It took more than 100 years from Grove´s invention of the FC to make a practical effectively working device.

The first practical FC applications were initiated by the development of the U.S. space program. General Electric developed the first polymer membrane fuel cell (PEMFC), which was used in the Gemini Program in the early 1960s. They continued to use the FCs in space to generate electricity for life support, guidance, and communications. First FC-powered van came in the mid-1960s; first PEMFC-powered submarine in 1989; first FC-powered bus and first passenger car running on PEMFC in 1993.[1]

The basic physical structure of a FC is simple and it consists of an electrolyte layer in contact with an anode and a cathode electrodes on either side. In a typical FC, fuel is fed continuously to the anode (positively polarized electrode) and an oxidant (oxygen, air) is fed continuously to the cathode (negatively polarized electrode). The electrochemical reactions occur at the electrodes to produce an electric current through the external circuit, while driving a complementary electric current that performs work on the load. Thus, in principle, FC produces power as long as fuel and oxygen are supplied[2].

FCs can be classified according to the choice of electrolyte and fuel used, which in turn determines the electrode reaction occurring on an anode and the type of ions that carry the current across the electrolyte, and includes alkaline FC (AFC), polymer electrolyte membrane or proton exchange membrane FC (PEMFC), phosphoric acid FC (PAFC), molten carbonate FC (MCFC) and solid oxide FC (SOFC) [1–3]. The operating temperature and long lasting durability of a FC dictate the physicochemical and thermo mechanical properties of materials used in the FC components, i.e. electrodes, electrolyte, interconnects, current collectors, etc.. PEMFCs are limited to temperature of about 80–90 °C and AFC and PAFC are working up to 220 °C [2]. The Fig. 1 provides an overview of the basic principles and electrochemical reactions in the main FCs types.

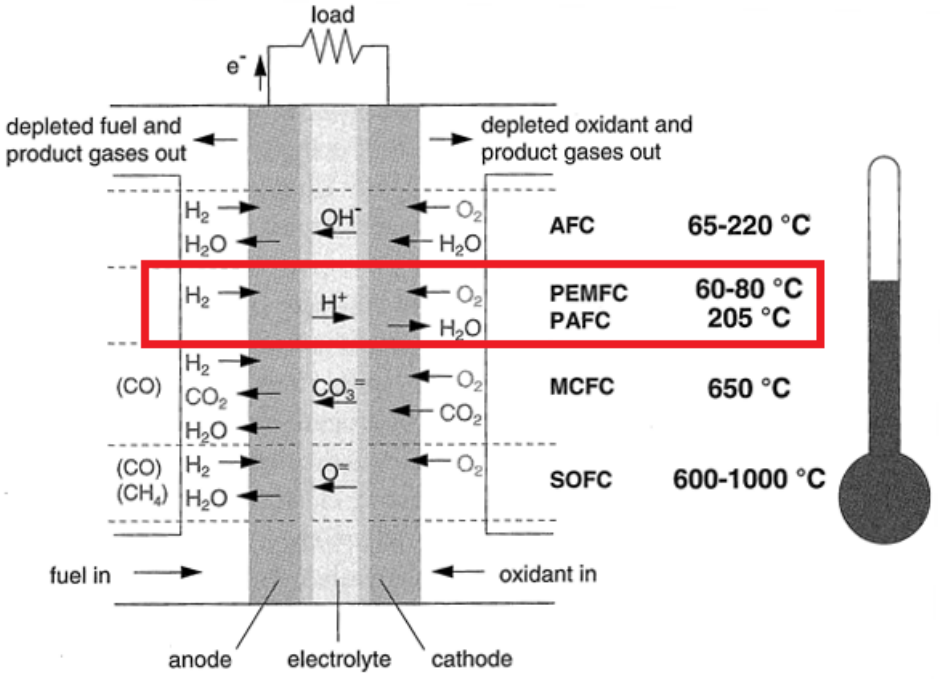

Figure 1. Types of fuel cells, their reactions, and operating temperatures [1].

In a common PEMFC, the electrolyte is a thin (<50 μm) proton conductive polymer (Nafion® – fluorinated sulfonic acid or other similar polymer) membrane. Typically, the catalyst layer consists of platinum particles supported on porous carbon. A schematic diagram of cell configuration and basic operating principles are shown in Fig. 2. The only liquid in the PEMFC is water and the corrosion problem is minimal. However, in the operating system, it is very important to keep the membrane hydrated, so it should be controlled that the by-product water does not evaporate faster than it is produced. The operating temperature is usually between 60 and 80 °C, allowing for faster

startup compared with other FCs. In a PEMFC the suitable fuel is pure hydrogen, which assumes conversion of fuels such as natural gas or other hydrocarbons. An implementation of the PEMFC enables the direct use of methanol without a fuel reform. Direct methanol FC (DMFC) use as oxidation catalyst the Pt-Ru alloy supported on the porous carbons. During some decades, the main focus of development of PEMFC has been on the small-scale distributed stationary power generation, but now the focus has been shifted on automotive and portable applications. [1–3]

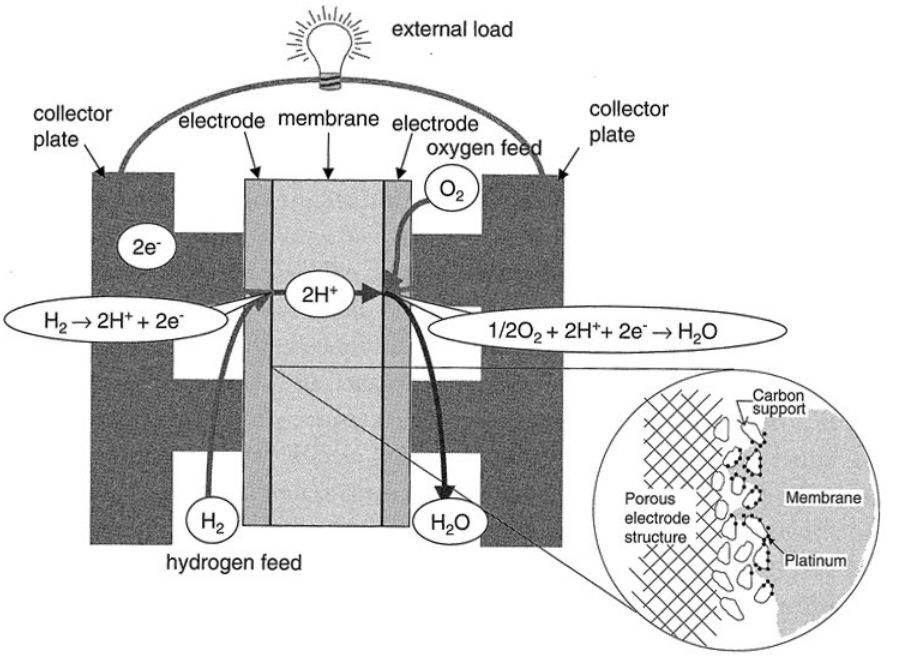

Figure 2. The basic principle of operation of PEMFC [1].

The main advantages of a PEMFC are: high fuel conversion efficiency (34–36%), low or zero emission of residuals (if H_2 is used as a fuel), rapid start-up, capable for generation of high current and power densities (2 kW dm^{-3} and 2 W cm^{-2}), long life, no moving parts and therefore quiet operation. Although, there are many significant future challenges in PEMFC design and development such as thermal and water management and sensitivity to poisoning by CO, sulphur containing components/species, as well as with NH_3. Those disadvantages decrease the operating current density and for the compensation of the lost current density additional electrode catalyst loading is inevitable, however, increasing the cost of the PEMFC system. Finally, to cross the barrier to commercialization, the development of hydrogen infrastructure needs great investments. [1–3]

4.2 Oxygen electroreduction reaction

4.2.1 The general scheme of oxygen electroreduction

The mechanism and kinetics of the cathodic ORR are functions of many experimental parameters, including the chemical composition of the cathode, electrolyte and its pH, and most importantly the electrode potential. Proposed hypothetical reaction pathways, rather than detailed reaction mechanisms, are based on data obtained by a rotating disk and ring-disk methods that enables the quantitative determination of some reaction intermediates. ORR is a multi-electron transfer reaction, which reaction mechanisms consist of several elementary steps involving various serial and/or parallel pathways. The ORR in aqueous solutions may proceed by two overall pathways: a ´direct´ four-electron electroreduction to H_2O or a 'peroxide' pathway, which involves formation of H_2O_2 as the stable intermediate product. In acidic solution:
the 'direct' four-electron pathway can be summarised as:

$$\mathbf{O_2 + 4H^+ + 4e^- \rightarrow 2H_2O} \qquad E_0 = 1.229 \text{ V vs. normal hydrogen electrode (NHE),}$$

the peroxide pathway as:

$$\mathbf{O_2 + 2H^+ + 2e^- \rightarrow H_2O_2} \qquad E_0 = 0.67 \text{ V vs. NHE,}$$

followed by either the reduction of peroxide:

$$\mathbf{H_2O_2 + 2H^+ + 2e^- \rightarrow 2H_2O} \qquad E_0 = 1.77 \text{ V vs. NHE,}$$

or by the decomposition of peroxide as:

$\mathbf{H_2O_2 \rightarrow 2H_2O + O_2}$ [6–9].

The 'direct' four-electron pathway includes a number of steps in which O_2 is reduced to OH^- and finally to H_2O. The reduction steps may include an absorbed peroxide intermediates, which are not present in solution phase. In the case of the peroxide pathway the peroxide species are probably located in the solution [7]. Thus, the cathode surface must be at the same time a good electron transfer catalyst and also a good peroxide decomposing catalyst. The first pathway appears to be predominate on noble-metal electrocatalyst, e.g. on Pt, and the second pathway on different carbons including graphite [7].

4.2.2 Oxygen electroreduction on carbon electrodes

Recent studies have revealed that the physical properties of the carbon support influence the electrochemical performance, durability and efficiency of the FC. In the reviews by Antolini [10] and Sharma and Pollet [11], it was emphasized that an ideal support should have the high surface area, versatility in porosity, good electrical conductivity, good mechanical and electrical catalyst-support interaction, good corrosion resistance and most importantly – low cost. It has been reported [10,11] that carbon materials with high surface area and good crystallinity can provide a high dispersion of Pt-nanoparticles and facilitate the electron transfer step. Many authors [12–15] have concluded that the activity of a catalyst increases as the 'effective' reaction surface area of the catalyst increases. Thus, the catalyst particles should be reduced in the diameter to increase the effective electrochemically surface area. However, it has to be taken into account that sometimes the specific activity of the metal nanoparticles can decrease with the decrease of the particle size (known as the particle-size effect) [12–14,16]. Therefore, the catalysts are supported on high surface area substrates. Carbon supports should have a high percentage of mesopores in the 20–40 nm region to provide the accessibility of the reactants (e.g. monomeric units of the Nafion® ionomer) to the catalytic site and also the quick removal of the products.

Various carbon supports (carbon black, pyrolytic graphite, amorphous carbon, single walled and multi walled carbon nanotubes, carbon nanofibers, etc.) have been used during long-lasting catalyst support optimization studies. Yeager et al. [17] found that the ORR rate on the stress-annealed pyrolytic graphite (SAPG) in alkaline solution is much lower than on ordinary pyrolytic graphite (OPG). SAPG is a highly ordered form of graphite, and its basal plane approaches to the atom arrangement of the basal plane of graphite. The ORR on graphite electrodes arises from an interaction of O_2 with functional (quinone, phenol, etc.) groups existing on the carbon surface. It is assumed that the quinone groups are mainly responsible for the ORR on carbon surface [18] and modification of the basal plane with different quinones increases the activity of ORR [17]. Gara and Compton [19] preformed the ORR measurements in 0.1 M H_2SO_4 solution on a variety of carbon substrates: glassy carbon (GC), edge plane pyrolytic graphite (EPPG), basal plane pyrolytic graphite (BPPG) and boron doped diamond (BDD), and single walled (SWCNT), bamboo multi walled (B-MWCNT) and hollow multi walled (H-MWCNT) carbon nanotube modified BPPG. They concluded that the substrates with a large number of edge plane sites have a higher activity towards ORR and therefore a higher tendency to produce H_2O_2 if used as a catalyst support in a PEMFC. Thus, it is favourable to decrease the number of edge plane sites in carbon catalyst supports for PEMFC applications in order to increase ORR efficiency and reduce the membrane degradation from H_2O_2 attack [19].

There are only limited data regarding the ORR at the well-defined carbide-derived carbons. In the work of Schlange et al. [20] the TiC derived carbon,

noted as C(TiC), was used as catalyst support for DMFC application. The study showed that C(TiC) supported noble metal catalysts show 18% better performance during fuel cell application than a commercial catalyst, even without optimization of the catalyst and support parameters for ORR. They suggested that this improvement can be related to a higher surface area of C(TiC), the good catalysts dispersion, the smaller Pt particles sizes compared to that for commercial catalyst and the more graphitic ordering of C(TiC) reducing the electrical resistance of the electrode layers.

CDC and some ordered mesoporous carbon (OMC) have comparable properties, e.g. controllable pore size, high surface area (up to 1800 $m^2\ g^{-1}$) and very large pore volume and high conductivity [21–23]. Additionally, OMCs enables efficient diffusion of hydrogen to the active sites. Moreover, OMC have some surface oxygen groups which are considered to improve the interaction between the metal catalyst and the carbon support allowing better dispersion of the catalyst particles [11,24].

Based on the comparison of different carbon materials it may be concluded that the best replacement for commercial carbon black can be OMC and carbon gels. In the same conditions those materials allow high dispersion of metal particles and good reactant flux, showed higher catalytic activity and thermal stability[11,24].

4.2.3 Oxygen electroreduction on platinum electrodes

The kinetics of ORR has been thoroughly studied on platinum electrodes in acidic solutions [16,25]. Platinum appears to be the most active noble metal for ORR [7].

Marković and co-workers demonstrated a noticeable dependence of the ORR activity on the crystallographic orientation of the platinum electrode surface in 0.1 M $HClO_4$ solution. The activity for ORR discerned from the half-wave potential values decreases in the order: Pt(110) > Pt(111) > Pt(100). The reaction proceeds on all well-ordered low index planes with exchange of four electrons per O_2 molecule. Tafel slopes of −120 mV per decade at high current densities and −60 mV per decade at low current densities were found for all three low-index Pt planes at room temperature. Oxygen-containing species chemisorbed on platinum appear to be the cause of the change in the Tafel slope. [25]

Paulus et. al [26] demonstrated that the diffusion resistance of the thin Nafion® film used to fix the catalyst particles to the carbon substrate is negligible, i.e. the kinetic current densities can be determined directly from the measured currents without extensive mathematical modeling. The higher activities in PEMFCs and a clearly higher activity measured in their work on a thin film RDE in 0.5 M $HClO_4$ point to a significant anion adsorption effect in 0.5 M H_2SO_4 as well as to possible enhancing effects of the higher oxygen solubility in Nafion® electrolytes [26].

Similar study on the ORR on platinum doped CDC materials in 0.1 M $HClO_4$ solution was made by Kaskel et. al [27], who proved that the Pt-CDC material is a promising alternative support material for fuel cell cathode catalysts. The observed Pt mass (12 wt.%) and specific activities, as well as the electrochemically active surface area (66 ± 4 m^2 Pt g^{-1}) are higher or comparable to those of commercial state-of-art Pt/carbon catalysts with conventional carbon black materials. The in situ incorporation of Pt nanoparticles into the carbon framework offer significant advantages for the long-term stability and corrosion resistance.

Corti et. al [28] investigated the correlation between catalytic activity and size of the platinum nanoparticles deposited onto the carbon black by different methods. The catalysts prepared by reduction with formic acid and ethylene glycol (microwave-assisted) show electrochemical activities very close to those of the commercial catalyst, and are almost insensitive to the Pt dispersion or Pt particle size.

4.2.4 Oxygen electroreduction on platinum-ruthenium binary catalysts

Studies in acidic solutions have revealed that physical properties (particle size and crystallinity) and chemical composition of Pt and Pt-based binary catalysts (Pt-Ru [29–31] and Pd-Ru [32] in 1.0 M H_2SO_4 solution) and Pt-Ru based transition metal ternary catalysts (Pt-Ru-Ni [33] and Pt-Ru-Co [34] in acidic solution), Pt based transition metal ternary catalysts (Pt-Co-Cr [35,36] in acidic media and Pt-V-Fe [37] and Pt-Co-Cu [35] (pH has not been discussed) and transition metal oxides (Pt-CoO-Cr_2O_3 [37]), deposited onto different carbon supports, can greatly influence ORR rate and fuel oxidation kinetics, and thus, the power and energy densities of PEMFCs [24,38,39]. Ternary catalysts demonstrate even higher electrochemical activity than Pt-based binary catalysts. Very important aspect of using the Pt-based transition metal binary [29–32] and ternary catalysts [35,36] is prevailing the 'four electron' pathway for ORR.

Several studies of ORR on polycrystalline (PC) Ru, monocrystalline Ru(*hklf*), Pt submonolayers on Ru, and Pt-Ru/C composite electrodes, conducted by Adžić et al., have shown considerable activity of these catalysts for ORR in alkaline [40] and acidic (mainly in 0.1 M $HClO_4$) [41–43] solutions. ORR on a PC Ru in acidic solution has been found to proceed through a 'parallel' mechanism with a series pathways being predominant and with the exchange of approximately four electrons. ORR rate shows strong dependence on the oxidation state of the Ru/RuO_x surface [40]. In alkaline solutions ORR also proceeds through a 'parallel' mechanism, which kinetics strongly depend on the thickness of an oxide layer. The slopes of the Tafel plots higher than 120 mV dec^{-1} have been observed because formation of $Ru(OH)_x$ takes place [41]. Additionally to 120 mV dec^{-1} slope, ill-defined larger Tafel slope values of 220–250 mV dec^{-1} were observed for Ru(0001) and Ru(10$\bar{1}$0) in

0.1 M $HClO_4$ solution at potentials less positive than 0.75 V (vs. standard hydrogen electrode (SHE)) [41]. Even a slope of 400 mV dec^{-1} has been observed by Climent et al. [44] for ORR on a Pd monolayer deposited onto Pt(111), ascribed to the rate determining step involving molecular O_2 adsorption. The use of Ru as a substrate for Pt is attractive because it may cause a change in d-band electron vacancies [45,46] and d-band center positions [47] that can enhance the ORR kinetics [42].

Carbon supported Se-modified Ru-Mo catalysts for ORR in acidic media have been synthesised and studied by Wieckowski et al. [48]. It was found that small additions of Mo into Se-Ru catalysts minimise the dissolution of the electrode in acidic media. The Se-Ru-Mo catalysts showed excellent O_2 reduction activities even after cycling the cathode 1000 times between 0.7 and 0.9 V (vs. reversible H_2 electrode (RHE)).

Pt-Ru-Mo-C ternary catalysts [49] for DMFCs have been studied in acidic media and it was found that all ternary Pt-Ru-Mo-C catalysts were more active toward CO and CH_3OH oxidation than binary Pt-Ru [49] or Pt-Mo [10,50] catalysts. Favourable electronic effects have been suggested by density functional theory [51–53], which has shown that the CO adsorption energy is the lowest on a Pt monolayer deposited onto Ru, compared with Pt, Ru and mixed Pt-Ru surface layer on Pt. The proposed bi-functional mechanism [54] suggests that Ru sites provide an active surface for oxidative removal of adsorbed CO from the neighboring Pt sites.

Data for the Gibbs energy of formation of RuO_2 enabled deriving a standard potential value of 0.43 V (vs. SHE) for the process

$$RuO_2 + 4H^+ + 4\bar{e} = Ru + 2H_2O, \quad (1)$$

but this is not the stationary potential observed in acid media [55]. Under CV conditions applied, RuO_2 is certainly not reduced back to the metallic state in the negative going potential sweep to 0.05 V. So, the process under discussion seems to be irrelevant to the experimental conditions [55,56]. A thermodynamic point of interest is the initial rest potential of ruthenium(IV) oxide in aqueous acidic medium, which can be interpreted in terms of the half-cell reaction (2)

$$2RuO_2 + 2H^+ + 2\bar{e} = Ru_2O_3 + H_2O, \quad (2)$$

reported as 0.94 V (vs. RHE) [55]. Trasatti et al. [57] measured potentiostatically the quasi stationary potential setup at RuO_2 films under small polarization. However, at the open circuit conditions, time dependent self-discharge and recovery potentials are observed, which eventually approach to ~0.75 V in acidic solutions [58,59]. In the case of Ru/RuO_2 electrode surface films, the process

$$RuO_2 + H^+ + 4\bar{e} = Ru{\cdot}O{\cdot}OH, \quad (3)$$

may be a preferred representation for the singular rest potential [55]. For thicker RuO_2 films, the following reaction scheme has been proposed [59]

$$RuO_x(OH)_4 + \delta H^+ + \delta\bar{e} = RuO_{x-\delta}OH_{y-\delta}, \quad (4)$$

attributed to the less accessible inner surface region of oxide that progressively becomes excluded as the redox reaction is driven to higher rates at large potential and scan rate. Similar effect can be proposed for Pt-Ru clusters, deposited inside of the microporous-mesoporous of $C(Mo_2C)$ support.

It should be noted that at Pt, Rh and Au, the thick oxide films (~40 layers of oxide for Pt) can also be formed by potential cycling over a restricted potential range down to ~0.7 V (vs. SHE), where the oxide remains only partially reduced [16,55,60–66]. However, such oxide films at Pt never exhibit reversible redox behaviour like RuO_2 (or IrO_2) upon potential cycling [55]. The thick oxide film on Pt electrode is also completely reduced to the metallic Pt (at the conditions of under potential deposition of hydrogen) in one negative going cycle [6–8,16,55,61–67]. For RuO_2 (or IrO_2) the key difference is that probably once the thick oxide layer is formed, it never reduces back to the bulk metal in a cathodic half cycle, so that a lower oxidation state oxide film remains on the Ru surface down to (and through) the H^+/H_2 reversible potential.

4.3 Carbide-derived carbons

Carbon produced by extraction of metal cations or non-metal cations from binary carbides is called carbide-derived carbon (CDC). Leaching in supercritical water, high-temperature treatment in halogens, vacuum decomposition, and other methods can be used to remove the metal or non-metal cations from different carbides, producing microporous-mesoporous carbon [68]. Selective etching of carbides offers unique control over carbon microstructure, thus synthesis of materials with narrow pore-size distribution, variable pore diameters and shape, and surface termination, and allowing optimization of material properties for improved performance in advanced applications. In the synthesis process, the carbide lattice is used as a template and cations are extracted layer-by-layer, so the control can be achieved at the atomic-level. Thus, the structure of the carbide is template for the carbon structure formed, with an opportunity for further modification by selection of the precursor carbide, synthesis temperature and the conditions of the synthesis environment. Uniform, relatively small pores (so-called micropores) formed during chlorination at lower temperatures have been associated with the amorphous structure of the CDCs, while less uniform and generally larger pores (mesopores) formed at higher synthesis temperatures have been linked to the graphitic ribbon network structure. In addition, CDC synthesis allows formation of highly porous carbon materials with good and tunable mechanical properties.[68–71]

4.4 Methods for physical characterization of materials

4.4.1 Porosity characterization

In this work, the low temperature (77 K) nitrogen sorption method was used for the study of the porosity of the carbon materials. From the evaluation of the adsorption isotherm we can reveal information about pore size, volume and specific surface area of the materials under study.

4.4.1.1 Interpretation and classification of adsorption isotherms

The shape of the isotherm depends on the type of the adsorbent and/or adsorbate and on the strength of the intermolecular interactions between the gas and the surface of the sample. According to IUPAC classification the adsorption isotherms can be divided into six classes (Fig. 3).

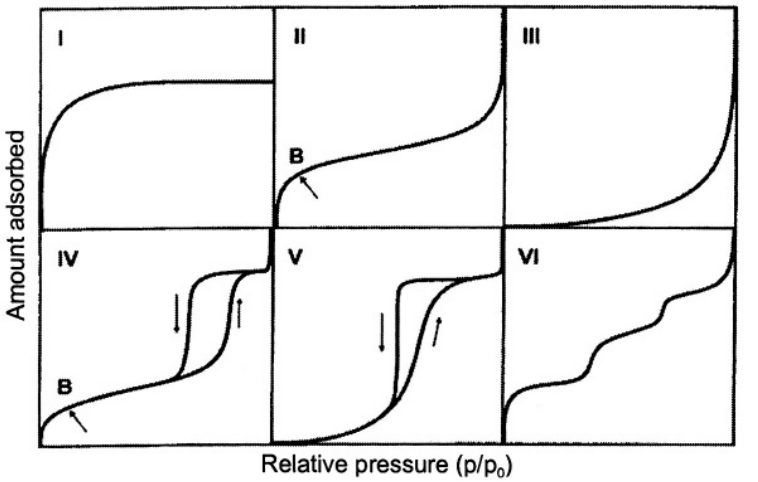

Figure 3. Main types of gas physisorption isotherms (IUPAC, 1985) [72].

Type I isotherm can be described by Langmuir adsorption equation. The main feature of reversible Type I isotherm is the long and horizontal plateau being characteristic for totally microporous adsorbent. Mircopore filling may occur in pores of molecular dimensions or pores with relatively small amount of multilayer adsorption. Type II and III isotherms describe adsorption in macroporous adsorbents with strong and weak adsorbate-absorbent interaction, respectively. Type II isotherm is typical for adsorption in mesoporous material and demonstrates no remarkable hysteresis. Type III isotherm occurs in systems where the adsorbate-sorbent interaction is small compared to the adsorbate-adsorbate interaction, thus, it is characteristic for the strongly associated molecules. Types IV and V characterize mesoporous absorbent with strong and

weak affinities, respectively. Furthermore, Types IV and V represent adsorption isotherms with hysteresis loop (Fig. 4). The hysteresis loop is associated with the filling (and emptying) of the mesopores by the capillary condensation effect [73]. Type IV isotherm describes the adsorption behaviour of special mesoporous materials showing pore condensation effect together with hysteresis behaviour between the adsorption and the desorption branch. The type V isotherm is very similar to Type III with weak adsorbent-adsorbate interaction. The Type VI isotherm, or stepped isotherm, is associated with layer-by-layer adsorption on a highly uniform surface [72,74,75].

Hysteresis loop, which appears in the multilayer range of physisorption isotherm, is generally associated with the capillary condensation effect. According to the laws of classical thermodynamics, the amount of adsorbed gas is controlled by the chemical potential of the adsorbent. It follows that the two branches of a loop cannot both satisfy the requirement of thermodynamic reversible adsorption/desorption process. The appearance of reproducible and stable hysteresis loop in the isotherm therefore implies the existence of certain well-defined metastable states. The four main types of hysteresis loops are illustrated in Fig. 4.

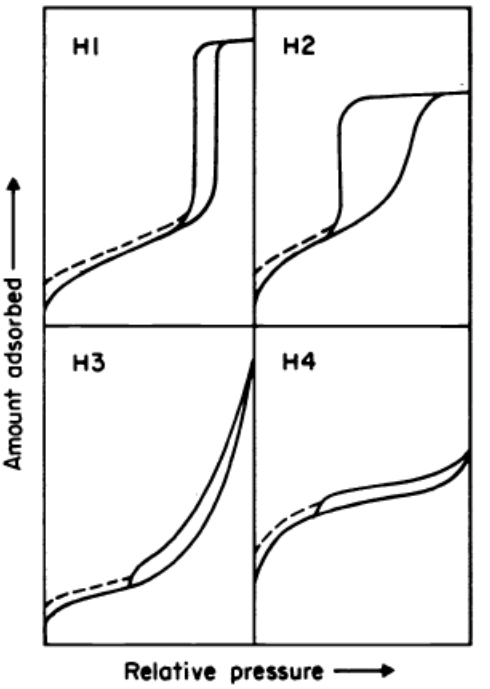

Figure 4. Types of hysteresis loops [76].

Type H1 hysteresis loop is a fairly narrow loop with very steep and nearly parallel adsorption and desorption branches and it is characteristic for materials with a narrow distribution of the uniform pores. Type H2 hysteresis loop is broad with a long and almost a flat plateau at high relative pressure and with a steep desorption branch indicating that the pore structure is complex and tend to be made up of interconnected networks of pores of different sizes and shapes. Types H3 and H4 hysteresis loops do not terminate in a plateau at high relative pressure and the limiting desorption boundary curve is therefore more difficult to establish. Type H3 loop is usually generated by the aggregates of platy particles or adsorbents containing slit-shaped pores. Type H4 is also characteristic of slit-shaped pores, as in many activated carbons, but in this case the pore size distribution is mainly in the micopore range [73].

4.4.1.2 Brunauer-Emmett-Teller theory

The Brunauer-Emmett-Teller (BET) theory [75,77–79] is the most popular method to determine the specific surface area of powders and porous materials. The BET equation is written as:

$$\frac{1}{\mathrm{W}\left(\frac{P}{P_0}-1\right)} = \frac{1}{W_{\mathrm{m}}c} + \frac{c-1}{W_{\mathrm{m}}c}\cdot\frac{P}{P_0}, \tag{5}$$

where W is the mass of gas adsorbed at relative pressure P/P_0, W_{m} is the mass of gas absorbed in monolayer and c is the constant in BET theory describing the adsorbent-adsorbate interactions. Thus, the BET plot in coordinates $1/\{W[(P/P_0)–1]\}$, P/P_0 should be a linear line (P/P_0 range from 0.05 to 0.35) with the slope and intercept values, as followed:

$$\mathrm{slope} = \frac{c-1}{W_{\mathrm{m}}c},$$

$$\mathrm{intercept} = \frac{1}{W_{\mathrm{m}}c}. \tag{7}$$

Thefore, W_{m} can be calculated from the slope and intercept as:

$$W_{\mathrm{m}} = \frac{1}{\mathrm{slope}+\mathrm{intercept}}. \tag{8}$$

The specific surface area, S_{BET}, of the material can be calculated as:

$$S_{BET} = \frac{W_m N_A A_{CS}}{Mm}, \quad (9)$$

where N_A is the Avogadro constant ($6.023 \cdot 10^{23}$ molecules per mole), A_{CS} is the molecular cross-section area of adsorbate (0.162 nm^2 for N_2 at 77 K[75,78]), M is the molar mass of adsorbate and m is the mass of adsorbent.

4.4.1.3 Total pore volume

The total pore volume, V_{tot}, is defined as the liquid volume absorbed at certain relative pressure, when the sorption isotherm exhibits a distinct plateau. In this case, it is assumed that all pores are filled with liquid adsorbate and thus, the density of the adsorbate is equal to the density of the liquid bulk at saturation pressure.[80] Thus, V_{tot} can be calculated from the amount of adsorbed nitrogen, V_{ads}, at a pressure P, and temperature T, using the following equation:

$$V_{tot} = \frac{PV_{ads}V_{molar}}{RT}, \quad (10)$$

where V_{molar} is the molar volume of adsorbate (34.7 $cm^3\ mol^{-1}$ for N_2 at 77 K) and R is the ideal gas constant (8.314 J $mol^{-1}\ K^{-1}$).

4.4.1.4 The *t*-plot method

The *t*-plot method [75,78,81,82] is used for determination of the volume of micropores, V_{micro}, and external surface area, S_{ext}, and for detecting the presence of mesopores in carbon materials. The experimental isotherm is transformed into *t*-plot, where the adsorbed gas volume, V_{ads}, is plotted against the statistical thickness of the adsorbed layer, t_{stat}. There are many methods to determine t_{stat}, but in present work the Harkins-Jura approximation is used:

$$t_{stat} = \sqrt{\frac{13.99}{0.034 - \log\frac{P}{P_0}}}. \quad (11)$$

The S_{ext} can be calculated from the slope of the linear high-pressure area of the *t*-plot and the intercept extrapolated to the volume axis will provide the V_{micro}. The surface area of micropores, S_{micro}, can be found from the difference of total surface area and meso-and macropore area:

$$S_{micro} = S_{BET} - S_{ext}. \quad (12)$$

4.4.1.5 Non-local density functional theory

Non-local density functional theory (NLDFT) [78,83] is used to describe the pore size distribution in both micro- and mesopore range of materials with hierarchical porous structure. NLDFT describes objectively the local structure of liquid condensed compound at the solid curved surfaces. The shape of adsorption isotherm for the model porous surface is determined by the liquid-liquid and liquid-solid interactions. Calculation of the pore size distribution is based on a solution of the generalized adsorption isotherm (GAI) equation, which correlates the kernel of theoretical adsorption/desorption isotherms with the experimental sorption isotherm:

$$N\left(\frac{P}{P_0}\right) = \int_{W_{\min}}^{W_{\max}} N\left(\frac{P}{P_0}, W\right) f(W) dW \tag{13}$$

where $N(P/P_0)$ is the experimental adsorption isotherm, W is the pore width, $N(P/P_0, W)$ is the kernel of theoretical isotherms in pores of different widths and $f(W)$ is the pore size distribution function. The GAI equation assumes that the total isotherm consist of isotherms of single pores which are multiplied by their relative distribution, f(W), over a range of pore sizes [83].

4.4.2 X-ray diffraction method

X-ray diffraction (XRD) method provides a convenient and practical mean for the qualitative identification of the structure of the crystalline compound. Thus, the X-ray powder diffraction method is the simplest analytical method that is capable of providing qualitative and quantitative information about the structure of compounds present in a solid sample. Information about the arrangement and the spacing of atoms in crystalline materials can be determined directly from XRD studies. XRD method is based upon the fact that XRD pattern is unique for each crystalline substance. Thus, if an exact match can be found between the reference pattern and the sample under study, the chemical and crystallographic identity can be assumed. [84,85]

Determination of the crystallite size is one of the most important applications in XRD powder method for materials characterization. To obtain the real crystallite size, the true mean shape of the crystallites must be known in order to derive and apply a correction to the column height of each crystallographic orientation (*hkl*). The Lorentzian band shape and the Gaussian error-distribution function are suitable for approximation of the band shape with a meaningful mathematical function. Based on the Scherrer equation, the half-value breadth B of the diffracted beam is proportional to the reciprocal of crystallite size. The Scherrer equation can be written as:

$$B = \frac{K\lambda}{L\cos\frac{\chi}{2}}, \tag{14}$$

where K is a constant (K = 0.93), λ is the X-rays wave-length, L is the linear dimension of particle and $\chi/2$ is the Bragg angle ($\theta = \chi/2$) [86].

4.4.3 Raman scattering method

Raman spectroscopy is a standard non-destructive analysis tool for characterization of the crystalline, nanocrystalline and amorphous materials. In Raman spectra recorded in the near-infrared and visible light regimes, carbon materials typically exhibit two broad bands, called as D (disordered induced) and G (graphitic) bands. In highly oriented pyrolytic graphite (HOPG) only a G-peak appears in Raman spectra around 1580–1600 cm^{-1}, while in disordered carbons, besides the G-peak, a D-peak appears at lower wavenumbers ~1350 cm^{-1} [87,88]. The presence and position of D- and G-peaks, ratio of their intensities (I_D/I_G) and full width at half maximum (FWHM) can be used to extract structural information of the materials. The intensity ratio of D- and G-peaks (I_D/I_G) is proportional to the in-plane correlation length. I_D/I_G is increasing with decay of the size of the perfect graphene layers, as the disorder is growing and the D-mode is becoming more active, as predicted by the Tuinstra-Koenig (T–K) relationship

$$\frac{I_D}{I_G} = \frac{C(\lambda)}{L_a}, \tag{15}$$

where I_D and I_G are the heights or integrated intensities of the D-peak and G-peak, respectively, L_a is the in-plane correlation length. The parameter $C(\lambda)$ is wavelength dependent parameter and can be described by the following equation: $C \approx C_0 + \lambda C_1$, where the parameters $C_0 = -12.6$ nm and $C_1 = 0.033$ are valid within the wavelength region 400 nm < λ < 700 nm.[84,87,88]

However, fitting of the Raman spectra of amorphous carbon is not always straightforward as the D- and G-peaks normally are distorted and there is no particular function for Raman spectra fitting. The simplest fits are done by applying two Gaussian or two Lorentzian profiles. A Lorantzian fit is often used for crystallised carbon and disordered graphite.

4.4.4 Transmission electron microscopy method

Transmission electron microscopy (TEM) and high resolution transmission electron microscopy (HRTEM) are powerful imaging tools to study materials at the nanometric and atomic resolution scale, respectively. These methods usually provide detailed geometric features and images, and are useful for examining what has happened on the subsurface, for instance, the indentation induced dislocations in a metal. TEM studies also yield information regarding the crystal structure, crystal quality and grain size. When operating in the diffraction mode, selected area electron diffraction (SAED) patterns can be used to determine the crystal structure of materials [85,89]. TEM method enables the fine-scale microstructure to the nanoscale applicable for the specimens sufficiently thin to facilitate transmission of a beam of electrons without a great loss of intensity. The maximum transmittable thickness depends upon the atomic number of the material, but typically this thickness lies in the range from 250 to 500 nm. However, the higher the applicable electron energy, the better the transmission through the specimen is and this has led to the construction of instruments with accelerating voltages in the range from 100 kV to 3 MV. In current generation instruments have accelerating voltages that lie in the range from 120 to 400 kV. For high-resolution images taken under controlled conditions, the periodicity of the fringes in the image corresponds with the spacing of crystal lattice planes in the specimen [85].

Electron lenses that can focus the electrons and guide them into an electron spectrometer are already present in a transmission electron microscope, so electron energy loss spectroscopy (EELS) measurements are performed in it, taking advantage of its imaging and diffraction capabilities to identify the structure of the material being analysed. EELS is capable of measuring atomic composition, chemical bonding, valence and conduction band electronic properties, surface properties, and element-specific pair distance distribution functions [90]. EELS is perhaps the best method developed for the carbon materials and it is easy to determine the differences among graphite, diamond or amorphous carbon (i.e. analysed the electron configurations of carbons in materials).

4.5 Methods for electrochemical characterization

4.5.1 Cyclic voltammetry method

Cyclic voltammetry (CV) is frequently used electrochemical technique because it offers a wealth of experimental information and insights into both the kinetic and thermodynamic details of many chemical systems. Based on the analysis of the shape of the voltammogram, the rate of the heterogeneous electron transfer or homogeneous chemical process accompanying electrochemical charge transfer step could be determined based simply on the measurement of peak

potential, E_P, and peak current, I_P, data as a function of electrode potential scan rate, v.[91–93] In CV method the electrode potential is changed from the initial potential to the final potential and then inverted back to the initial potential. The faradic current, I_f, due to the electrode reaction, is registered in the relevant zone of applied potential, where the electrode reaction occurs. However, there is also a capacitive contribution as on sweeping the electrode potential, the double layer charge density changes and therefore capacitive contribution increases with increasing of the electrode potential scan rate. The total current, I, is:

$$I = I_C + I_f = C_d \frac{dE}{dt} + I_f = vC_d + I_f, \tag{16}$$

where I_C is the capacitive current and C_d is the differential capacity of the double layer. Thus, I_c is proportional to v ($I_C \propto v$) and I_f is proportional to square root of v ($I_f \propto v^{1/2}$). Therefore, at very high potential scan rates the capacitive current must be subtracted from total current density in order to obtain the accurate values of rate constant for the electrochemical reaction.
In case of an irreversible oxidation reaction of the type O + $n\bar{e}$ → R, no inverse peak appears in current density,-potential (j, E) curve on inversing the scan direction. With respect to reversible systems the current waves are shifted to more negative potentials and E_p depends on v. The peak current is given as:

$$I_p = -2.99 \cdot 10^5 n^* (\alpha_c n')^{1/2} A c_O^b D_O^{1/2} v^{1/2}, \tag{17}$$

where n^* is the total number of electrons transferred, n' is the number of electrons transferred in rate determining step, α_c is the transfer coefficient, D_O is the diffusion coefficient, c_O^b is the concentration of substance O in the bulk solution and A is the flat cross-section (geometric) surface area of the electrode. The peak potential is given as:

$$E_p = E^{\Theta'} - \frac{RT}{\alpha_C n' F}\left[0.780 + \ln\frac{D_O^{1/2}}{k_0} + \frac{1}{2}\ln\frac{\alpha_C n' F v}{RT}\right], \tag{18}$$

where $E^{\Theta'}$ is the formal potential and k_0 is the rate constant. For the irreversible electrochemical reaction the current peaks are broader and lower [92].

4.5.2 Rotating disk electrode method

The rotating disk electrode (RDE) method is one of the best methods to control the efficient mass transport condition and thus, the kinetic measurements can be made with higher precision. Moreover, at steady state, the double-layer charging current does not influence the current measured. The most important feature of the RDE method is that the rate of mass transport to the surface is uniform. The linear velocity of the selected point on the surface increases with the distance from the center of rotation. The other important property of RDE technique is that the flow rate of the solution around it is laminar up to rather higher rotation rates. Since the flow is laminar, it is possible to calculate the rate of mass transport applying by the theory developed by Levich:

$$j_{\mathrm{D}} = -0.62 n \mathrm{F} D_{\mathrm{O}_2}^{2/3} \mathrm{v}^{-1/6} \omega^{1/2} c_{\mathrm{O}_2}^{\mathrm{b}}, \tag{19}$$

where j_{D} is the diffusion step limited charge transfer current density, n is the number of electrons transferred per electroreduction of one O_2 molecule, F is the Faraday constant, D_{O_2} is the diffusion coefficient for O_2 (1.8×10^{-5} cm^2 s^{-1}[39]), $c_{\mathrm{O}_2}^{\mathrm{b}}$ is the concentration of O_2 in the bulk solution (1.3×10^{-6} mol cm^{-3} at 25 °C[39]), v is the kinematic viscosity of the solution (0.01 cm^2 s^{-1}), ω is the angular velocity of rotation, ω=2πf, where f is the number of revolutions of disk per second. Based on the Levich equation, the limiting current is a linear function of the reagent concentration, and thus, Eq. 19 can be used to determine the diffusion coefficient of reacting species in solution.

In mixed kinetics control area, the Koutecky-Levich (K-L) equation can be applied and the total current density, j, can be defined as:

$$\frac{1}{j} = \frac{1}{j_{\mathrm{K}}} + \frac{1}{j_{\mathrm{D}}} = -\frac{1}{n\mathrm{F}k_{\mathrm{het}}c_{\mathrm{O}_2}^{\mathrm{b}}} - \frac{1}{B\omega^{1/2}}, \tag{20}$$

where j_{K} is the kinetic current density, k_{het} is the electrochemical rate constant for ORR and coefficient $\mathrm{B} = 0.62 n \mathrm{F} D_{\mathrm{O}_2}^{2/3} \mathrm{v}^{-1/6} c_{\mathrm{O}_2}^{\mathrm{b}}$. From the slope values of the linear K-L plot, the diffusion coefficient or the number of electrons transferred, and from the intercept the kinetic current densities can be determined [92,94,95].

The RDE data for supported catalyst with relatively thick catalyst layer can be analyzed using the modified Koutecky-Levich (K-L) equation:

$$\frac{1}{j} = \frac{1}{j_{\mathrm{K}}} + \frac{1}{j_{\mathrm{D}}} + \frac{1}{j_{\mathrm{f}}} = -\frac{1}{n\mathrm{F}k_{\mathrm{het}}c_{\mathrm{O}_2}^{\mathrm{b}}} - \frac{1}{0.62 n \mathrm{F} D_{\mathrm{O}_2}^{2/3} \nu^{-1/6} \omega^{1/2} c_{\mathrm{O}_2}^{\mathrm{b}}} - \frac{L_{\mathrm{f}}}{n\mathrm{F}c_{\mathrm{f}}D_{\mathrm{f}}}, \tag{21}$$

where j_f is the current density in the Nafion® film with thickness L_f, c_f and D_f are the O_2 concentration and diffusion constant in the Nafion® film, respectively. However, analysis made by Behm et al. [26,96] demonstrates that for thin Pt-carbon film electrodes the role of Nafion® layer is unimportant (because if j_f is very high, then $j_f >> j_k$) and the classical K-L equation (Eq. 20) can be applied.

Between the limiting current plateau of a voltammogram and the nearly linear region close to the equilibrium potential, E_{eq}, ($j \rightarrow 0$) there is a region of potential for irreversible reactions, where j depends exponentially on potential, known as the so-called Tafel region. For the reduction process, the Tafel law expresses as:

$$-\ln\left|j_{cat}\right| = const - \frac{\alpha_C nFE}{RT}, \tag{22}$$

where j_{cat} is the cathodic current density and α_C is the cathodic transfer coefficient [92].

4.5.3 Electrochemical impedance spectroscopy method

Electrochemical impedance spectroscopy (EIS) represents a powerful method for investigation of the electrical properties of materials and interfaces of conducting electrodes as well as the kinetics of complex electrochemical systems. [91,92,94] This non-steady-state measuring technique involves the application of a small sinusoidal currents or potential perturbation. Perturbation of the electrochemical system leads to a small shift of the steady state. The responses to the applied perturbation, which is generally sinusoidal, can differ in phase and amplitude from the applied signal. If a monochromatic alternating voltage $E(t) = E_0\sin(\omega t)$ is applied to an electrode, then the resulting current is $I(t) = I_0\sin(\omega t+\theta)$, where θ is the phase difference between the voltage and the current and E_0 and I_0 are the amplitudes of the sinusoidal voltage and current, respectively. Then, by the Ohm's law ($I = E/R$), the impedance (complex resistance), Z, is defined as, [93–95]:

$$Z = \frac{U(t)}{I(t)} = \left|Z\right|e^{j\theta} = Z' + jZ'', \tag{23}$$

with $j = \sqrt{-1}$, where Z' and Z'' are the real and imaginary part of the impedance, respectively. Thus, the impedance of the real electrochemical system is a function of frequency. For the pure resistor, the phase shift is zero and for a pure capacitor it is $-\pi/2$ rad (–90°). For the real electrochemical interphase the phase value depends on the electrochemical processes taking place at the interface as well on the frequency applied.

For an equivalent circuit, where the resistance is connected in series with the capacitive element with capacitance, C, so called RC circuit, the following relations are valid:

$$Z'' = R_S \Rightarrow C_S = -\frac{1}{Z'' \cdot 2\pi f}, \tag{24}$$

$$\frac{|Z|^2}{Z'} = R_P \Rightarrow C_P = -\frac{Z''}{|Z|^2 \cdot 2\pi f}, \tag{25}$$

where R_S and C_S are the series resistance and series capacitance, respectively, and R_P and C_P are the parallel resistance and parallel capacitance, respectively, $|Z|$ is the magnitude of impedance and f is the AC frequency. For the ideally polarizable interface the series and the parallel capacitances must be equivalent [93,94].

For the liquid electrochemical systems, the EIS experiments have been usually conducted in the range of frequencies from 10^{-3} to 10^5 Hz.

5. EXPERIMENTAL

5.1 Synthesis of carbide-derived carbon powders from Mo_2C

The CDC powders were synthesized from Mo_2C [70] according to the following simplified reaction scheme: $Mo_2C + 5Cl_2 \rightarrow C + 2\ MoCl_5$. Mo_2C powder (−325 mesh, 99.5%, Sigma-Aldrich), loaded into a quartz vessel in a tube furnace, was reacted with Cl_2 (99.999%, AGA) for 6 h at a flow rate of 50 ml min^{-1} at different fixed synthesis temperatures, t_{synt}: 600, 750, 800, 850, 900 and 1000 °C [70]. The by-product $MoCl_5$ was removed by the flow of excess Cl_2. After chlorination the product (microporous-mesoporous C(Mo_2C) carbon) noted as C(Mo_2C)600 °C, C(Mo_2C)750 °C, C(Mo_2C)800 °C, C(Mo_2C)850 °C, C(Mo_2C)900 °C and C(Mo_2C)1000 °C, was additionally treated with H_2 for 2 h at 800 °C in order to remove residual chlorine, chlorides, and oxygen-containing functional groups. During the heating and cooling steps the reactor was flushed with a stream of Ar (99.9999%, AGA). The t_{synt} were selected to prepare carbon materials with a wide variation of microporosity-mesoporosity characteristics, including S_{BET} [70,97].

5.2 Preparation of Pt-nanoclusters or Pt-Ru alloy nanoclusters activated catalysts

The Pt-nanoparticles or the Pt-Ru alloy nanoparticles were deposited onto carbon support by sodium borohydride reduction method [38]. The required quantity of $H_2PtCl_6{\times}6H_2O$ (99.9%, Alfa Aesar) was dissolved in Milli-Q^+ water (18.2 MΩ cm at 25 °C) to prepare a solution with Pt-salt concentration of ~1 mM [98,99]. For the Pt(50 at%)-Ru(50 at%) (at% – atomic %) binary alloy catalyst synthesis required quantities of $H_2PtCl_6{\times}6H_2O$ and $RuCl_3{\times}xH_2O$ (both 99.9%, Alfa Aesar) were dissolved in Milli-Q^+ water and the solution was diluted to prepare a metal salts solution with a total metal cation concentration of ~2 mM [5]. The prepared solution was stirred at room temperature (22±1 °C) for 1 h. The pH of the solution was adjusted to ~8 through drop-wise addition of 20 wt% solution of NaOH (99.99%, Sigma Aldrich). The required amount of carbon powder was added into the aqueous solution. Thereafter, the $NaBH_4$ (≥98.0%, Aldrich) solution was prepared by dissolving $NaBH_4$ in Milli-Q^+ water, which was carefully added to the previously prepared suspension. The reaction mixture was stirred for 2 h and left to settle overnight. The catalyst (noted as Pt-C(Mo_2C)600 °C, Pt-C(Mo_2C)750 °C, Pt-C(Mo_2C)800 °C, Pt-C(Mo_2C)850 °C or Pt-C(Mo_2C)1000 °C and Pt-Ru-C(Mo_2C)600 °C or Pt Ru-C(Vulcan)) was filtered, rinsed thoroughly with Milli-Q^+ water and dried at 80 °C. The mass percent of Pt in the catalyst material synthesized was ~70 wt% (14 at%) and the total Pt-Ru alloy loading was ~20 wt% of the mass of C(Mo_2C).

5.3 Methods for structural characterization of powders and electrodes

XRD patterns for the studied materials were collected with a Bruker D8 Advance diffractometer with Ni filtered CuK_α radiation (0.6 mm wide parallel beam, two 2.5° Soller slits and LynxEye line detector). The scanning step for 2θ was 0.01° from 16° to 90° and the total counting time per step was 166 s. The X-ray tube was operated at 40 kV and 40 mA and the data were treated using Scherrer equation.

The porosity of the CDC powders was studied using the low temperature (−195.8 °C) nitrogen sorption method [100] (Micromeritics ASAP 2020). The NLDFT and the slit shape pore model were used for the pore size calculation. S_{BET} was calculated using the BET multipoint theory [77] within the p/p_0 range from 0.05 to 0.2. The values of V_{tot} (near saturation pressure) and V_{micro} were calculated using *t*-plot method with Harkins and Jura thicknesses between 0.5 and 0.9 nm [101].

For morphological studies, the materials were examined using HRTEM on a Tecnai 12 instrument, operated at a 120 kV accelerating voltage appling associated techniques, such as EELS, and SAED methods. EELS data for the carbon C-K edge were collected under magic-angle conditions and with collection angle of $\beta \sim 2.4$ mrad (diffraction mode) in the energy range from 280 to 340 eV. HRTEM specimens were prepared from ultrasonic dispersions of the corresponding samples in 1 ml ethanol, and one drop of each suspension was deposited onto a copper grid covered with a holey carbon film.

The X-ray photoelectron spectroscopy (XPS) [102–104] experiments were carried out with a SCIENTA SES-100 spectrometer using an unmonochromated MgK_α X-ray source with power of 300 W. SES-100 system was calibrated using Au 4f photolines. The pressure in the analysis chamber varied from 2×10^{-10} to 5×10^{-10} mbar.

The scanning electron microscopy with energy-dispersive X-ray spectroscopy (SEM-EDX) data were obtained using Helios™ Nanolab 600.

5.4 Electrode preparation

A glassy carbon disk electrode (GCDE), pressed into a Teflon® holder, was used as the catalyst active layer support [5,98,99,105–108]. The GCDE was polished with a 0.05 μm alumina slurry (Buehler) to a mirror finish. After polishing, the GCDE was washed with Milli-Q^+ water and sonicated in Milli-Q^+ water for a few minutes. Catalyst ink was prepared by suspending the C(Mo_2C), Pt-C(Mo_2C) or Pt-Ru-C(Mo_2C) powder in 20 wt% solution of isopropanol (Sigma-Aldrich, >99%) in Milli-Q^+ water and agitated for 30 min in an ultrasonic bath to disperse the suspension homogeneously. Thereafter the Nafion® dispersion (Aldrich) was added (to achieve 5 wt% content of Nafion® ionomer in the final catalyst layer) and the mixture was sonicated and

mechanically mixed for 30 min to prepare a uniformly dispersed ink. All inks were deposited onto the GCDE and dried at 22 ± 1°C.

The flat cross-section (geometric) surface area of the electrode was 0.196 cm^2. The calculated thickness of Nafion® film was <0.1 μm. The catalyst loading on the GCDE for C(Mo_2C) and Pt-C(Mo_2C) electrodes was approximately ~1.0 mg cm^{-2}, including 0.7 mg cm^{-2} Pt in the form of deposited Pt-nanoclusters. For Pt-Ru-C(Mo_2C) electrodes, the loading was ~2 mg cm^{-2} (~0.4 mg cm^{-2} Pt-Ru alloy per flat cross-section surface area).

5.5 Electrochemical measurements

All electrochemical measurements were performed in 0.5 M H_2SO_4 aqueous solution (Fluka, TraceSelect®Ultra) in a three electrode cell [5,98,99,105–108] using CV, RDE (Pine Instrumental Company) and EIE methods applying Autolab PGSTAT 302, Eco Chemie B.V. or Gamry Reference 600 systems. The counter electrode was a large area Pt wire mesh (S_{Pt} > 50 cm^2) separated from the working electrode compartment by a fritted glass membrane. The reference electrode was Hg|Hg_2SO_4|K_2SO_4 (sat.) electrode (MSE) connected to the cell through a Luggin capillary. All potentials were recalculated into the SHE potential scale ($E = E_{MSE} + 0.674$). CV data were measured at different potential scan rates from 2 to 200 mV s^{-1}. RDE data were obtained at rotation rates from 0 to 3000 rev min^{-1} at v = 10 mV s^{-1}. The current densities were calculated using the flat cross-section surface area. The electrolyte solution was saturated with Ar (99.9999%, AGA) or molecular O_2 (99.999%, AGA). All CV and RDE data were statistically treated. EIS data were obtained at fixed electrode potentials within ac frequencies from 0.01 to 10,000 Hz with 5 mV AC voltage excitation.

6. RESULTS AND DISCUSSION

6.1. Analysis of the physical characteristics of the materials

The first-order Raman spectra was obtained using Nd:YAG laser (λ_L = 532 nm) excitation. Data in Fig. 5 exhibit the two typical distinct bands for disordered carbons, the G-band at ~1580 cm^{-1} and the D-band at ~1350 cm^{-1} [70,87,88]. The G-peak corresponds to graphite in-plane vibrations with E_{2g} symmetry and D-peak is a breathing mode with A_{1g} symmetry activated only in the presence of disorder in graphitic structure. The spectrum also shows the second-order peak of D-band (2D) at 2700 cm^{-1}. The increase of 2D peak is related to the crystallographic ordering of the graphitic structure. Thus, as the chlorination temperature increases from 600 to 1000 °C, the C(Mo_2C) powder becomes more ordered [70].

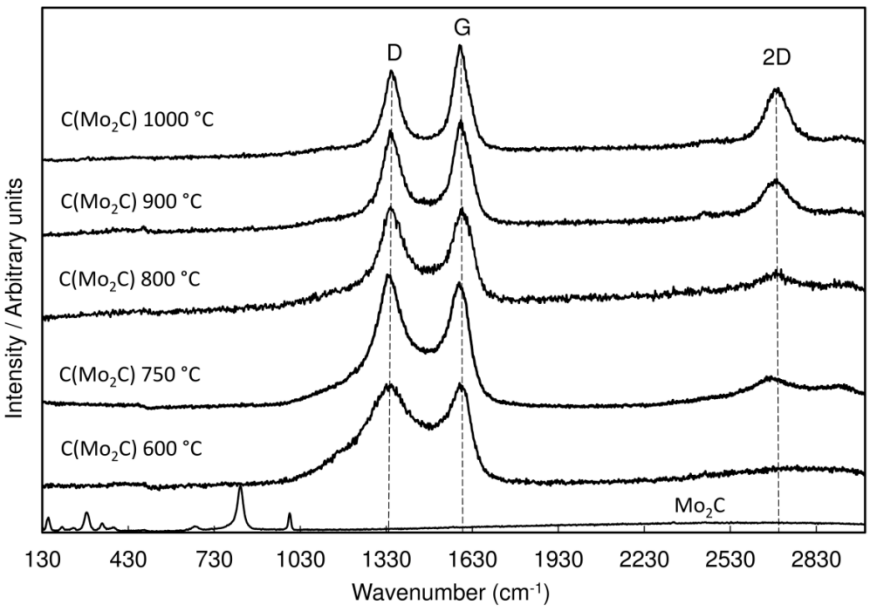

Figure 5. Raman spectra for Mo_2C and C(Mo_2C) powders (normalized by the G-peak intensities).

Comparison of XRD data for pristine C(Mo_2C) (Fig. 6a) with precursor material Mo_2C data shows that the reaction has fully terminated and there is no Mo_2C, $MoCl_5$ and residual chlorine in the studied materials, which is in agreement with X-ray fluorescence (XRF), SEM-EDX and XPS data obtained [5,70,98,99,105–107]. XRD data (Fig. 6a) show that the crystallinity increases with the increase of t_{synt}, however, the medium size of C(Mo_2C) crystallites only slightly increases with t_{synt} [70]. XRD data for Pt-C(Mo_2C) electrodes are represented in

Fig. 6b. Based on the clear XRD reflections for Pt(111), Pt(200), Pt(220), etc. [109], it can be concluded that the deposited Pt-nanoparticles have mainly crystalline structure. The medium size of Pt-crystallites is smallest for Pt-C(Mo_2C)800 °C and Pt-C(Mo_2C)850 °C (Table 1).

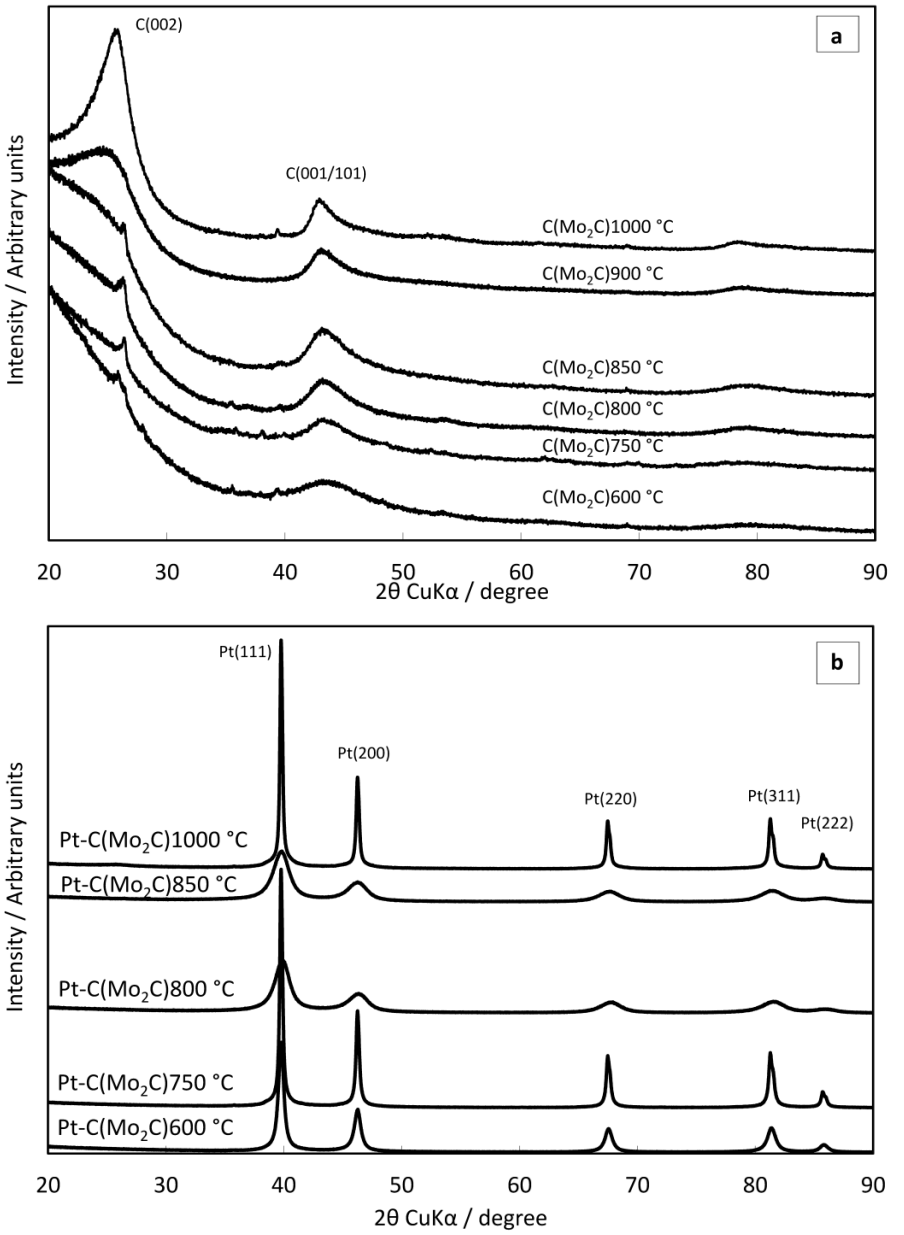

Figure 6. XRD patterns for (a) C(Mo_2C) carbon supports and (b) C(Mo_2C) modified with Pt-nanoparticles catalyst (Pt-C(Mo_2C)) (without Nafion® binder), noted in figure.

Table 1. Lattice parameter, *a*, and Pt crystallite size, *d*, calculated by Scherrer method (Pt(220) reflection) from XRD data.

Parameter/ material	*a*, nm	*d*, nm
Pt-C(Mo_2C)600 °C	0.392	17.3
Pt-C(Mo_2C)750 °C	0.392	27.22
Pt-C(Mo_2C)800 °C	0.390	5.38
Pt-C(Mo_2C)850 °C	0.391	5.65
Pt-C(Mo_2C)1000 °C	0.392	31.15

The I type of isotherm with H4 type hysteresis (according to IUPAC classification [72]) for C(Mo_2C)600 °C and the IV type of isotherm with H2 type hysteresis for other studied C(Mo_2C) powders (Fig. 7a, b) were obtained from N_2 sorption measurements. The data in Table 2 show that the C(Mo_2C) materials can be divided into 2 groups: amorphous materials with high S_{BET} ($S_{BET} > 1700$ m^2g^{-1}) synthesized at $t_{synt} \leq 850$ °C and more graphitized materials with smaller S_{BET} ($S_{BET} < 1500$ m^2g^{-1}) synthesized at $t_{synt} \geq 900$ °C [70]. Increasing t_{synt} from 800 °C to 1000 °C decreases S_{BET} and S_{micro}, but noticeably increases the mesopore surface area (S_{meso}). Maximal S_{meso}, V_{tot} and mesopore volume (V_{meso}) for t_{synt} 600 to 900 °C were established for C(Mo_2C)800 °C powder. Thus, the pore size distribution data in Fig. 7c indicate that the porosity of the C(Mo_2C) carbon powders is widely tuneable.

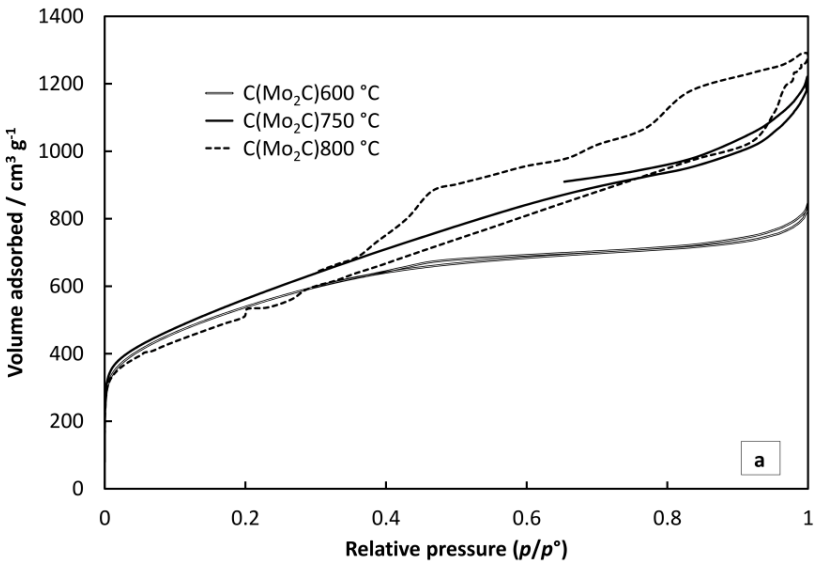

Figure 7 (a)

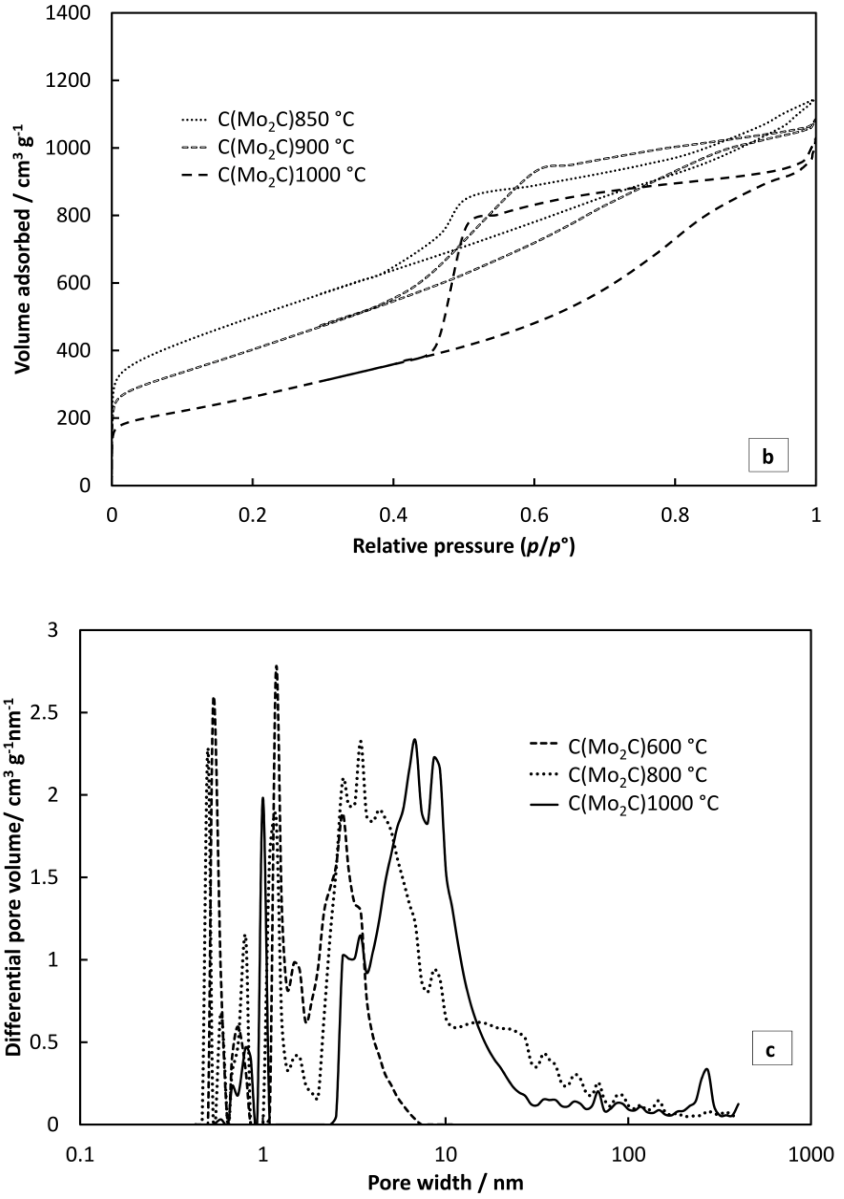

Figure 7. N_2 adsorption isotherms (a and b) and (c) differential pore volume distribution vs. pore width plots for C(Mo_2C) carbon powders, (without Nafion® binder), noted in figure.

Table 2. Results of N_2 sorption measurements for C(Mo_2C) and C(Vulcan) powders.

Parameter/ material	S_{BET} m^2g^{-1}	S_{micro} m^2g^{-1}	S_{meso} m^2g^{-1}	S_{micro}/S_{BET}	V_{tot} cm^3g^{-1}	V_{micro} cm^3g^{-1}	V_{meso} cm^3g^{-1}
C(Mo_2C)600 °C	1940	1810	130	0.93	1.25	0.96	0.29
C(Mo_2C)750 °C	2020	1660	360	0.82	1.83	1.07	0.76
C(Mo_2C)800 °C	1920	1460	460	0.76	1.97	1.09	0.88
C(Mo_2C)850 °C	1790	1440	350	0.80	1.77	1.08	0.69
C(Mo_2C)900 °C	1450	1325	125	0.91	1.64	1.4	0.24
C(Mo_2C)1000 °C	940	260	680	0.28	1.53	0.09	1.44
C(Vulcan)	240	150	90	0.63	0.83	0.07	0.76

S_{BET} – specific surface area, S_{micro} – micropore area, S_{meso} – mesopore area, V_{tot} – total pore volume, V_{micro} – micropore volume, V_{meso} – mesopore volume.

HRTEM data (Figs. 8a–b) for morphological studies of the carbons show that with the increase of t_{synt} the carbon structure becomes more graphitised. The C(Mo_2C) 600°C particles (Fig. 8a) are mainly amorphous and for C(Mo_2C) 800°C (Fig. 8b) clearly ordered graphitic areas can be seen at some surface regions. The Pt- and Pt-Ru-nanoparticles are dispersed quite homogenously over the C(Mo_2C) surface (Fig. 8c–d), however in some areas porous Pt- and Pt-Ru-nanoclusters agglomerates are found.[5,98]

N_2 sorption porosity data (Table 2) and SEM-EDX data (Fig. 9) show that electrode materials have hierarchical structure and well-developed open (micro)-mesoporosity. EDX data (Tables in Figs. 9a–d) show that there is no chemical contamination of C(Mo_2C) electrode with residual Cl_2 or Mo_2Cl_5, or raw Mo_2C. In some areas the binding material Nafion® filaments (as element F) have been observed. EDX data show the small oxygen concentration in C(Mo_2C) powders, probably existing as functional groups at the surface and partly the signal is caused by Nafion® Tables in Fig. 9.

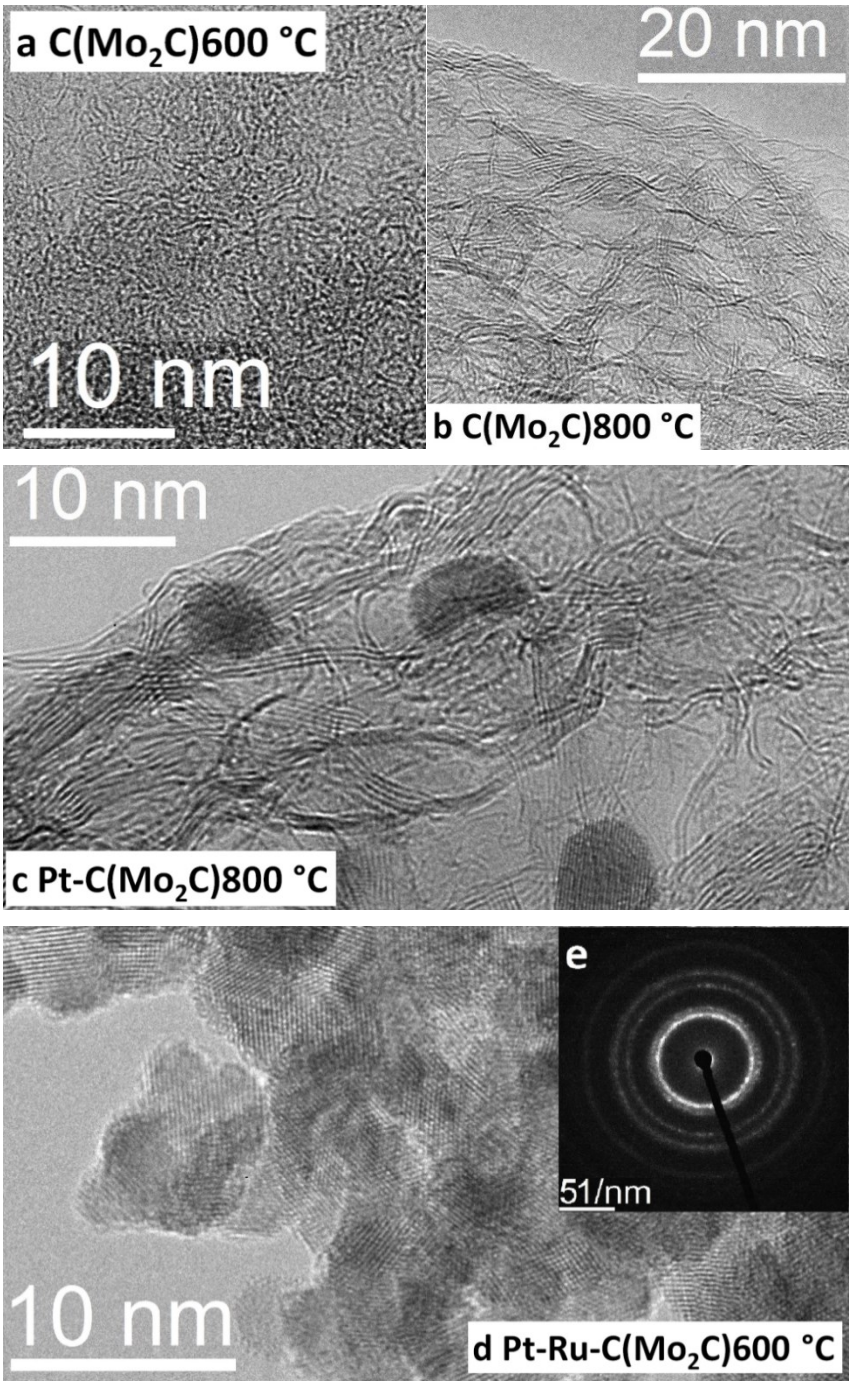

Figure 8. HRTEM images (a–d) and (e) SAED analysis data for material under study, noted in figure.

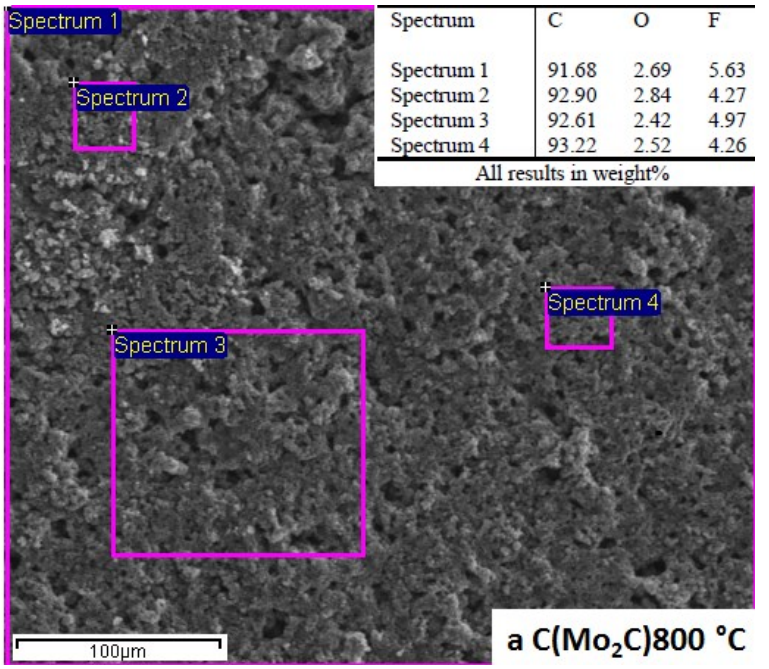

Spectrum	C	O	F
Spectrum 1	91.68	2.69	5.63
Spectrum 2	92.90	2.84	4.27
Spectrum 3	92.61	2.42	4.97
Spectrum 4	93.22	2.52	4.26

All results in weight%

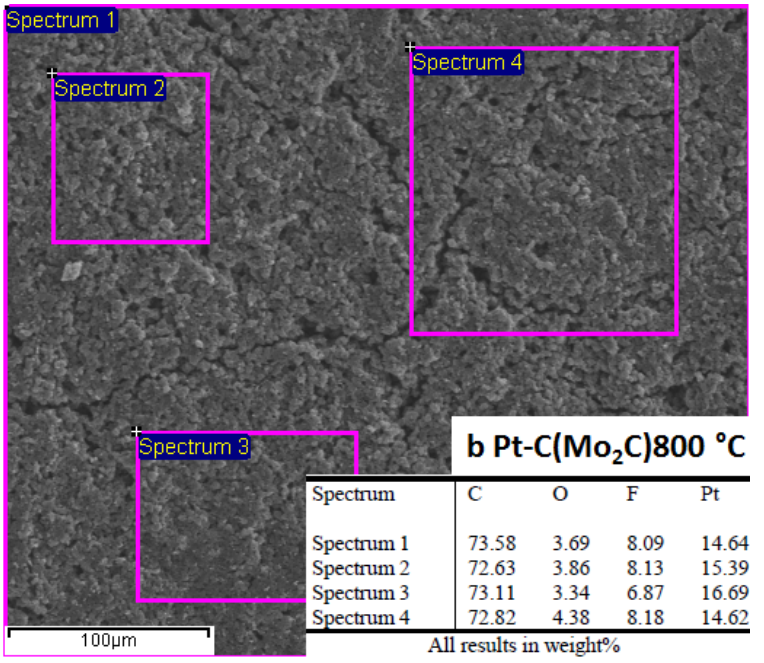

Spectrum	C	O	F	Pt
Spectrum 1	73.58	3.69	8.09	14.64
Spectrum 2	72.63	3.86	8.13	15.39
Spectrum 3	73.11	3.34	6.87	16.69
Spectrum 4	72.82	4.38	8.18	14.62

All results in weight%

Figure 9 (a, b)

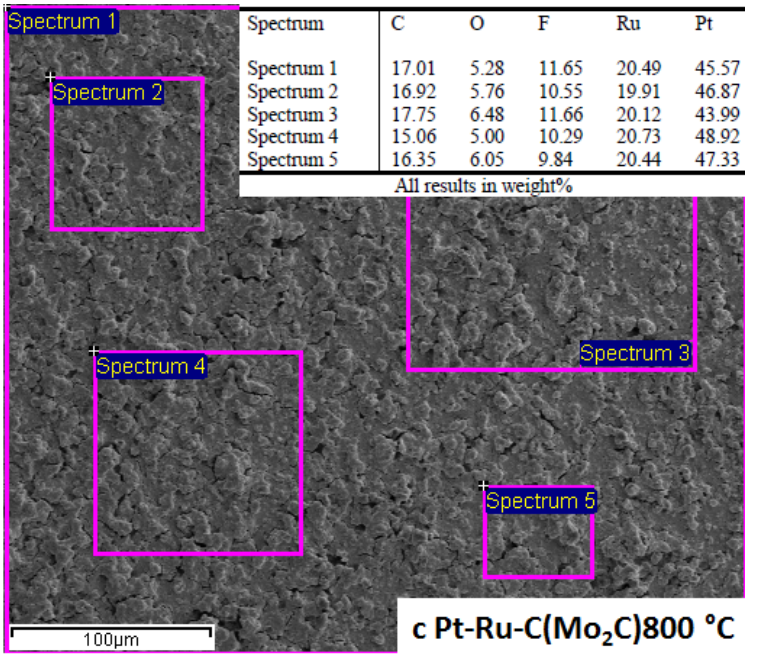

Spectrum	C	O	F	Ru	Pt
Spectrum 1	17.01	5.28	11.65	20.49	45.57
Spectrum 2	16.92	5.76	10.55	19.91	46.87
Spectrum 3	17.75	6.48	11.66	20.12	43.99
Spectrum 4	15.06	5.00	10.29	20.73	48.92
Spectrum 5	16.35	6.05	9.84	20.44	47.33

All results in weight%

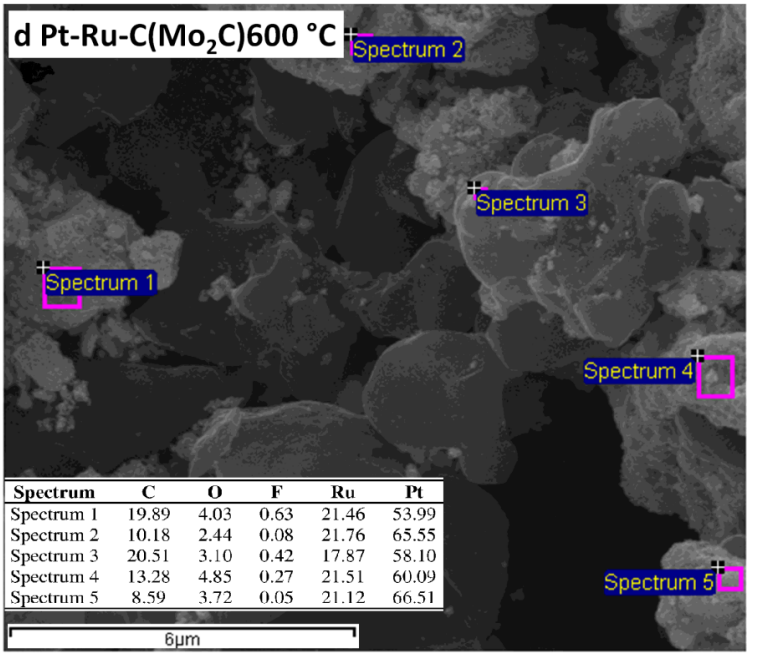

Spectrum	C	O	F	Ru	Pt
Spectrum 1	19.89	4.03	0.63	21.46	53.99
Spectrum 2	10.18	2.44	0.08	21.76	65.55
Spectrum 3	20.51	3.10	0.42	17.87	58.10
Spectrum 4	13.28	4.85	0.27	21.51	60.09
Spectrum 5	8.59	3.72	0.05	21.12	66.51

Figure 9. SEM-EDX data for material under study, noted in figure, (with 1% Nafion® binder) deposited onto GC (glassy carbon) plate.

XPS [104] data (Fig. 10) obtained are in good correlation with SEM-EDX data (Fig. 9d), and clear reflections for Pt and Ru, O, CF and F (CF and F from Nafion® binder) were observed. High resolution spectra for Pt4f configuration region (inset in Fig. 10) showed doublet with peaks at about 71.2 eV ($Pt4f_{7/2}$) and 74.6 eV ($Pt4f_{5/2}$), characteristic of bulk Pt [110].

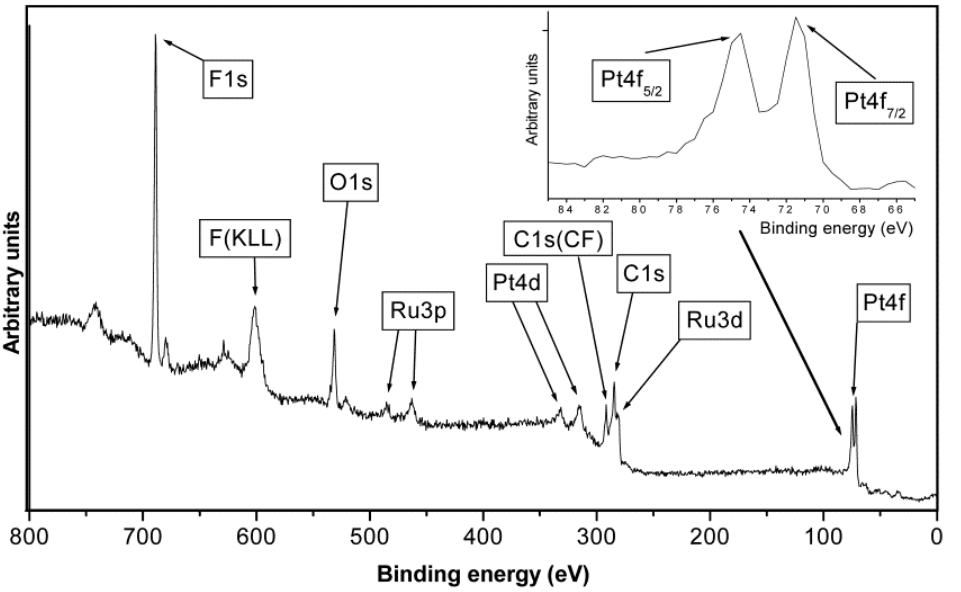

Figure 10. XPS data for Pt-Ru-C(Mo_2C)600 °C catalyst deposited onto GC plate with addition of 1% Nafion® binder.

6.2 Electrochemical characterization of C(Mo_2C) electrodes

CV data show that very high cathodic (electroreduction) current densities j (presented as capacitance, C_{CV}, in Fig. 11) are established for Ar as well for O_2-saturated 0.5 M H_2SO_4 solution within the potential region from 0.6 to 0.2 V (vs. SHE). The values of capacitance, C_{CV}, are calculated from j, E-curves, using the relation $C_{CV} = j/v$. The values of C_{CV} are higher for unmodified C(Mo_2C) electrodes (Fig. 11b) in 0.5 M H_2SO_4 solution with O_2-saturated systems than with Ar-saturated (Fig. 11a), especially within the potential region from 0.6 to 0.1 V (vs. SHE). The values of j and C_{CV} for C(Mo_2C)600 °C are seven to ten times higher than for C(Mo_2C)1000 °C (at $E < 0.7$ V (vs. SHE)). Thus, the electrocatalytic activity of C(Mo_2C) electrode noticeably depends on the S_{BET}, S_{meso}, S_{micro} and V_{micro} values of the carbon powder, determined by the t_{synt} of C(Mo_2C) (Table 2). Electrocatalytically the most active materials with highest capacitance are the amorphous microporous carbon electrode synthesized at the lowest t_{synt} that has the highest number of defects.

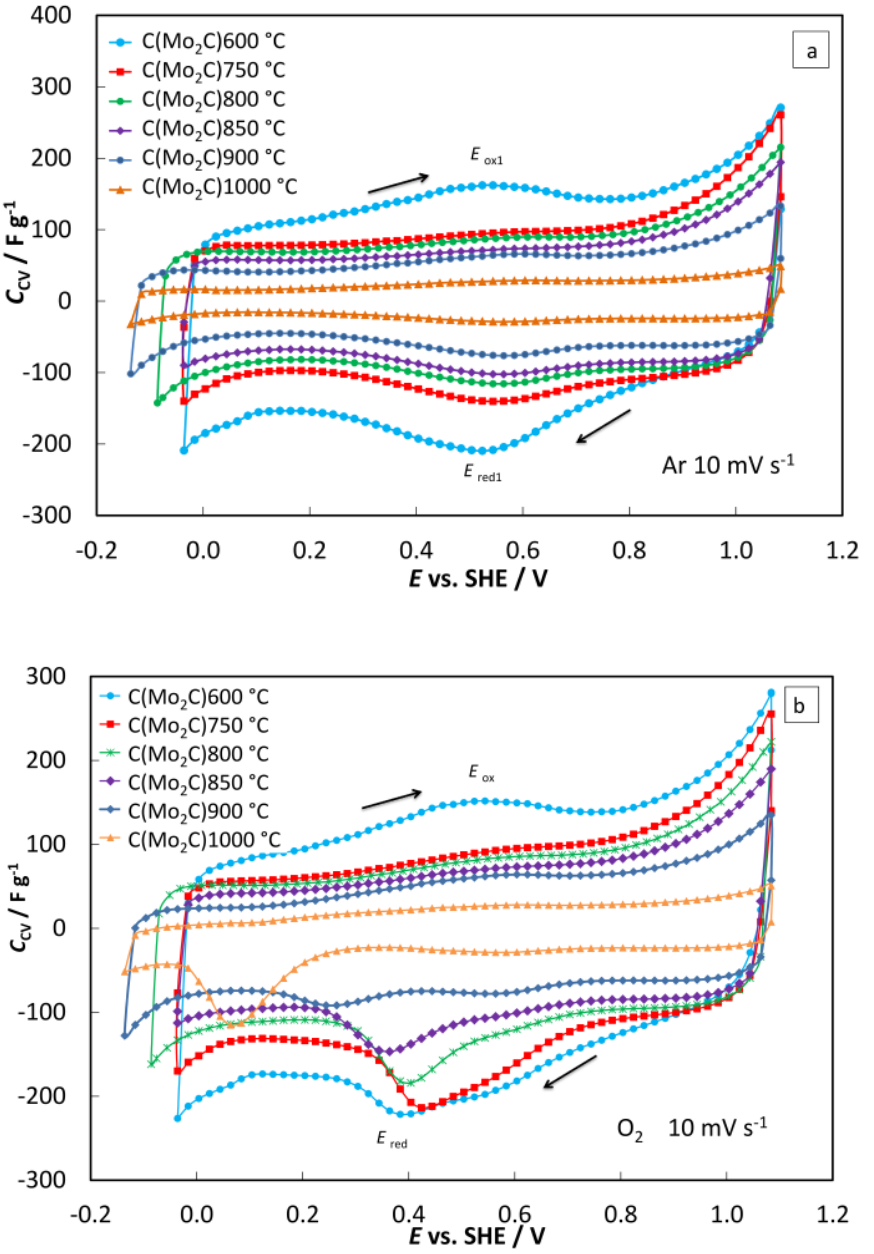
a
C(Mo2C)600 °C
C(Mo2C)750 °C
C(Mo2C)800 °C
C(Mo2C)850 °C
C(Mo2C)900 °C
C(Mo2C)1000 °C
E ox1
E red1
Ar 10 mV s-1
CCV / F g-1
E vs. SHE / V
b
E ox
E red
O2 10 mV s-1

Figure 11 (a, b)

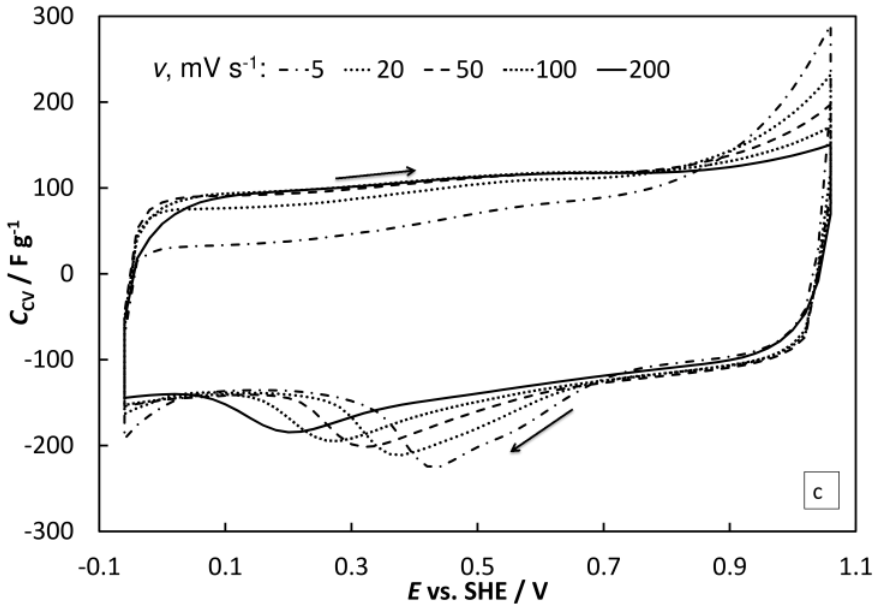

Figure 11. Calculated capacitance C_{CV}, E-plots for C(Mo_2C) electrodes (noted in figure) (a) in Ar-saturated and (b) O_2-saturated 0.5 M H_2SO_4 solution. (c) C_{CV}, E-plots for C(Mo_2C)750 °C in 0.5 M H_2SO_4 O_2-saturated solution at different v (mV s^{-1}, noted in figure).

For O_2-saturated systems, a wide electroreduction current (capacitance) maximum in the C_{CV}, E curve (Fig. 11b) can be seen at peak potentials E_{red} < 0.6 V (vs. SHE) for C(Mo_2C) electrodes. For C(Mo_2C) synthesized at 600 °C < t_{synt} < 850 °C, E_{red} is shifted moderately towards less positive values indicating the decrease in catalytic activity with the increase in t_{synt}. The C(Mo_2C)1000 °C has a very low positive value of E_{red} indicating that partially graphitized carbons are relatively inactive ORR catalysts. The C_{CV}, E curves (Fig. 11c) measured at different potential scan rate for O_2-saturated C(Mo_2C)750 °C system show that within the peak potential area C_{CV} remarkably depends on v. Thus, the pseudocapacitive behaviour, i.e. high values of C_{CV} (Fig. 11a, b) calculated at $E \leq 0.7$ V (vs. SHE), indicates that C(Mo_2C)600 °C, C(Mo_2C)750 °C and C(Mo_2C)800 °C could be used as a negatively charged electrode for pseudo-capacitive supercapacitor with high energy density.

Data presented in Fig. 11c show that with the increase of scan rate, E_{red} shifts noticeably towards less positive potential, indicating that there is a slow faradic electroreduction reaction of O_2 and/or surface oxides with mixed kinetics mechanism. There are no clearly visible oxidation peaks near E_{red}, indicating that the overvoltage for carbon surface oxidation reaction is high. Only for most active C(Mo_2C)600 °C, a wide oxidation peak was observed at E_{ox} ~ 0.5 V (vs. SHE) (Fig. 11b), shifted more than 150 mV towards more positive potential compared with the E_{red}. Thus, the surface oxide formation at C(Mo_2C) electrodes is a slow process.

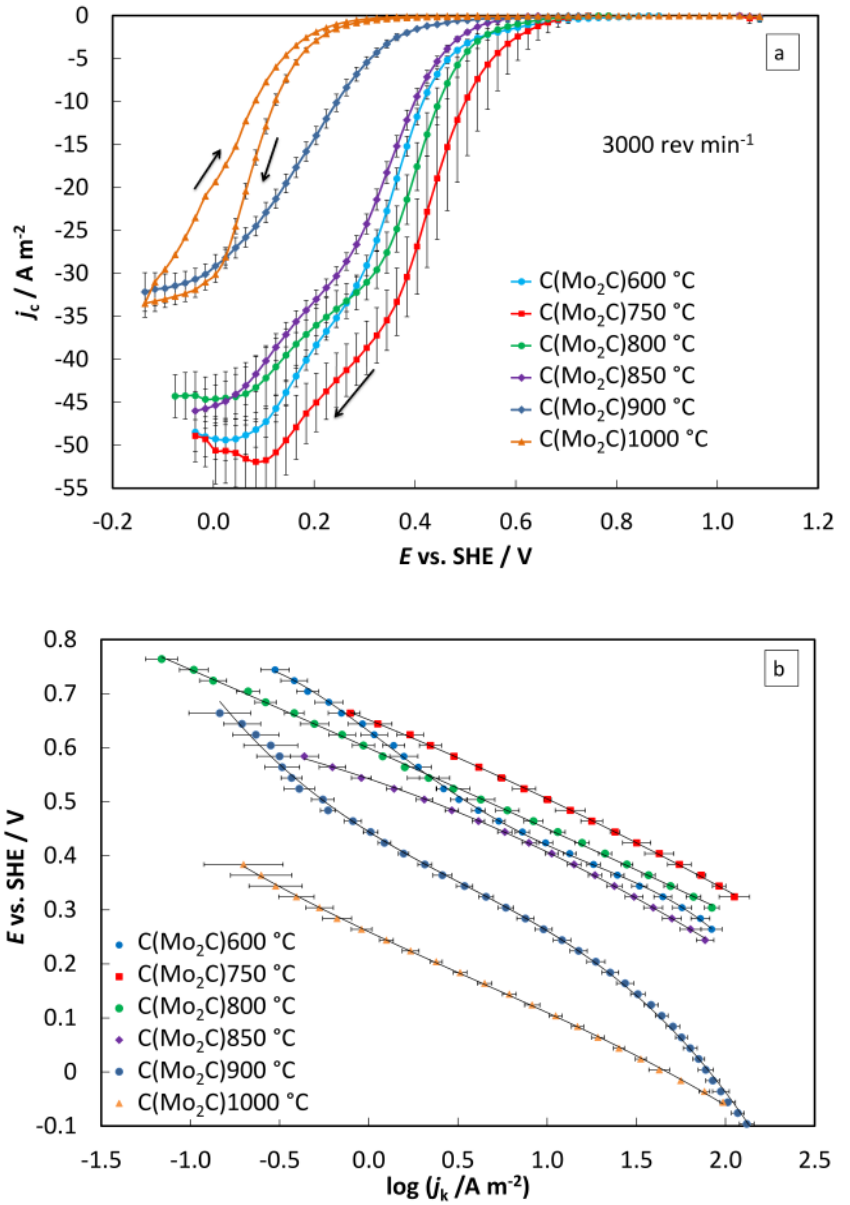

Figure 12. RDE data corrected with background current densities (a) for $C(Mo_2C)$ electrodes (noted in figure) at 3000 rev min^{-1} in 0.5 M H_2SO_4 solution. (b) Tafel plots calculated from RDE data in 0.5 M H_2SO_4 solution.

Very high current densities were measured for C(Mo_2C)750 °C and C(Mo_2C)600 °C electrodes (Fig. 12a) using the RDE method. The statistically treated RDE data in Fig. 12a show noticeable decrease in ORR current densities, j_c (corrected for Ar-saturated electrolyte data), and half wave potential, $E_{½}$, (Table 3) for C(Mo_2C)900 °C and C(Mo_2C)1000 °C, compared with the C(Mo_2C)800 °C, C(Mo_2C)850 °C and C(Mo_2C)750 °C. This behaviour can be explained by considering that the structure of C(Mo_2C)900 °C and C(Mo_2C)1000 °C is more ordered and less amorphous and has a lower surface micro-roughness.

Table 3. Kinetic parameters ORR from RDE data for C(Mo_2C) electrodes.

Parameter/ material	***n***	***E*½ vs. SHE/V**
C(Mo_2C)600 °C	3.3±0.2	0.33
C(Mo_2C)750 °C	3.2±0.1	0.41
C(Mo_2C)800 °C	2.8±0.2	0.38
C(Mo_2C)850 °C	3.0±0.1	0.31
C(Mo_2C)900 °C	2.3±0.1	0.16
C(Mo_2C)1000 °C	2.3±0.1	0.08

However, in addition to the microporosity-mesoporosity effect, the much higher values of j_c for C(Mo_2C)600 °C and C(Mo_2C)750 °C compared with the C(Mo_2C)1000 °C can also be explained by the more pronounced redox transformation of the electrochemically active surface groups. The value of $E_{½}$ (Table 3) is shifted nearly 330 mV toward more positive potential, demonstrating the higher catalytic activity of C(Mo_2C)750 °C compared with the C(Mo_2C)1000 °C. It is well established that the defect amorphous areas and the edge planes are more active toward ORR compared with the basal C(0001) plane [7,19]. Thus, based on the data in Table 3, established values of $E_{½}$ for C(Mo_2C)600 °C, C(Mo_2C)750 °C and C(Mo_2C)800 °C lie within the potential region for practical ORR electrodes [7,24,26,38] and materials under study can be used for development of PEMFCs.

The RDE data were analysed using the Koutecky-Levich equation (Eq. 20). For C(Mo_2C) electrodes, number of electrons transferred (calculated from K-L plots) varies from 2.3 (C(Mo_2C)1000 °C) to 3.3 (C(Mo_2C)600 °C) (Table 3), in good agreement with the data for other unmodified CDC electrodes [7,19,105,106,108]. The decrease in n with increasing t_{synt} indicates that the amorphous structure combined with well-developed microporosity-mesoporosity is needed for the reduction of H_2O_2 to H_2O, which is effective only on C(Mo_2C)600 °C and C(Mo_2C)750 °C electrodes.

The Tafel (E, log j_k) plots were calculated from the value of j_k, using linear extrapolation of K-L plots with the condition $\omega^{-½} \rightarrow 0$. The slope of the Tafel plots, b, (Fig. 12b) depends on t_{synt} as well as on potential applied, i.e. on the ORR overvoltage. The Tafel plots are linear within kinetic current densities region $0.1 \leq (\log j_k / \text{A m}^{-2}) \leq 1.5$ and the calculated values of Tafel slope range from –125 to –155 mV, depending on the porosity of the electrode material tested.

EIS data (Fig. 13a,b) demonstrate nearly capacitive behaviour in the low AC frequency region, explained by the quick ORR followed by the slow electrical double-layer (EDL) formation step, limited by the adsorption rate of ions, intermediates and/or reaction products at/inside microporous-mesoporous C(Mo_2C) electrodes. The high-frequency series resistance is almost independent of t_{synt}. The phase angle, log f- and log |-Z''|, log f-plots (Fig. 13c) illustrate that there is nearly ideal blocking capacitive behaviour (the slope of |-Z''|, log f-plots are lower than –0.96) at $f \leq 10$ Hz[5,55,98,105,106,111].

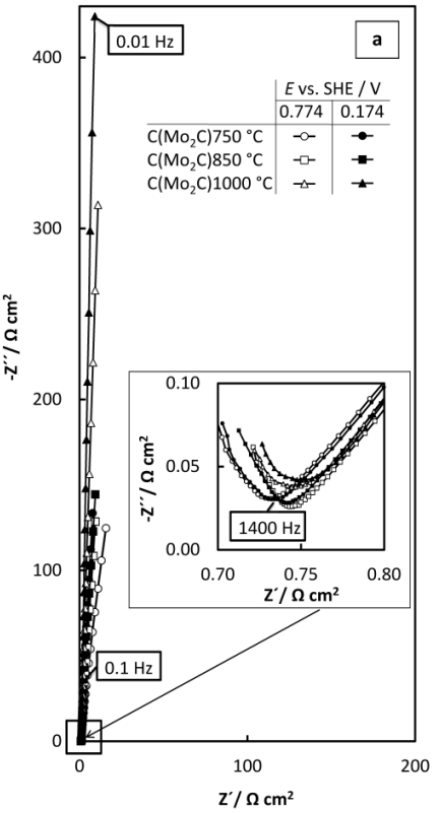

Figure 13 (a)

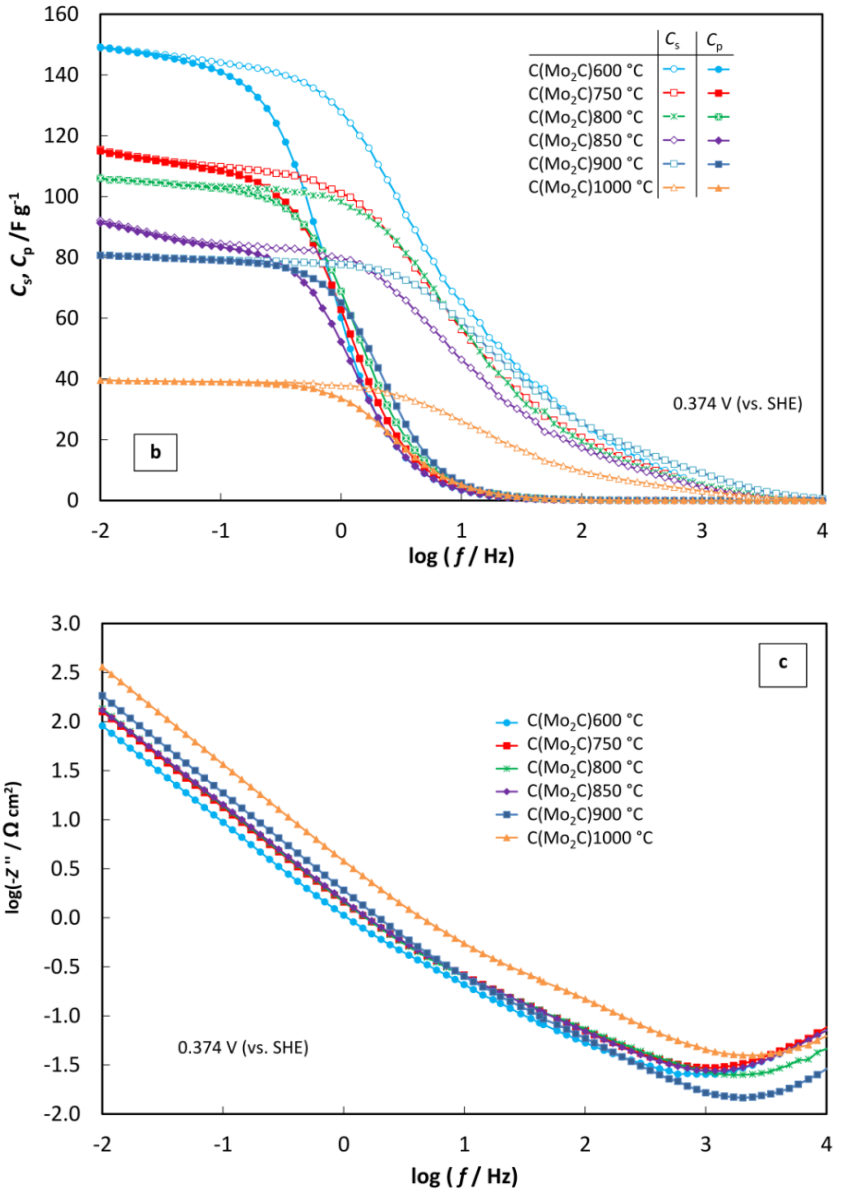

Figure 13. (a) Nyquist plots for C(Mo$_2$C) systems at different E, noted in figure, (b) C_s, log f and C_p, log f-plots for C(Mo$_2$C) systems (noted in figure) at 0.374 V (vs. SHE), (c) log(-Z''),log f-plots in 0.5 M H_2SO_4 Ar-saturated solution.

6.3 Electrochemical characterization of Pt-C(Mo_2C) electrodes

Data in Figs. 14a–b indicate that cyclic voltammograms with typical shape were obtained for Pt-C(Mo_2C) electrodes. The current densities increase quickly in two regions, which is explained by the reduction of surface oxides (Fig.14a) and ORR (Fig. 14b) at potentials from 1.0 to 0.6 V (vs. SHE) and by the cathodic electroreduction of H_3O^+-cations and hydrogen adsorption at $E < 0.3$ V (vs. SHE). For Pt-C(Mo_2C) electrodes, the so-called EDL region was observed in the potential range $0.3 < E < 0.6$ V (vs. SHE), which is explained by the blocking adsorption of ions on Pt-nanoclusters in Ar-saturated solution (Fig. 14a) and by the adsorption of ORR intermediates and ions on Pt-nanoclusters in O_2-saturated solution (Fig. 14b). The butterfly-shaped hydrogen evolution peaks (Fig. 14a) were used for the calculation of the so-called electrochemically active surface area values ($ECA = Q_{cal}/Q_{Pt-poly}$, where Q_{cal} is calculated charge required for hydrogen adsorption from the Pt surface and $Q_{Pt-poly} = 210$ μC cm^{-2} corresponds to polycrystalline Pt surface) [28,96,108], given in Table 4. Traditionally for porous electrodes, *ECA* depends somewhat on the potential scan rate applied. Based on the collected data, the highest electrochemical activity was established for Pt-C(Mo_2C) 800 °C and Pt-C(Mo_2C) 850 °C electrodes. It can be explained by the optimal ratio of S_{meso}/S_{micro} and V_{meso}/V_{micro} values [5,70,97–99,105,106], and existence of some defected amorphous catalytically active and not very well crystallised carbon areas, exposed at the electrode surface.

Nearly pseudocapacitive behaviour [5,19,97–100,104–108] was established for Pt-C(Mo_2C) (Fig. 14b) electrodes as the C_{CV} values, calculated for O_2-saturated systems (Fig. 14b), weakly depend on the potential scan rate, especially within the potential region from 0.6 V to 0.3 V (vs. SHE). A weak dependence of C_{CV} on v indicates the dominating pseudocapacitive behaviour for Pt-C(Mo_2C) electrodes. Comparison of CV data for C(Mo_2C) (Fig. 11b) and Pt-C(Mo_2C) (Fig. 14b) electrodes in O_2-saturated solutions shows that for Pt-C(Mo_2C) systems the increase of $|j|$, that is induced by ORR, is shifted towards more positive E, and only slightly higher values of j and C_{CV} (Fig. 14b) were obtained within the region $E \leq 0.3$ V (vs. SHE), where the hydrogen adsorption and evolution is prevalent.

After correction of the current density values with Ar-saturated solution current density data, RDE curves (Fig. 15a) characteristic of mixed kinetic processes (within potential range from 0.9 to 0.7 V (vs. SHE)) were observed. A diffusion limited process (within potential range from 0.5 to 0.05 V (vs. SHE)) were observed and intensive cathodic hydrogen evolution occurs at $E \leq 0.05$ (vs. SHE). RDE data in Fig. 15a show that j_c depends on the carbon support characteristics, and the highest values of j_c were measured for Pt-C(Mo_2C) 800 °C catalyst. Comparison of the data for C(Mo_2C) (Fig. 12a) and Pt-C(Mo_2C) (Fig. 15a) electrodes demonstrates noticeably higher catalytic

activity of Pt-C(Mo_2C) electrodes. The electrochemical activity of Pt-C(Mo_2C) electrodes is somewhat higher than for Pt-Vulcan®XC72 electrodes [6–8,24, 60,106,112,113], explained by the more higher S_{BET}, optimal ratio of V_{micro}/V_{meso} and S_{micro}/S_{meso}, as well as by better electrical conductivity of partially graphitized C(Mo_2C), especially for materials prepared at $t_{synt} \geq 800$ °C.

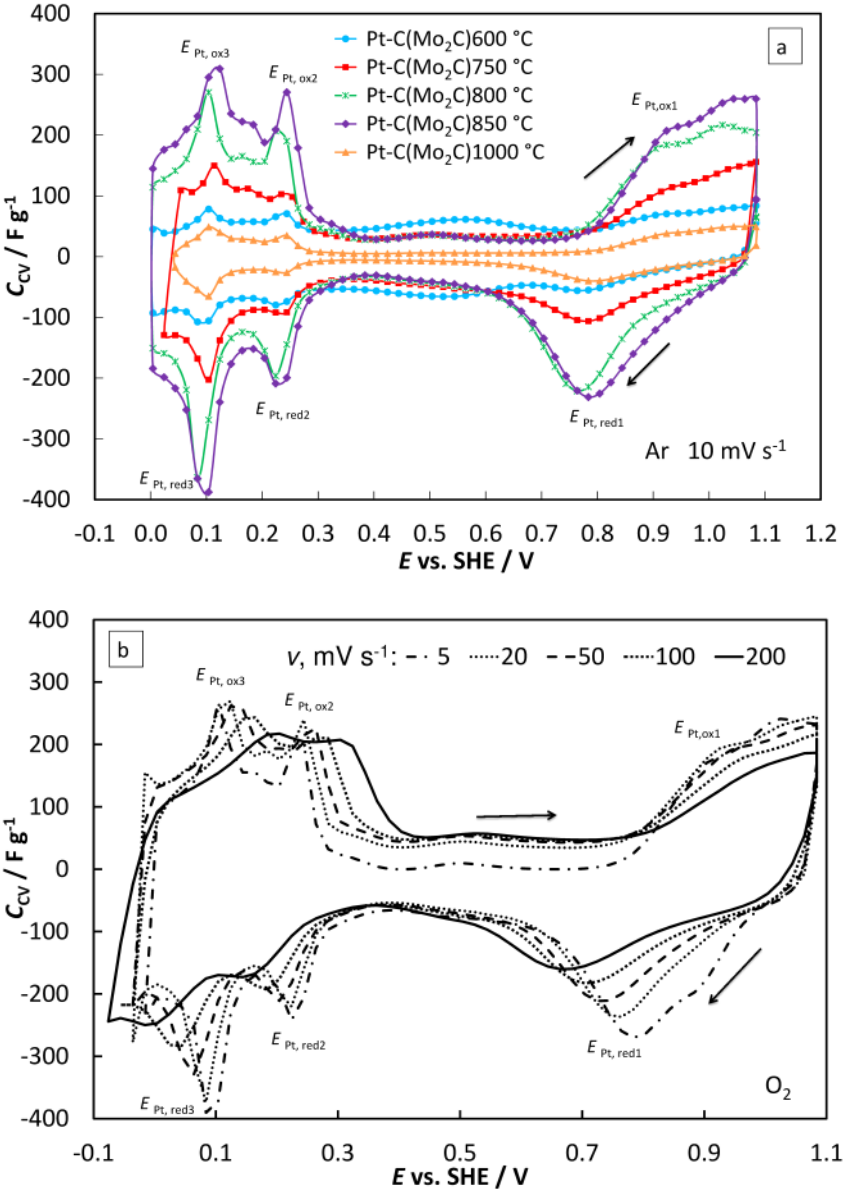

Figure 14. Calculated capacitance C_{CV}, E-plots for Pt-C(Mo_2C) electrodes (noted in figure) in 0.5 M H_2SO_4 solution (a) in Ar-saturated and (b) O_2-saturated systems, at different v (mV s^{-1}, noted in figure).

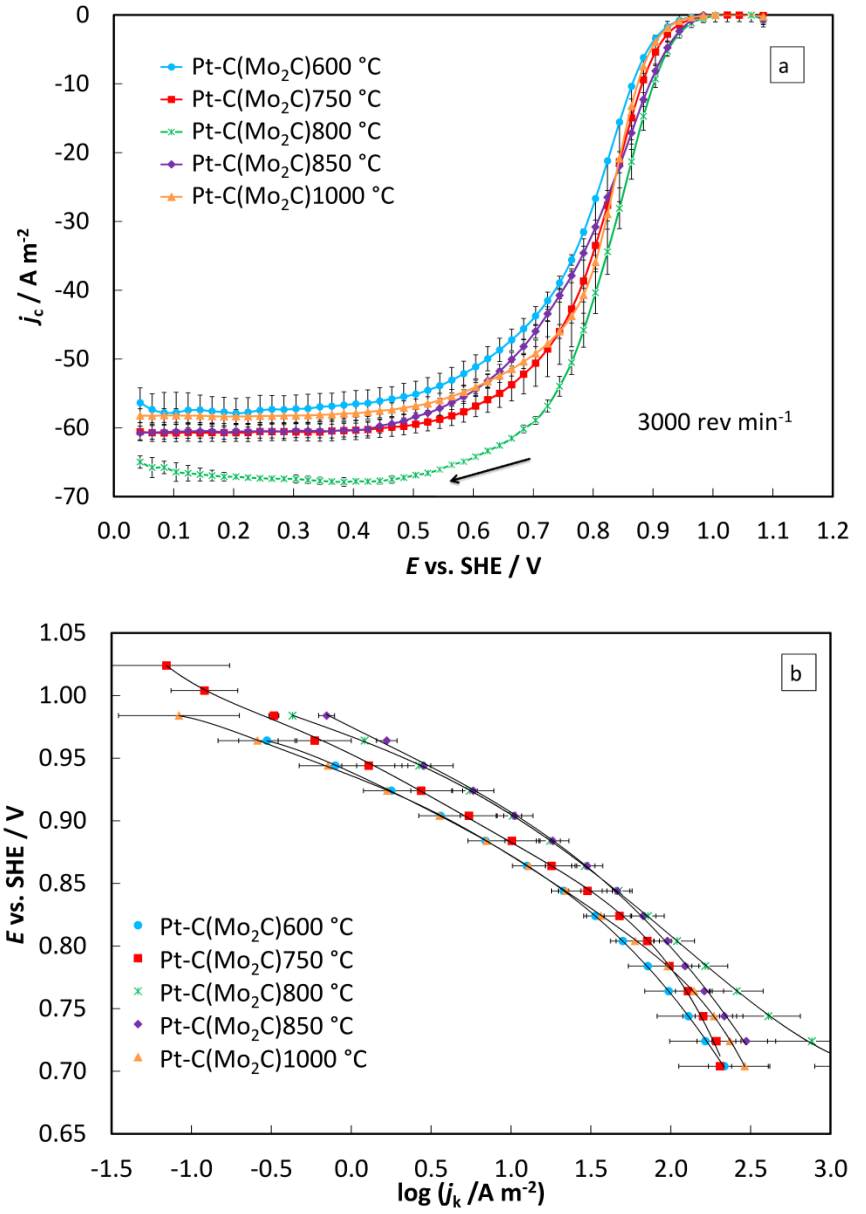

Figure 15. RDE data corrected with background current densities (a) for Pt-C(Mo_2C) electrodes (noted in figure) at 3000 rev min^{-1} in 0.5 M H_2SO_4 solution. (b) Tafel plots calculated from RDE data in 0.5 M H_2SO_4 solution.

The half-wave potential depends on the microporosity-mesoporosity of the carbon support (Table 4). The most positive $E_{½}$ was established for Pt-C(Mo_2C)800 °C.

The linear Levich plots, calculated from the cathodic potential scan direction at $E < 0.6$ V(vs. SHE) for Pt-C(Mo_2C), are characteristic of a diffusion limited process. The K-L plots, calculated from the cathodic potential scan direction of the RDE data for Pt-C(Mo_2C) ($0.70 < E < 0.90$ V (vs. SHE)) electrodes, are linear and the intercepts (j_k) of the extrapolated K-L plots depends on the potential applied. The number of electrons (Table 4) for Pt-C(Mo_2C) electrodes, calculated from the linear K-L plots, is roughly four and is in good agreement with literature data [43,67,114,115].

Table 4. Kinetic parameters from CV and RDE data for Pt-C(Mo_2C) electrodes.

Parameter/material	***ECA*, $m^2\ g^{-1}$**	***n***	**$E_{½}$ vs. SHE/V**
Pt-C(Mo_2C)600 °C	3.4±0.3	3.3±0.1	0.80
Pt-C(Mo_2C)750 °C	14±1.4	3.7±0.1	0.82
Pt-C(Mo_2C)800 °C	23.9±3.2	3.6±0.1	0.83
Pt-C(Mo_2C)850 °C	29.7±2.1	3.3±0.1	0.81
Pt-C(Mo_2C)1000 °C	7.0±0.3	3.3±0.1	0.82

The Tafel-like plots (log j_k, E) (Fig. 15b) suggest that the slope values of Tafel-like plot, b, slightly depend on the porosity parameters of the support, i.e. on the carbon material t_{synt}. The log j_k, E dependences are linear only in a narrow potential region and therefore the b value can be calculated only at $E > 0.85$ V (vs. SHE) (low kinetic current density region). The calculated b values (–110±10 mV) are practically independent of the electrode studied. The calculated b value for Pt-C(Mo_2C) electrodes is nearly the same as b values obtained for Pt or Ru electrodes [65,66,93,116]. In the lower potential region (at higher current densities), the value of b gradually increases for all Pt-C(Mo_2C) systems, and is comparable to those observed for layered Pd electrode deposited onto Pt(111) [44], Pt-Ru alloy and Ru(*hklf*) electrodes at $E < 0.75$ V (vs. SHE) [42]. The change in b value can be attributed to a change from Langmuir mechanism (at low j_k [65,66,93,116]) to a more complicated ORR mechanism [11,42,44,65,66,98,106,111,116–120] in the high current density region. The dependence of the value of b on the potential applied indicates that the number of electrons transferred for Pt-C(Mo_2C)600 °C and Pt-C(Mo_2C)800 °C systems depends noticeably on the kinetic current densities (Fig. 15b).

Impedance data given in Figs. 16a,b show that at low AC frequency $f \leq 1$ Hz, nearly blocking capacitive behaviour [5,55,98,99,105,106,111] was observed. The values of limiting series and parallel capacitance (Fig. 16b) are overlapping at $f \leq 0.5$ Hz indicating that in addition to PEMFC catalysts, the Pt-C(Mo_2C) materials can be used as pseudocapacitor electrodes for energy storage.

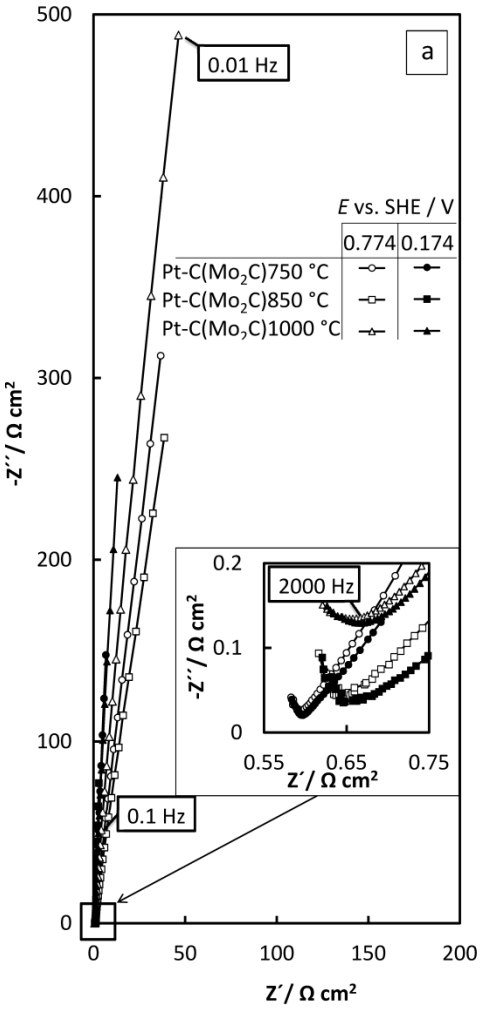

Figure 16 (a)

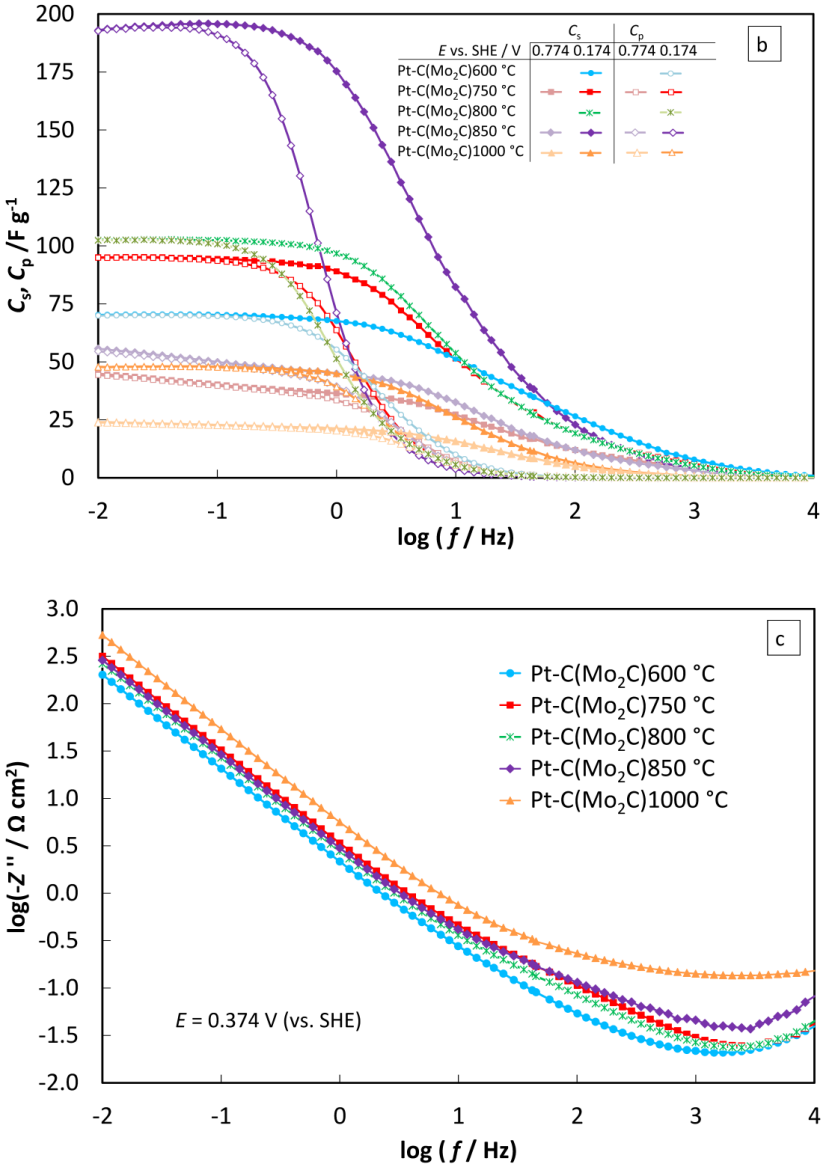

Figure 16. (a) Nyquist plots for Pt-C(Mo_2C) systems at different E, noted in figure, (b) C_s, log f- and C_p, log f-plots for Pt-C(Mo_2C) systems (noted in figure) at 0.374 V (vs. SHE), (c) log(-Z´´),log f-plots in 0.5 M H_2SO_4 Ar-saturated solution.

6.4 Electrochemical characterization of Pt-Ru-C(Mo_2C) electrodes

CV data measured in Ar- and O_2-saturated 0.5 M H_2SO_4 solution at different v are presented in Fig. 17a for Pt-Ru-C(Mo_2C)600 °C and in Fig. 17b for comparison the corresponding data for C(Vulcan) and Pt-Ru-C(Vulcan) electrodes are given. Capacitance C_{CV}, E-curves for Pt-Ru-C(Mo_2C)600 °C [5] show that similarly to Ru/RuO_2 electrode [56,57,121–124], nearly pseudocapacitive behaviour was established for Ar- and O_2-saturated systems, explained by the faradic processes limited by adsorption step rate at very large specific surface area electrode. Nearly exponential increase in current density (and C_{CV}) was established only at $E < 0.1$ V (vs. SHE), caused by the cathodic hydrogen evolution from acidic 0.5 M H_2SO_4 solution (Fig. 17a). The lower S_{BET} (Table 1) for C(Vulcan) based system is main reason why the current densities and capacitance values are lower (Fig. 17b) than for that C(Mo_2C) based systems within all the potential region studied (Fig. 17a).

The values of C_{CV} only weakly depend on the potential scan rate applied [5], similarly to other microporous-mesoporous carbon electrodes [97,125,126] and for Ru/RuO_2 system [55–57]. No diffusion limited processes occur in Ar-saturated 0.5 M H_2SO_4 solution. Thus, mainly surface processes (adsorption, absorption, partial and faradaic charge transfer) determine the current density and electrode capacitance values for stationary electrode (including double layer capacitance, C_{dl}, adsorption capacitance, C_{ad}, and faradaic capacitance, C_{far} values). Virtually pure pseudocapacitive behaviour is exhibited [55,56,124] at more positive potentials than 0.8 V [55–59,121–124] caused by formation of RuO_2 in a hydrous state.

The nearly pseudocapacitive behaviour of Pt-Ru-C(Mo_2C)600 °C (probably obtained mainly by the pseudocapacitive behaviour of RuO_2, and supported by C_{dl} and C_{ad} as well) is surprising because the CV data approach nearly capacitive behaviour, having almost constant $C_{CV} \geq 0.8$ F cm^{-2}, observed within potential range from 0.4 to 0.8 V vs. SHE, albeit with some small but discernable maxima (Fig. 5d in [5]) at $E = 0.45$ (vs. SHE) in reduction curve. Thus, the almost constant capacitance arises from the overlap of several redox processes with C_{far}, C_{dl} and C_{ad} at Pt-Ru- C(Mo_2C)600 °C in the potential range under study. For RuO_2, three successive redox stages can be recognised that involve oxidation states Ru^{4+}, Ru^{3+} and Ru^{2+} (even Ru^{6+} at very high potential values), however not very well separable for Pt-Ru-C(Mo_2C)600 °C or Pt-Ru-C(Vulcan) electrodes.

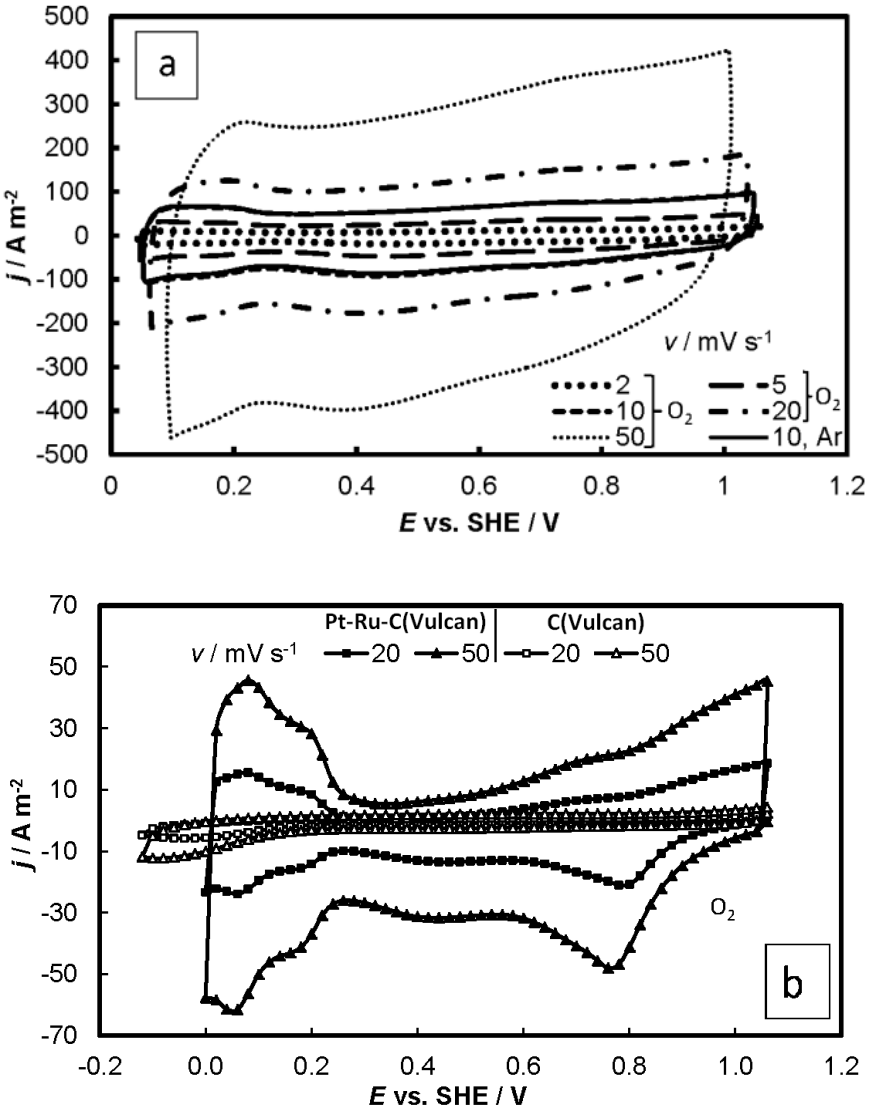

Figure 17. CVs for (a) Pt-Ru-C(Mo_2C)600 °C (Ar-saturated and O_2-saturated), and (b) Pt-Ru-C(Vulcan) and C(Vulcan) electrodes (O_2-saturated) in 0.5 M H_2SO_4 solution at different *v* (mV s-1), noted in figure.

Thus, nearly reversible redox processes reveal in the CVs (Fig. 17a) and capacitance plots for the electrochemically formed RuO_2 film on Pt-Ru-C(Mo_2C)600 °C associated with overlapping the redox processes, probably involving different oxidation states of Ru in RuO_x. Differently from Pt or Au electrodes [16,58,59,61–66,109,112,127,128], the CVs for Pt-Ru-C(Mo_2C)600 °C do not involve any stage of reduction of RuO_x to Ru^0, i.e. to the bare Ru electrode

surface similarly to Ru/RuO_2 [55]. Of course, in parallel with C_{far}, noticeable amount of charge is accumulated due to double layer charging of the extended microporous-mesoporous carbon, and hydrous oxide surface, as well as adsorption capacitance of sulfate or bisulfate anions onto Pt-Ru-C(Mo_2C)600 °C surface. It has been well established that the adsorbed (bi)sulfate anions are blocking O_2 adsorption sites and thereby hindering the ORR at Pt [65,66] or Ru (RuO_2) surface.

High current densities as well as hysteresis in that case of Pt-Ru-C(Mo_2C)600 °C electrode are mainly caused by the more expressed microporous-mesoporous nature of the C(Mo_2C) support (Table 2). Comparison of current densities for CDC and C(Vulcan) based electrodes indicates noticeably more active ORR at C(Mo_2C) and Pt-Ru-C(Mo_2C)600 °C) than that at C(Vulcan) or Pt-Ru-C(Vulcan) catalysts. The half wave potential for the Pt-Ru-C(Mo_2C)600 °C electrode is ~0.75 V (vs. SHE) (Fig. 18a), which is close to $E_{½}$ values obtained for Pt monolayer on Au(111), $Pt_{0.75}Pd_{0.25}$ alloy monolayer on Vulcan® XC72 support [43] or for Se-Ru-Mo-C electrode [48]. In our case $E_{1/2}$ is more positive than that obtained for Pt-Ru(*hklf*), Au(*hklf*), $Pt_{1.5}$ monolayer+Ru-C, Ru/C [42] and Se-Ru catalyst (9% Ru on carbon black, Vulcan® XC72, Cabot Corp.) [116]. Thus, the $E_{½}$ value for Pt-Ru-C(Mo_2C)600 °C system is in the region of potential for applicable ORR electrodes [118].

The slopes of Tafel plots (Fig. 18b) somewhat depend on the electrode potential, indicating that in the region of mixed kinetics the number of electrons *n* transferred (Fig. 18b, inset) depends on potential. Based on data in Fig. 18b, only at $E > 0.70$ V (vs. SHE) (low ORR current density region), the value of b –109±5 mV dec^{-1} is comparable or somewhat lower than it is typical for Pt or Ru electrodes [40–43]. In the region of higher kinetic current densities (i.e. at higher overpotential) the value of b gradually increases and only at $E < 0.60$ V (vs. SHE) it stabilises at –240±10 mV dec^{-1}, comparable to Pd electrodes deposited onto Pt(111) [44] or for Pt-Ru alloy and Ru(*hklf*) electrodes (calculated at $E < 0.75$ V (vs. SHE) [43]). The change in b can be attributed to a change from Langmuir mechanism [25,118,129–132] to a more complicated mixed kinetic ORR mechanism.

EIS data, given in Fig. 19, show that in the region of high AC frequencies ($f \geq 1000$ Hz) Pt-Ru-C(Mo_2C)600 °C system demonstrates nearly pure resistive behaviour, i.e. phase angle θ values are nearly 0°. Only a very small depressed semicircle in Nyquist plots can be seen at intermediate AC frequency region (500 Hz $\leq f \leq$ 10000 Hz). Surprisingly in this region, the Nyquist and Bode plots depend weakly on potential applied, but the shape of plots is independent of the concentration of oxygen in 0.5 M H_2SO_4 solution. The R_s values have been calculated at $f \geq 3000$ Hz and used for ohmic drop correction of CV and RDE data. At lower AC frequencies $f < 1$ Hz, log Z' and log $|Z|$ values increase with the rise of potential, thus, with the decrease of the ORR rate, i.e. ORR current. High negative θ values from –82 to –90° at $f \leq 0.1$ Hz and the slope value from –0.85 to –0.88 (vs. SHE) [5], obtained from log $|-Z''|$, log f plots

[111] at $f \leq 5$ Hz, can be explained by mainly adsorption step limited faradaic pseudocapacitive processes at Pt-Ru-C(Mo_2C)600 °C electrode, similarly to Ru/RuO_2 electrode in H_2SO_4 solution [55–57,121–124]. Surprisingly in these regions of AC frequency and potential, the adsorption limited pseudocapacitive processes are slow and prevail at the Pt-Ru-C(Mo_2C)600 °C surface.

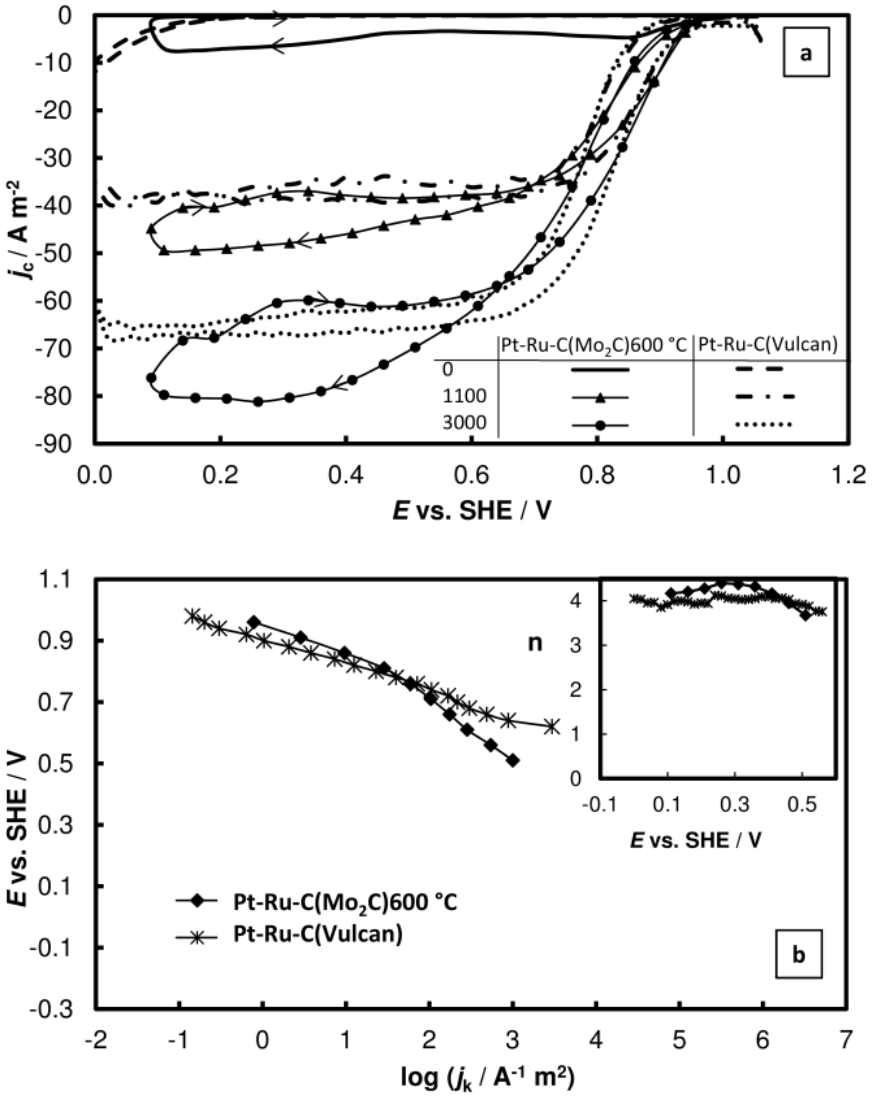

Figure 18. RDE data corrected with background current densities for ORR on Pt-Ru-C(Mo_2C) and Pt-Ru-C(Vulcan) in 0.5 M H_2SO_4 solution (a) at different electrode rotating speeds (rev min^{-1}), noted in figure. (b) Tafel plots calculated from RDE data in 0.5 M H_2SO_4 solution. Inset: potential dependence of the number of electrons (n) transferred for ORR obtained from Levich plots.

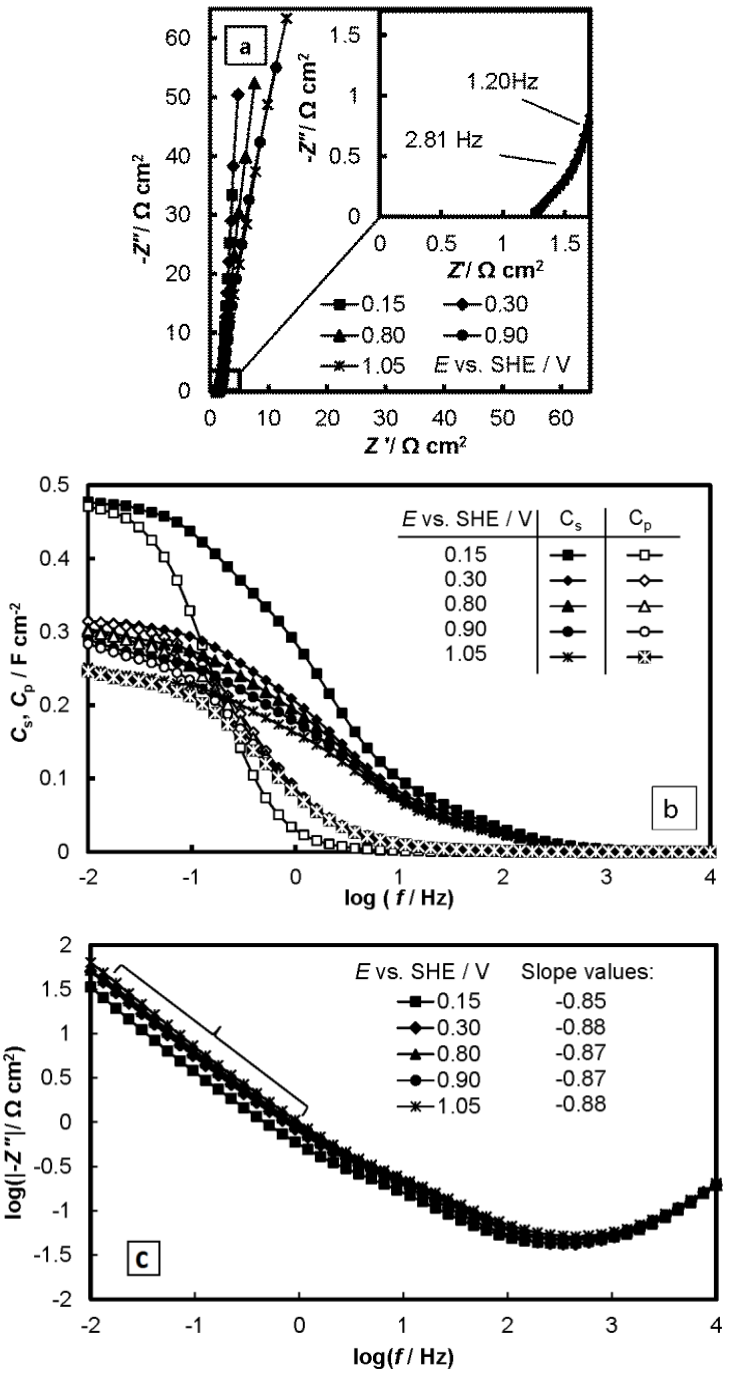

Figure 19. (a) Nyquist plots for Pt-Ru-C(Mo_2C)600 °C at different E, noted in figure, (b) C_s, log f- and C_p, log f-plots for Pt-C(Mo_2C) systems (noted in figure) at 0.374 V (vs. SHE), (c) log(-Z´´),log f-plots in 0.5 M H_2SO_4 Ar-saturated solution.

It should be noted that comparable behaviour of Nyquist and Bode plots for mixed RuO_2-TiO_2 electrodes in 5 M aqueous solution of NaCl (298 K, open circuit conditions) has been established by Tilak et al. [132], if RuO_2 content is higher than 20 wt%, explained by pseudocapacitive behaviour of RuO_2 at lower AC frequencies $f < 0.5$ Hz. These results show that added TiO_2 intimately influences RuO_2-TiO_2 pseudocapacitive behaviour [55,115,132,133].

Very high values of series capacitance C_s ($f \to 0$) and parallel capacitance C_p, ($f \to 0$) calculated from Nyquist plots have been obtained (Fig. 19b). At $f \to 0$, C_s, $\log f$- and C_p, $\log f$-dependencies overlap, indicating nearly so called blocking capacitive electrode behaviour [70,71,97,111,126,134–136]. The values of C_s and C_p increase noticeably with the decrease in the potential applied. The values of C_s and C_p are somewhat higher than those obtained for C(Mo_2C) electrode in neutral Na_2SO_4 or H_2SO_4 aqueous solution. Thus, in addition to PEMFC electrodes, these electrodes can be used as pseudocapacitive electrodes in hybrid H_2SO_4 electrolyte based supercapacitors [136–138] for peak power generation regime in combined electrochemical devise.

The hydrogen evolution (limited by Volmer reaction, i.e. by the rate of adsorption step of hydrogen) [138] occurs at Pt-Ru-C(Mo_2C)600 °C, at $E < 0.3$ V (vs. SHE).

However, for separation of electrical double layer formation, specific SO_4^{2-}(or HSO_4^-) ion adsorption [139], ORR and hydrogen evolution processes, the experimental studies in solutions with different anion chemical composition and pH are inevitable.

7. SUMMARY

In this thesis the oxygen electroreduction (ORR) on different carbon and Pt and Pt based binary catalysts deposited onto carbon support has been studied. The kinetic parameters for ORR have been determined.

The main aim of this work was to study the influence of the micro- and mesoporosity, pore size distribution and crystallinity (amount of amorphous and graphitic layers) of different carbide-derived carbon (CDC) materials on the ORR kinetics. The CDC materials were prepared from Mo_2C (noted as C(Mo_2C)) at six different chlorination temperatures (t_{synt}) from 600 °C to 1000 °C. Pt-nanoclusters and Pt-Ru alloy nanoparticles were deposited onto/into C(Mo_2C) powders using sodium borohydride reduction method.

All electrochemical studies were made in 0.5 M H_2SO_4 solution using the cyclic voltammetry (CV), rotating disk electrode (RDE) and the electrochemical impedance spectroscopy (EIS) methods.

Raman spectroscopy, X-ray diffraction, high-resolution transmission electron microscopy, selected-area electron diffraction and the electron energy loss spectroscopy methods were applied for the structural and morphological characterization, and the nitrogen sorption method was used for the porosity analysis. The morphology, specific surface area (S_{BET}), microporosity-mesoporosity and electrical conductivity of the materials studied noticeably depend on t_{synt} applied for production of CDC. Based on the very high kinetic current densities measured for the C(Mo_2C) material synthesized at t_{synt} 750, 800 and 850 °C, it can be concluded that these supports have the optimal micro- and mesoporous structure for ORR.

The cathodic current densities and half-wave potentials strongly depend on t_{synt} and the porosity of C(Mo_2C). Thus, the comparison of different C(Mo_2C) supports indicates that, in addition to the high S_{BET}, the crystallinity and morphology of the carbon particles noticeably influence the rate of ORR. This is apparent in the case of 600 °C $\leq t_{synt} \leq$ 850 °C, where the difference in S_{BET} is negligible, however the electrochemical properties widely vary. The number of electrons transferred per electroreduction of one molecule of O_2 ($2.3 \leq n \leq 3.3$) depends noticeably on the microporosity-mesoporosity and structure of the C(Mo_2C) electrode, indicating that the reaction kinetics depends on the properties of the porous carbon powder studied.

EIS data demonstrate nearly capacitive behaviour for C(Mo_2C) electrodes in the low AC frequency region, which could be explained by the quick cathodic ORR followed by a slow adsorption step of ions and intermediates at/inside the microporous-mesoporous C(Mo_2C).

The results of this study indicate that the size of the deposited Pt-nanoclusters depends on the porosity and crystallinity parameters of the C(Mo_2C) support.

Very high values of ORR current density were calculated for Pt-C(Mo_2C)800 °C. The number of electrons transferred, calculated from linear

Koutecky-Levich plots, varies from 3.3 to 3.7. Thus, the so called 'direct' four electron process mechanism, however, with some deviations, was observed. The electrochemically active surface area, calculated from CV data within the H_3O^+ adsorption/desorption region, is high (from 14 to 30 m^2g^{-1}) for Pt-C(Mo_2C)750 °C, Pt-C(Mo_2C)800 °C and Pt-C(Mo_2C)850 °C compared with Pt-C(Mo_2C)600 °C indicates that in addition to high S_{BET} for the C(Mo_2C)600 °C electrode, the optimal ratio of mesoporosity and microporosity, as it was found for the C(Mo_2C)750 °C and C(Mo_2C)800 °C electrodes, is required for very quick electroreduction of O_2 to H_2O in order to avoid noticeable accumulation of H_2O_2 into the Pt-(Mo_2C) catalyst.

However, the EIS data demonstrate the pseudocapacitive behaviour of the Pt-C(Mo_2C) electrodes, which could be explained by the slow limiting adsorption step of the ions and intermediates (mainly H_2O_2) at/inside the Pt-C(Mo_2C) electrodes.

CV and rotating RDE data show very high cathodic oxygen electroreduction and double layer charging current densities for the Pt-Ru-C(Mo_2C)600 °C catalyst. For Pt-Ru-C(Vulcan) electrode somewhat lower ORR kinetic current densities were calculated. The number of electrons transferred per one O_2 molecule (~4) is in good agreement with the literature data.

Analysis of EIS data shows that, similarly to the Ru/RuO_2 system in H_2SO_4 aqueous solution, the nearly pseudocapacitive behaviour within the very low AC frequency region was observed, which is probably caused by the very quick cathodic electroreduction processes (RuO_2 reduction and ORR as well as underpotential deposition of hydrogen, remarkable only at $E < 0.34$ (vs. SHE)), and by specific adsorption of the ions and reaction intermediates at the Pt-Ru-C(Mo_2C) catalyst. The values of the very high series capacitance (C_s) and parallel capacitance (C_p) were established at $E = 0.15$ V (vs. SHE). C_s and C_p noticeably decrease with the rise of the electrode potential (i.e. with the decrease in RuO_2 electroreduction rate), indicating that both C_s and C_p are influenced by the faradaic pseudocapacitance.

Therefore, in addition to applicability in polymer electrolyte membrane fuel cells as ORR cathodes, the Pt-Ru-C(Mo_2C) systems are also interesting materials for pseudocapacitive (i.e. for hybrid supercapacitor) systems or for bifunctional electrochemical power sources combining the properties of the fuel cell and supercapacitor subsystems.

8. REFERENCES

[1] F. Barbir, PEM Fuel Cells. Theory and Practice, Elsevier Inc., United States of America, 2013.

[2] U.S Department of Energy, Office of Fossil Energy, National Energy Technology Laboratory, Fuel Cell Handbook, 7th ed., EG&G Technical Services, Inc., Morgantown, West Virginia, 2004.

[3] B.C.H. Steele, A. Heinzel, Materials for fuel-cell technologies, Nature 414 (2001) 345–352.

[4] R. Bashyam, P. Zelenay, A class of non-precious metal composite catalysts for fuel cells, Nature 443 (2006) 63–66.

[5] K. Vaarmets, S. Sepp, J. Nerut, E. Härk, I. Tallo, E. Lust, Electrochemical and physical characterization of Pt–Ru alloy catalyst deposited onto microporous–mesoporous carbon support derived from Mo_2C at 600 °C, J. Solid State Electrochem. 17 (2013) 1729–1741.

[6] R. Adžić, J. Lipkowski, P.N. Ross, Electrocatalysis, Wiley-VCH, New York, 1998.

[7] K. Kinoshita, Electrochemical oxygen technology, John Wiley and Sons, INC., New York, 1992.

[8] M.R. Tarasevich, A. Sadkowski, E. Yeager, in: B.E. Conway, J.O. Bockris, E. Yeager, S.U.M. Khan, R.E. White (Eds.), Comprehensive treatise of electrochemistry, 7th ed., Plenum Press, New York, 1983.

[9] J.P. Hoare, The electrochemistry of oxygen, Interscience Publishers, New York, 1968.

[10] E. Antolini, Platinum-based ternary catalysts for low temperature fuel cells: Part I. Preparation methods and structural characteristics, Appl. Catal. B Environ. 74 (2007) 324–336.

[11] S. Sharma, B.G. Pollet, Support materials for PEMFC and DMFC electro-catalysts-A review, J. Power Sources 208 (2012) 96–119.

[12] K. Kinoshita, Particle size effects for oxygen reduction on highly dispersed platinum in acid electrolytes, J. Electrochem. Soc. 137 (1990) 845–848.

[13] M. Watanabe, H. Sei, P. Stonehart, The influence of platinum crystallite size on the electroreduction of oxygen, J. Electroanal. Chem. 261 (1989) 375–387.

[14] K. Yahikozawa, Y. Fujii, Y. Matsuda, K. Nishimura, Y. Takasu, Electrocatalytic properties of ultrafine platinum particles for oxidation of methanol and formic acid in aqueous solutions, Electrochimica Acta 36 (1991) 973–978.

[15] A. Kabbabi, F. Gloaguen, F. Andolfatto, R. Durand, Particle size effect for oxygen reduction and methanol oxidation on Pt/C inside a proton exchange membrane, J. Electroanal. Chem. 373 (1994) 251–254.

[16] K.J.J. Mayrhofer, B.B. Blizanac, M. Arenz, V.R. Stamenkovic, P.N. Ross, N.M. Markovic, The impact of geometric and surface electronic properties of Pt-catalysts on the particle size effect in electrocatalysis, J. Phys. Chem. B 109 (2005) 14433–14440.

[17] E. Yeager, Electrocatalysts for O_2 reduction, Electrochimica Acta 29 (1984) 1527–1537.

[18] V. Garten, D. Weiss, The Quinone-Hydroquinone character of activated carbon and carbon black, Aust. J. Chem. 8 (1955) 68–95.

[19] M. Gara, R.G. Compton, Activity of carbon electrodes towards oxygen reduction in acid: A comparative study, New J. Chem. 35 (2011) 2647–2652.

[20] A. Schlange, A.R. dos Santos, B. Hasse, B.J.M. Etzold, U. Kunz, T. Turek, Titanium carbide-derived carbon as a novel support for platinum catalysts in direct methanol fuel cell application, J. Power Sources 199 (2012) 22–28.
[21] R. Ryoo, S.H. Joo, M. Kruk, M. Jaroniec, Ordered mesoporous carbons, Adv. Mater. 13 (2001) 677–681.
[22] J. Ding, K.-Y. Chan, J. Ren, F. Xiao, Platinum and platinum–ruthenium nanoparticles supported on ordered mesoporous carbon and their electrocatalytic performance for fuel cell reactions, Electrochimica Acta 50 (2005) 3131–3141.
[23] H. Yamada, T. Hirai, I. Moriguchi, T. Kudo, A highly active Pt catalyst fabricated on 3D porous carbon, J. Power Sources 164 (2007) 538–543.
[24] E. Antolini, Carbon supports for low-temperature fuel cell catalysts, Appl. Catal. B Environ. 88 (2009) 1–24.
[25] N.M. Marković, R.R. Adžić, B.D. Cahan, E.B. Yeager, Structural effects in electrocatalysis: oxygen reduction on platinum low index single-crystal surfaces in perchloric acid solutions, J. Electroanal. Chem. 377 (1994) 249–259.
[26] U.A. Paulus, T.J. Schmidt, H.A. Gasteiger, R.J. Behm, Oxygen reduction on a high-surface area Pt/Vulcan carbon catalyst: a thin-film rotating ring-disk electrode study, J. Electroanal. Chem. 495 (2001) 134–145.
[27] L. Borchardt, F. Hasché, M.R. Lohe, M. Oschatz, F. Schmidt, E. Kockrick, C. Ziegler, T. Lescouet, A. Bachmatiuk, B. Büchner, D. Farrusseng, P. Strasser, S. Kaskel, Transition metal loaded silicon carbide-derived carbons with enhanced catalytic properties, Carbon 50 (2012) 1861–1870.
[28] F.J. Nores-Pondal, I.M.J. Vilella, H. Troiani, M. Granada, S.R. de Miguel, O.A. Scelza, H.R. Corti, Catalytic activity vs. size correlation in platinum catalysts of PEM fuel cells prepared on carbon black by different methods, Int. J. Hydrog. Energy 34 (2009) 8193–8203.
[29] Z. Liu, X.Y. Ling, X. Su, J.Y. Lee, Carbon-supported Pt and PtRu nanoparticles as catalysts for a direct methanol fuel cell, J Phys Chem B 108 (2004) 8234–8240.
[30] W.-C. Chang, M.T. Nguyen, Investigations of a platinum–ruthenium/carbon nanotube catalyst formed by a two-step spontaneous deposition method, J. Power Sources 196 (2011) 5811–5816.
[31] M. Tsuji, M. Kubokawa, R. Yano, N. Miyamae, T. Tsuji, M.-S. Jun, S. Hong, S. Lim, S.-H. Yoon, I. Mochida, Fast preparation of PtRu catalysts supported on carbon nanofibers by the microwave-polyol method and their application to fuel cells, Langmuir 23 (2006) 387–390.
[32] Z. Liu, X. Zhang, S. Tay, Nanostructured PdRu/C catalysts for formic acid oxidation, J. Solid State Electrochem. 16 (2012) 545–550.
[33] Z.-B. Wang, C.-R. Zhao, P.-F. Shi, Y.-S. Yang, Z.-B. Yu, W.-K. Wang, G.-P. Yin, Effect of a carbon support containing large mesopores on the performance of a Pt−Ru−Ni/C catalyst for direct methanol fuel cells, J. Phys. Chem. C 114 (2010) 672–677.
[34] J.-Y. Woo, K.-M. Lee, B.-C. Jee, C.-H. Ryu, C.-H. Yoon, J.-H. Chung, Y.-R. Kim, S.-B. Moon, A.-S. Kang, Electrocatalytic characteristics of Pt–Ru–Co and Pt–Ru–Ni based on covalently cross-linked sulfonated poly(ether ether ketone)/heteropolyacids composite membranes for water electrolysis, J. Ind. Eng. Chem. 16 (2010) 688–697.
[35] A. Freund, J. Lang, T. Lehmann, K.A. Starz, Improved Pt alloy catalysts for fuel cells, Catal. Today 27 (1996) 279–283.

[36] A. Seo, J. Lee, K. Han, H. Kim, Performance and stability of Pt-based ternary alloy catalysts for PEMFC, Electrochimica Acta 52 (2006) 1603–1611.
[37] J. Luo, N. Kariuki, L. Han, L. Wang, C.-J. Zhong, T. He, Preparation and characterization of carbon-supported PtVFe electrocatalysts, Electrochimica Acta 51 (2006) 4821–4827.
[38] G.S. Chai, S.B. Yoon, J.-S. Yu, J.-H. Choi, Y.-E. Sung, Ordered porous carbons with tunable pore sizes as catalyst supports in direct methanol fuel cell, J Phys Chem B 108 (2004) 7074–7079.
[39] S. Gottesfeld, I.D. Raistrick, S. Srinivasan, Oxygen reduction kinetics on a platinum RDE coated with a recast Nafion film, J. Electrochem. Soc. 134 (1987) 1455–1462.
[40] N.A. Anastasijević, Z.M. Dimitrijević, R.R. Adžić, Oxygen reduction on a ruthenium electrode in alkaline electrolytes, J. Electroanal. Chem. Interfacial Electrochem. 199 (1986) 351–364.
[41] N.A. Anastasijević, Z.M. Dimitrijević, R.R. Adžić, Oxygen reduction on a ruthenium electrode in acid electrolytes, Electrochimica Acta 31 (1986) 1125–1130.
[42] H. Inoue, S.R. Brankovic, J.X. Wang, R.R. Adžić, Oxygen reduction on bare and Pt monolayer-modified Ru(0001), Ru(10$\bar{1}$0) and Ru nanostructured surfaces, Electrochimica Acta 47 (2002) 3777–3785.
[43] K. Sasaki, Y. Mo, J.X. Wang, M. Balasubramanian, F. Uribe, J. McBreen, R.R. Adzic, Pt submonolayers on metal nanoparticles—novel electrocatalysts for H_2 oxidation and O_2 reduction, Electrochimica Acta 48 (2003) 3841–3849.
[44] V. Climent, N.M. Marković, P.N. Ross, Kinetics of oxygen reduction on an epitaxial film of palladium on Pt(111), J Phys Chem B 104 (2000) 3116–3120.
[45] S. Mukerjee, S. Srinivasan, M.P. Soriaga, J. McBreen, Role of structural and electronic properties of Pt and Pt alloys on electrocatalysis of oxygen reduction An in situ XANES and EXAFS investigation, J. Electrochem. Soc. 142 (1995) 1409–1422.
[46] T. Toda, H. Igarashi, M. Watanabe, Enhancement of the electrocatalytic O_2 reduction on Pt–Fe alloys, J. Electroanal. Chem. 460 (1999) 258–262.
[47] B. Hammer, J.K. Nørskov, Theoretical surface science and catalysis—calculations and concepts, in: H.K. Bruce C. Gates (Eds.), Adv. Catal., Academic Press, 2000: pp. 71–129.
[48] M.J.-F. Guinel, A. Bonakdarpour, B. Wang, P.K. Babu, F. Ernst, N. Ramaswamy, S. Mukerjee, A. Wieckowski, Carbon-supported, Selenium-modified Ruthenium–Molybdenum catalysts for Oxygen reduction in acidic media, ChemSusChem 2 (2009) 658–664.
[49] N. Tsiouvaras, M.V. Martínez-Huerta, O. Paschos, U. Stimming, J.L.G. Fierro, M.A. Peña, PtRuMo/C catalysts for direct methanol fuel cells: Effect of the pretreatment on the structural characteristics and methanol electrooxidation, Int. J. Hydrog. Energy 35 (2010) 11478–11488.
[50] B.N. Grgur, N.M. Markovic, P.N. Ross, Electrooxidation of H_2, CO, and H_2/CO mixtures on a well-characterized $Pt_{70}Mo_{30}$ bulk alloy electrode, J. Phys. Chem. B 102 (1998) 2494–2501.
[51] Y. Ishikawa, M.-S. Liao, C.R. Cabrera, Oxidation of methanol on platinum, ruthenium and mixed Pt–M metals (M=Ru, Sn): a theoretical study, Surf. Sci. 463 (2000) 66–80.

[52] M.T.M. Koper, T.E. Shubina, R.A. van Santen, Periodic density functional study of CO and OH adsorption on Pt−Ru alloy surfaces: Implications for CO tolerant fuel cell catalysts, J. Phys. Chem. B 106 (2002) 686–692.
[53] M.-S. Liao, C.R. Cabrera, Y. Ishikawa, A theoretical study of CO adsorption on Pt, Ru and Pt–M (M=Ru, Sn, Ge) clusters, Surf. Sci. 445 (2000) 267–282.
[54] M. Watanabe, S. Motoo, Electrocatalysis by ad-atoms: Part III. Enhancement of the oxidation of carbon monoxide on platinum by ruthenium ad-atoms, J. Electroanal. Chem. Interfacial Electrochem. 60 (1975) 275–283.
[55] B.E. Conway, Electrochemical supercapacitors: scientific fundamentals and technological applications, Plenum, New York, 1999.
[56] S. Hadži-Jordanov, H. Angerstein-Kozlowska, B.E. Conway, Surface oxidation and H deposition at ruthenium electrodes: Resolution of component processes in potential-sweep experiments, J. Electroanal. Chem. Interfacial Electrochem. 60 (1975) 359–362.
[57] S. Trasatti, G. Buzzanca, Electrode material. Solid state structure and electrochemical behaviour, J. Electroanal. Chem. 29 (1971) 1–5.
[58] T. Liu, W.G. Pell, B.E. Conway, Self-discharge and potential recovery phenomena at thermally and electrochemically prepared RuO_2 supercapacitor electrodes, Electrochimica Acta 42 (1997) 3541–3552.
[59] T. Arikado, C. Iwakura, H. Tamura, Electrochemical behaviour of the ruthenium oxide electrode prepared by the thermal decomposition method, Electrochimica Acta 22 (1977) 513–518.
[60] H.A. Gasteiger, S.S. Kocha, B. Sompalli, F.T. Wagner, Activity benchmarks and requirements for Pt, Pt-alloy, and non-Pt oxygen reduction catalysts for PEMFCs, Appl. Catal. B Environ. 56 (2005) 9–35.
[61] L.D. Burke, E.J.M. O'Sullivan, Oxygen gas evolution on hydrous oxides — An example of three-dimensional electrocatalysis?, J. Electroanal. Chem. Interfacial Electrochem. 117 (1981) 155–160.
[62] L.D. Burke, O.J. Murphy, Cyclic voltammetry as a technique for determining the surface area of RuO_2 electrodes, J. Electroanal. Chem. Interfacial Electrochem. 96 (1979) 19–27.
[63] M. Van Brussel, G. Kokkinidis, I. Vandendael, C. Buess-Herman, High performance gold-supported platinum electrocatalyst for oxygen reduction, Electrochem. Commun. 4 (2002) 808–813.
[64] N.M. Markovic, H.A. Gasteiger, P.N. Ross, Oxygen reduction on platinum low-index single-crystal surfaces in sulfuric acid solution: Rotating ring-Pt(*hkl*) disk studies, J. Phys. Chem. 99 (1995) 3411–3415.
[65] M.D. Maciá, J.M. Campiña, E. Herrero, J.M. Feliu, On the kinetics of oxygen reduction on platinum stepped surfaces in acidic media, J. Electroanal. Chem. 564 (2004) 141–150.
[66] A. Kuzume, E. Herrero, J.M. Feliu, Oxygen reduction on stepped platinum surfaces in acidic media, J. Electroanal. Chem. 599 (2007) 333–343.
[67] R.E. Davis, G.L. Horvath, C.W. Tobias, The solubility and diffusion coefficient of oxygen in potassium hydroxide solutions, Electrochimica Acta 12 (1967) 287–297.
[68] Y. Gogotsi, Ed., Carbide-Derived Carbon, in: Nanomaterials Handbook, CRC Press, Boca Raton, 2006: pp. 250–293.

[69] Y. Gogotsi, A. Nikitin, H. Ye, W. Zhou, J.E. Fischer, B. Yi, H.C. Foley, M.W. Barsoum, Nanoporous carbide-derived carbon with tunable pore size, Nat. Mater. 2 (2003) 591–594.
[70] A. Jänes, T. Thomberg, H. Kurig, E. Lust, Nanoscale fine-tuning of porosity of carbide-derived carbon prepared from molybdenum carbide, Carbon 47 (2009) 23–29.
[71] T. Thomberg, H. Kurig, A. Jänes, E. Lust, Mesoporous carbide-derived carbons prepared from different chromium carbides, Microporous Mesoporous Mater. 141 (2011) 88–93.
[72] J.U. Keller, R. Staudt, Adsorption isotherms, in: Gas Adsorption Equilibria, Springer US, 2005: pp. 359–413.
[73] F. Rouquerol, J. Rouquerol, K. Sing, Chapter 7 – Assessment of Mesoporosity, in: F. Rouquerol, J. Rouquerol, K. Sing (Eds.), Adsorptin by Powders Porous Solids, Academic Press, London, 1999: pp. 191–217.
[74] F. Rouquerol, J. Rouquerol, K. Sing, Chapter 1 – Introduction, in: F. Rouquerol, J. Rouquerol, K. Sing (Eds.), Adsorption by Powders Porous Solids, Academic Press, London, 1999: pp. 1–26.
[75] Practical Approaches of Pure Component Adsorption Equilibria, in: Adsorption Analysis: Equilibria and Kinetics, Imperial College Press, 1998: pp. 49–148.
[76] K.S.W. Sing, Reporting physisorption data for gas/solid systems with special reference to the determination of surface area and porosity (Recommendations 1984), Pure Appl. Chem. 57 (1985) 603–619.
[77] S. Brunauer, P.H. Emmett, E. Teller, Adsorption of gases in multimolecular layers, J Am Chem Soc 60 (1938) 309–319.
[78] F. Rouquerol, J. Rouquerol, K. Sing, Chapter 6 – Assessment of Surface Area, in: F. Rouquerol, J. Rouquerol, K. Sing (Eds.), Adsorption by Powders Porous Solids, Academic Press, London, 1999: pp. 165–189.
[79] S. Lowell, J.E. Shields, M.A. Thomas, M. Thommes, Surface Area Analysis from the Langmuir and BET Theories, in: Characterization of Porous Solids and Powders: Surface Area, Pore Size and Density, Springer Netherlands, 2004: pp. 58–81.
[80] S. Lowell, J.E. Shields, M.A. Thomas, M. Thommes, Mesopore Analysis, in: Characterization of Porous Solids and Powders: Surface Area, Pore Size and Density, Springer Netherlands, 2004: pp. 101–128.
[81] P.A. Webb, C. Orr, M.I. Corporation, Analytical methods in fine particle technology, Micromeritics Instrument Corporation, 1997.
[82] S. Lowell, J.E. Shields, M.A. Thomas, M. Thommes, Micropore Analysis, in: Characterization of Porous Solids and Powders: Surface Area, Pore Size and Density, Springer Netherlands, 2004: pp. 129–156.
[83] S. Lowell, J.E. Shields, M.A. Thomas, M. Thommes, Adsorption Mechanism, in: Characterization of Porous Solids and Powders: Surface Area, Pore Size and Density, Springer Netherlands, 2004: pp. 15–57.
[84] D.A. Skoog, F.J. Holler, T.A. Nieman, Principles of instrumental analysis., Saunders College Pub., Philadelphia; London, 1998.
[85] P.E.J. Flewitt, R.K. Wild, Physical Methods for Materials Characterisation, 2th ed., Taylor & Francis, 2003.
[86] A.L. Patterson, The Scherrer Formula for X-Ray Particle Size Determination, Phys. Rev. 56 (1939) 978–982.

[87] A.C. Ferrari, J. Robertson, Interpretation of Raman spectra of disordered and amorphous carbon, Phys. Rev. B 61 (2000) 14095–14107.
[88] S. Urbonaite, L. Hälldahl, G. Svensson, Raman spectroscopy studies of carbide derived carbons, Carbon 46 (2008) 1942–1947.
[89] B. Bhushan, Ed., Springer Handbook of Nanotechnology, Springer, Heidelberg, Germany, 2010.
[90] R.F. Egerton, Electron Energy-Loss Spectroscopy in the Electron Microscope, Springer, 1996.
[91] F. Scholz, Electroanalytical Methods: Guide to Experiments and Applications, Springer, 2009.
[92] C.M.A. Brett, A.M.O. Brett, Electrochemistry: Principles, Methods, and Applications, Oxford University Press, Incorporated, 1993.
[93] A.J. Bard, L.R. Faulkner, Electrochemical Methods, 2nd ed., Wiley, New York, 2001.
[94] E. Gileadi, Electrode Kinetics for Chemists, Chemical Engineers and Materials Scientists, Wiley, 1993.
[95] V.S. Bagotsky, Fundamentals of Electrochemistry, John Wiley & Sons, 2005.
[96] T.J. Schmidt, Characterization of high-surface-area electrocatalysts using a rotating disk electrode configuration, J. Electrochem. Soc. 145 (1998) 2354.
[97] T. Thomberg, A. Jänes, E. Lust, Energy and power performance of vanadium carbide derived carbon electrode materials for supercapacitors, J. Electroanal. Chem. 630 (2009) 55–62.
[98] K. Vaarmets, J. Nerut, E. Härk, E. Lust, Electrochemical and physical characterisation of Pt-nanocluster activated molybdenum carbide derived carbon electrodes, Electrochimica Acta 104 (2013) 216–227.
[99] E. Lust, K. Vaarmets, J. Nerut, I. Tallo, P. Valk, S. Sepp, E. Härk, Influence of specific surface area and microporosity-mesoporosity of pristine and Pt-nanoclusters modified carbide derived carbon electrodes on the oxygen electroreduction, Electrochimica Acta (2014) doi:10.1016/j.electacta.2014.04.054.
[100] P.I. Ravikovitch, A.V. Neimark, Characterization of nanoporous materials from adsorption and desorption isotherms, Colloids Surf. Physicochem. Eng. Asp. 187–188 (2001) 11–21.
[101] Fundamentals of Pure Component Adsorption Equilibria, in: Adsorption Analysis: Equilibria and Kinetics, Imperial College Press, 1998: pp. 11–48.
[102] K. Siegbahn, C. Nordling, G. Johansson, J. Hedman, P.F. Hedén, K. Hamrin, U. Gelius, T. Bergmark, L.O. Werme, R. Manne, Y. Bear, ESCA-Applied to Free Molecules, North-Holland, Amsterdam, 1969.
[103] P.S. Bagus, C. Wőll, A. Wieckowski, Dependence of surface properties on adsorbate-substrate distance: Work function changes and binding energy shifts for I/Pt(111), Surf. Sci. 603 (2009) 273–283.
[104] C.J. Corcoran, H. Tavassol, M.A. Rigsby, P.S. Bagus, A. Wieckowski, Application of XPS to study electrocatalysts for fuel cells, J. Power Sources 195 (2010) 7856–7879.
[105] E. Härk, J. Nerut, K. Vaarmets, I. Tallo, H. Kurig, J. Eskusson, K. Kontturi, E. Lust, Electrochemical impedance characteristics and electroreduction of oxygen at tungsten carbide derived micromesoporous carbon electrodes, J. Electroanal. Chem. 689 (2013) 176–184.

[106] E. Lust, E. Härk, J. Nerut, K. Vaarmets, Pt and Pt–Ru catalysts for polymer electrolyte fuel cells deposited onto carbide-derived carbon supports, Electrochimica Acta 101 (2013) 130–141.
[107] E. Härk, S. Sepp, P. Valk, K. Vaarmets, J. Nerut, R. Jäger, E. Lust, Impact of the various catalysts (Pt, Pt-Ru) deposited onto carbon support to the slow oxygen reduction reaction kinetics, ECS Trans. 45 (2013) 1–11.
[108] S. Sepp, E. Härk, P. Valk, K. Vaarmets, J. Nerut, R. Jäger, E. Lust, Impact of the Pt catalyst on the oxygen electroreduction reaction kinetics on various carbon supports, J. Solid State Electrochem. 18 (2014) 1223–1229.
[109] G. Álvarez, F. Alcaide, O. Miguel, L. Calvillo, M. Lázaro, J. Quintana, J. Calderón, E. Pastor, Technical electrodes catalyzed with PtRu on mesoporous ordered carbons for liquid direct methanol fuel cells, J. Solid State Electrochem. 14 (2010) 1027–1034.
[110] R. Giorgi, P. Ascarelli, S. Turtù, V. Contini, Nanosized metal catalysts in electrodes for solid polymeric electrolyte fuel cells: an XPS and XRD study, Appl. Surf. Sci. 178 (2001) 149–155.
[111] M.E. Orazem, N. Pébère, B. Tribollet, Enhanced graphical representation of electrochemical impedance data, J. Electrochem. Soc. 153 (2006) B129.
[112] V. Lakshminarayanan, R. Srinivasan, D. Chu, S. Gilman, Area determination in fractal surfaces of Pt and Pt-Ru electrodes, Surf. Sci. 392 (1997) 44–51.
[113] S. Mukerjee, S. Srinivasan, Enhanced electrocatalysis of oxygen reduction on platinum alloys in proton exchange membrane fuel cells, J. Electroanal. Chem. 357 (1993) 201–224.
[114] U.A. Paulus, T.J. Schmidt, H.A. Gasteiger, R.J. Behm, Oxygen reduction on a high-surface area Pt/Vulcan carbon catalyst: a thin-film rotating ring-disk electrode study, J. Electroanal. Chem. 495 (2001) 134–145.
[115] B. Wang, Recent development of non-platinum catalysts for oxygen reduction reaction, J. Power Sources 152 (2005) 1–15.
[116] S. Fiechter, I. Dorbandt, P. Bogdanoff, G. Zehl, H. Schulenburg, H. Tributsch, M. Bron, J. Radnik, M. Fieber-Erdmann, Surface modified ruthenium nanoparticles: Structural investigation and surface analysis of a novel catalyst for oxygen reduction, J Phys Chem C 111 (2006) 477–487.
[117] S. Mukerjee, J. McBreen, Effect of particle size on the electrocatalysis by carbon-supported Pt electrocatalysts: an in situ XAS investigation, J. Electroanal. Chem. 448 (1998) 163–171.
[118] P. Hernández-Fernández, S. Rojas, P. Ocón, J.L. Gómez de la Fuente, J. San Fabián, J. Sanza, M.A. Peña, F.J. García-García, P. Terreros, J.L.G. Fierro, Influence of the preparation route of bimetallic Pt−Au nanoparticle electrocatalysts for the oxygen reduction reaction, J Phys Chem C 111 (2007) 2913–2923.
[119] V.M.-W. Huang, V. Vivier, M.E. Orazem, N. Pébère, B. Tribollet, The apparent constant-phase-element behavior of a disk electrode with faradaic reactions, J. Electrochem. Soc. 154 (2007) C99.
[120] B. Hirschorn, M.E. Orazem, B. Tribollet, V. Vivier, I. Frateur, M. Musiani, Determination of effective capacitance and film thickness from constant-phase-element parameters, Electrochimica Acta 55 (2010) 6218–6227.
[121] D. Galizzioli, F. Tantardini, S. Trasatti, Ruthenium dioxide: a new electrode material. I. Behaviour in acid solutions of inert electrolytes, J. Appl. Electrochem. 4 (1974) 57–67.

[122] J.B. Goodenough, Progress in Solid State Chemistry, Reiss H (Ed.), Pergamon, New York, 1971.
[123] H. Schäfer, G. Schneidereit, W. Gerhardt, Zur Chemie der Platinmetalle. RuO_2 Chemischer Transport, Eigenschaften, thermischer Zerfall, Z. Für Anorg. Allg. Chem. 319 (1963) 327–336.
[124] S. Hadži-Jordanov, H. Angerstein-Kozlowska, M. Vukovic, B.E. Conway, Reversibility and growth behavior of surface oxide films at ruthenium electrodes, J. Electrochem. Soc. 125 (1978) 1471–1480.
[125] E. Lust, G. Nurk, A. Jänes, M. Arulepp, P. Nigu, P. Möller, S. Kallip, V. Sammelselg, Electrochemical properties of nanoporous carbon electrodes in various nonaqueous electrolytes, J. Solid State Electrochem. 7 (2003) 91–105.
[126] A. Jänes, L. Permann, M. Arulepp, E. Lust, Electrochemical characteristics of nanoporous carbide-derived carbon materials in non-aqueous electrolyte solutions, Electrochem. Commun. 6 (2004) 313–318.
[127] E. Antolini, F. Cardellini, Formation of carbon supported PtRu alloys: An XRD analysis, J. Alloys Compd. 315 (2001) 118–122.
[128] S. Ardizzone, G. Fregonara, S. Trasatti, "Inner" and "outer" active surface of RuO_2 electrodes, Electrochimica Acta 35 (1990) 263–267.
[129] A. Sarapuu, S. Kallip, A. Kasikov, L. Matisen, K. Tammeveski, Electroreduction of oxygen on gold-supported thin Pt films in acid solutions, J. Electroanal. Chem. 624 (2008) 144–150.
[130] A. Damjanovic, M.A. Genshaw, Dependence of the kinetics of O_2 dissolution at Pt on the conditions for adsorption of reaction intermediates, Electrochimica Acta 15 (1970) 1281–1283.
[131] M. Tarasevich, Investigation of the parallel-consecutive stage of oxygen and hydrogen peroxide reaction. Mechanism of oxygen electroreduction at platinum metals, Elektrokimiya 5 (1973) 599–605.
[132] B.V. Tilak, C.-P. Chen, V.I. Birss, J. Wang, Capacitive and kinetic characteristics of Ru-Ti oxide electrodes: influence of variation in the Ru content, Can. J. Chem. 75 (1997) 1773–1782.
[133] J. Eskusson, A. Jänes, A. Kikas, L. Matisen, E. Lust, Physical and electro-chemical characteristics of supercapacitors based on carbide derived carbon electrodes in aqueous electrolytes, J. Power Sources 196 (2011) 4109–4116.
[134] A. Jänes, T. Thomberg, E. Lust, Synthesis and characterisation of nanoporous carbide-derived carbon by chlorination of vanadium carbide, Carbon 45 (2007) 2717–2722.
[135] J.R. Macdonald, Impedance spectroscopy emphasizing solid materials and systems, Wiley, New York, 1987.
[136] V. Khomenko, E. Raymundo-Piñero, E. Frackowiak, F. Béguin, High-voltage asymmetric supercapacitors operating in aqueous electrolyte, Appl. Phys. Mater. Sci. Process. 82 (2006) 567–573.
[137] K. Fic, G. Lota, E. Frackowiak, Electrochemical properties of supercapacitors operating in aqueous electrolyte with surfactants, Electrochimica Acta 55 (2010) 7484–7488.
[138] A. Lasia, On the mechanism of the hydrogen absorption reaction, J. Electroanal. Chem. 593 (2006) 159–166.
[139] S. Strbac, The effect of pH on oxygen and hydrogen peroxide reduction on polycrystalline Pt electrode, Electrochimica Acta 56 (2011) 1597–1604.

9. SUMMARY IN ESTONIAN

Hapniku elektroredutseerumisreaktsiooni uurimine molübdeenkarbiidist pärineval modifitseerimata ja modifitseeritud süsinikul ning sünteesitud materjalide elektrokeemiline ja füüsikaline karakteriseerimine

Polümeerelektrolüütmembraan-kütuseelement (PEMFC) on paljutõotavaks energiaallikaks portatiivsetes ja statsionaarsetes seadmetes. PEMFC on kõrge kasuteguri ja madala keskkonnareostusega ning töötab suhteliselt madalatel temperatuuridel. PEMFC efektiivsust enim piiravaks teguriks on hapniku redutseerumise reaktsiooni (ORR) aeglus katoodil. Seetõttu on paljud uurimustööd suunatud uute ORR katalüsaatorite arendamisele. ORR katoodse ülepinge vähendamiseks on erinevaid süsinikmaterjale aktiveeritud plaatina, plaatina-ruteeniumi ja teiste Pt-metallide sulamite ning d-metallide (Ni, Co, Fe, Cr) nanoklastritega.

Käesoleva töö eesmärgiks oli uurida Pt ja Pt-Ru sulamist katalüsaatorite alusmaterjali omaduste mõju ORR kineetikale 0,5 M H_2SO_4 vesilahuses. Katalüsaatori nanoosakeste kandjana kasutati Mo_2C pulbrist kuuel kloreerimistemperatuuril vahemikus 600 kuni 1000 °C sünteesitud mikro-mesopoorset süsinikmaterjali. Tulemusi võrreldi kommertsiaalsest süsinikkandjast Vulcan® XC72 valmistatud elektroodi andmetega.

Uuritud materjalide füüsikaliseks karakteriseerimiseks kasutati röntgenstruktuuranalüüsi, röntgenfotoelektronspektroskoopia, Raman spektroskoopia jt meetodeid. Materjalide morfoloogia ja süsiniku elektronkonfiguratsiooni määramiseks kasutati kõrglahutusega transmissioon-elektronmikroskoopiat (HRTEM) koos elektronide energiakao spektroskoopia ja valitud alalt elektronide difraktsiooni meetoditega. Pinna topograafia uurimiseks rakendati skaneerivat elektronmikroskoopiat. HRTEM analüüs näitas, et Pt ja Pt-Ru nanoosakesed moodustavad pinnal aglomeraate ning sadenemine süsinikust alusmaterjali pinnale on toimunud ühtlaselt. Materjali poorsus ja eripind määrati lämmastiku adsorptsiooni mõõtmistest ning tulemustest järeldus, et sünteesitemperatuur mõjutab oluliselt materjalide eripinda ning poorijaotust.

Elektrokeemiliseks karakteriseerimiseks kasutati tsüklilise voltamperomeetria, pöörleva ketaselektroodi ja elektrokeemilise impedantsi spektroskoopia meetodeid.

Tsüklilise voltamperomeetria ja pöörleva ketaselektroodi meetodil mõõdetud andmetest tuleneb, et Mo_2C-st sünteesitud modifitseerimata süsiniku elektrokeemiline aktiivsus on palju suurem kui kommertsiaalsel Vulcan® XC72 süsinikul. Leiti, et Koutecky-Levich'i meetodil arvutatud üleminevate elektronide arv ($2.3 \leq n \leq 3.3$) sõltub süsinikmaterjali mikro-mesopoorsusest ja struktuurist. Lisaks leiti, et süsinikmaterjali suur eripind, kristallilisus ja morfoloogia mõjutavad oluliselt ORR kineetikat, isegi kui erineval temperatuuril (vahemikus 600 °C $\leq t_{synt} \leq$ 850 °C) sünteesitud süsinikmaterjalide eripindade erinevus on väike. Katalüütilise aktiivsuse tõstmiseks modifitseeriti karbiidset

päritolu mikro-mesopoorset süsinikku plaatina nanoosakestega boorhüdriidiga redutseerimise meetodil. Elektrokeemilistest mõõtmistest võib järeldada, et süsinikkandjale sadestatud Pt-nanoosakese suurus sõltub oluliselt alusmaterjali miko-mesopoorsusest ja kristallilisusest. Pöörleva ketaselektroodi meetodil mõõdetud andmetest järeldub, et Pt-C(Mo_2C)800 °C elektroodil on kõige kõrgemad katoodse voolutiheduse väärtused. Koutecky-Levich'i meetodil arvutatud üleminevate elektronide arv varieerub vahemikus 3.3 kuni 3.7 ja on kooskõlas kirjanduse andmetega. Tsüklilise voltamperomeetria andmetest arvutati elektrikeemiliselt aktiivse eripinna suurus, mis on kõige kõrgem (14–30 m^2g^{-1}) Pt-C(Mo_2C)750 °C, Pt-C(Mo_2C)800 °C ja Pt-C(Mo_2C)850 °C elektroodide korral.

Tsüklilise voltamperomeetria ja pöörleva ketaselektroodi meetoditel mõõdetud andmetest Pt-Ru-C(Mo_2C) 600 °C katalüsaatori materjali kohta võib järeldada, et mõõdetud ORR ja elektrilise kaksikkihi voolutiheduse väärtused on väga kõrged. Koutecky-Levich'i meetodil arvutatud üleminevate elektronide arv on ligikaudu 4.

Elektrokeemilise impedantsspektroskoopia andmetest leitud suured paralleel- ja järjestikmahtuvused annavad põhjendatud lootust, et plaatina ja ruteeniumiga aktiveeritud süsinikmaterjalid pakkuvad huvi ka kõrge energiatihedusega superkondensaatorite valmistamisel.

10. ACKNOWLEDGEMENTS

Author thank Thomas Thomberg and Indrek Tallo for synthesising the CDC powders, Mr. J. Aruväli and Prof. K. Kirsimägi for performing XRD and XRF measurements, prof. K. Kontturi from Department of Chemistry and Dr. J. Hua from Department of Applied Physics at Aalto University School of Science for HRTEM measurements, Dr. Ilmo Sildos from Institute of Physics at University of Tartu for the Raman studies and H. Kurig and R. Palm for the low temperature N_2 sorption experiments.

This work was supported by Estonian target research project SF0180002s08, institutional research funding IUT (IUT 20-13) of the Estonian Ministry of Education and Research, Estonian Centre of Excellence in Research Project 3.20101.11-0030 "High-technology Materials for Sustainable Development", Estonian Energy Technology Programme project 3.2.0501.10-0015, Estonian Materials Technology project 3.2.1101.12-0019, Grant ETF8267 and graduate school "Functional materials and technologies" receiving funding from the European Social Fund under project 1.2.0401.09-0079 in Estonia.

11. PUBLICATIONS

CURRICULUM VITAE

Name: Kersti Vaarmets
Date of birth: November 24, 1984
Citizenship: Estonian
Contact: Institute of Chemistry, Faculty of Science and Technology, University of Tartu
14a Ravila Street, 50411 Tartu, Estonia
E-mail: kersti.vaarmets@ut.ee

Education:

1992–2004	Rakvere Real Gymnasium
2004–2007	University of Tartu – Bachelor's degree in chemistry
2007–2009	University of Tartu – Master's degree in chemistry
2009–2014	University of Tartu, Institute of Chemistry, PhD student

Professional employment:

2006–2013	University of Tartu, Institute of Chemistry, technician
2013–2014	University of Tartu, Institute of Chemistry, junior research fellow

List of Publications:

K. Vaarmets, S. Sepp, J. Nerut, E. Härk, I. Tallo, E. Lust, Electrochemical and physical characterization of Pt–Ru alloy catalyst deposited onto microporous–mesoporous carbon support derived from Mo_2C at 600 °C, Journal of Solid State Electrochemistry 17 (2013) 1729.

K. Vaarmets, J. Nerut, E. Härk, E. Lust, Electrochemical and physical characterisation of Pt-nanocluster activated molybdenum carbide-derived carbon electrodes, Electrochimica Acta 104 (2013) 216.

E. Lust, K. Vaarmets, J. Nerut, I. Tallo, H. Kurgi, P.Valk, E. Härk, Influence of specific surface area and microporosity-mesoporosity of pristine and Pt-nanoclusters modified carbide-derived carbon electrodes on the oxygen electroreduction, Electrochimica Acta (2014) DOI:10.1016/j.electacta.2014.04.054.

E. Härk, J. Nerut, K. Vaarmets, I. Tallo, H. Kurig, J. Eskusson, K. Kontturi, E. Lust, Electrochemical impedance characteristics and electroreduction of oxygen at tungsten carbide-derived micromesoporous carbon electrodes, Journal Electroanalytical Chemistry 689 (2013) 176.

E. Lust, E. Härk, J. Nerut, K. Vaarmets, Pt and Pt–Ru catalysts for polymer electrolyte fuel cells deposited onto carbide-derived carbon supports, Electrochimica Acta 101 (2013) 130.

E. Härk, V. Steinberg, S. Sepp, K. Vaarmets, J. Nerut, T. Kallio, K. Kontturi, E. Lust, Electrochemical and physical characterization of Pt activated micromesoporous vanadium carbide-derived carbon electrodes in sulfuric acid solution, Journal Electrochemistry Society 160 (2013) F923.

S. Sepp, E. Härk, P. Valk, K. Vaarmets, J. Nerut, R. Jäger, E. Lust, Impact of the Pt catalyst on the oxygen electroreduction reaction kinetics on various carbon supports, Journal of Solid State Electrochemistry 18 (2014) 1223–1229

E. Härk, S. Sepp, P. Valk, K. Vaarmets, J. Nerut, R. Jäger, E. Lust, Impact of the various catalysts (Pt, Pt-Ru) deposited onto carbon support to the slow oxygen reduction reaction kinetics, ECS Transactions 45 (2013) 1.

ELULOOKIRJELDUS

Nimi: Kersti Vaarmets
Sünniaeg: 24. November 1984
Kodakondsus: Eesti
Kontakt: Keemia Instituut, Loodus- ja tehnoloogiateaduskond,
Tartu Ülikool,
Ravila 14A, 50411 Tartu, Eesti
E-mail: kersti.vaarmets@ut.ee

Haridus:

1992–2004	Rakvere Reaalgümnaasium
2004–2007	Tartu Ülikool – loodusteaduse bakalaureuse kraad (füüsikaline ja elektrokeemia)
2007–2009	Tartu Ülikool – loodusteaduse magistri kraad (füüsikaline ja elektrokeemia)
2009–2014	Tartu Ülikool, Keemia Instituut, doktorant

Töökogemus:

2006–2013	Tartu Ülikool, LOKT, Keemia Instituut, Füüsikalise keemia õppetool, laborant
2013–02014	Tartu Ülikool, LOKT, Keemia Instituut, Füüsikalise keemia õppetool, nooremteadur

Teaduspublikatsioonid:

K. Vaarmets, S. Sepp, J. Nerut, E. Härk, I. Tallo, E. Lust, Electrochemical and physical characterization of Pt–Ru alloy catalyst deposited onto microporous–mesoporous carbon support derived from Mo_2C at 600 °C, Journal of Solid State Electrochemistry 17 (2013) 1729.

K. Vaarmets, J. Nerut, E. Härk, E. Lust, Electrochemical and physical characterisation of Pt-nanocluster activated molybdenum carbide-derived carbon electrodes, Electrochimica Acta 104 (2013) 216.

E. Lust, K. Vaarmets, J. Nerut, I. Tallo, H. Kurgi, P.Valk, E. Härk, Influence of specific surface area and microporosity-mesoporosity of pristine and Pt-nanoclusters modified carbide-derived carbon electrodes on the oxygen electroreduction, Electrochimica Acta (2014) DOI:10.1016/j.electacta.2014.04.054.

E. Härk, J. Nerut, K. Vaarmets, I. Tallo, H. Kurig, J. Eskusson, K. Kontturi, E. Lust, Electrochemical impedance characteristics and electroreduction of oxygen at tungsten carbide-derived micromesoporous carbon electrodes, Journal Electroanalytical Chemistry 689 (2013) 176.

E. Lust, E. Härk, J. Nerut, K. Vaarmets, Pt and Pt–Ru catalysts for polymer electrolyte fuel cells deposited onto carbide-derived carbon supports, Electrochimica Acta 101 (2013) 130.

E. Härk, V. Steinberg, S. Sepp, K. Vaarmets, J. Nerut, T. Kallio, K. Kontturi, E. Lust, Electrochemical and physical characterization of Pt activated micromesoporous vanadium carbide derived carbon electrodes in sulfuric acid solution, Journal Electrochemistry Society 160 (2013) F923.

S. Sepp, E. Härk, P. Valk, K. Vaarmets, J. Nerut, R. Jäger, E. Lust, Impact of the Pt catalyst on the oxygen electroreduction reaction kinetics on various carbon supports, Journal of Solid State Electrochemistry 18 (2014) 1223–1229.

E. Härk, S. Sepp, P. Valk, K. Vaarmets, J. Nerut, R. Jäger, E. Lust, Impact of the various catalysts (Pt, Pt-Ru) deposited onto carbon support to the slow oxygen reduction reaction kinetics, ECS Transactions 45 (2013) 1.

DISSERTATIONES CHIMICAE UNIVERSITATIS TARTUENSIS

1. **Toomas Tamm.** Quantum-chemical simulation of solvent effects. Tartu, 1993, 110 p.
2. **Peeter Burk.** Theoretical study of gas-phase acid-base equilibria. Tartu, 1994, 96 p.
3. **Victor Lobanov.** Quantitative structure-property relationships in large descriptor spaces. Tartu, 1995, 135 p.
4. **Vahur Mäemets.** The ^{17}O and ^{1}H nuclear magnetic resonance study of H_2O in individual solvents and its charged clusters in aqueous solutions of electrolytes. Tartu, 1997, 140 p.
5. **Andrus Metsala.** Microcanonical rate constant in nonequilibrium distribution of vibrational energy and in restricted intramolecular vibrational energy redistribution on the basis of slater's theory of unimolecular reactions. Tartu, 1997, 150 p.
6. **Uko Maran.** Quantum-mechanical study of potential energy surfaces in different environments. Tartu, 1997, 137 p.
7. **Alar Jänes.** Adsorption of organic compounds on antimony, bismuth and cadmium electrodes. Tartu, 1998, 219 p.
8. **Kaido Tammeveski.** Oxygen electroreduction on thin platinum films and the electrochemical detection of superoxide anion. Tartu, 1998, 139 p.
9. **Ivo Leito.** Studies of Brønsted acid-base equilibria in water and non-aqueous media. Tartu, 1998, 101 p.
10. **Jaan Leis.** Conformational dynamics and equilibria in amides. Tartu, 1998, 131 p.
11. **Toonika Rinken.** The modelling of amperometric biosensors based on oxidoreductases. Tartu, 2000, 108 p.
12. **Dmitri Panov.** Partially solvated Grignard reagents. Tartu, 2000, 64 p.
13. **Kaja Orupõld.** Treatment and analysis of phenolic wastewater with microorganisms. Tartu, 2000, 123 p.
14. **Jüri Ivask.** Ion Chromatographic determination of major anions and cations in polar ice core. Tartu, 2000, 85 p.
15. **Lauri Vares.** Stereoselective Synthesis of Tetrahydrofuran and Tetrahydropyran Derivatives by Use of Asymmetric Horner-Wadsworth-Emmons and Ring Closure Reactions. Tartu, 2000, 184 p.
16. **Martin Lepiku.** Kinetic aspects of dopamine D_2 receptor interactions with specific ligands. Tartu, 2000, 81 p.
17. **Katrin Sak.** Some aspects of ligand specificity of P2Y receptors. Tartu, 2000, 106 p.
18. **Vello Pällin.** The role of solvation in the formation of iotsitch complexes. Tartu, 2001, 95 p.

19. **Katrin Kollist.** Interactions between polycyclic aromatic compounds and humic substances. Tartu, 2001, 93 p.
20. **Ivar Koppel.** Quantum chemical study of acidity of strong and superstrong Brønsted acids. Tartu, 2001, 104 p.
21. **Viljar Pihl.** The study of the substituent and solvent effects on the acidity of OH and CH acids. Tartu, 2001, 132 p.
22. **Natalia Palm.** Specification of the minimum, sufficient and significant set of descriptors for general description of solvent effects. Tartu, 2001, 134 p.
23. **Sulev Sild.** QSPR/QSAR approaches for complex molecular systems. Tartu, 2001, 134 p.
24. **Ruslan Petrukhin.** Industrial applications of the quantitative structure-property relationships. Tartu, 2001, 162 p.
25. **Boris V. Rogovoy.** Synthesis of (benzotriazolyl)carboximidamides and their application in relations with *N*- and *S*-nucleophyles. Tartu, 2002, 84 p.
26. **Koit Herodes.** Solvent effects on UV-vis absorption spectra of some solvatochromic substances in binary solvent mixtures: the preferential solvation model. Tartu, 2002, 102 p.
27. **Anti Perkson.** Synthesis and characterisation of nanostructured carbon. Tartu, 2002, 152 p.
28. **Ivari Kaljurand.** Self-consistent acidity scales of neutral and cationic Brønsted acids in acetonitrile and tetrahydrofuran. Tartu, 2003, 108 p.
29. **Karmen Lust.** Adsorption of anions on bismuth single crystal electrodes. Tartu, 2003, 128 p.
30. **Mare Piirsalu.** Substituent, temperature and solvent effects on the alkaline hydrolysis of substituted phenyl and alkyl esters of benzoic acid. Tartu, 2003, 156 p.
31. **Meeri Sassian.** Reactions of partially solvated Grignard reagents. Tartu, 2003, 78 p.
32. **Tarmo Tamm.** Quantum chemical modelling of polypyrrole. Tartu, 2003. 100 p.
33. **Erik Teinemaa.** The environmental fate of the particulate matter and organic pollutants from an oil shale power plant. Tartu, 2003. 102 p.
34. **Jaana Tammiku-Taul.** Quantum chemical study of the properties of Grignard reagents. Tartu, 2003. 120 p.
35. **Andre Lomaka.** Biomedical applications of predictive computational chemistry. Tartu, 2003. 132 p.
36. **Kostyantyn Kirichenko.** Benzotriazole – Mediated Carbon–Carbon Bond Formation. Tartu, 2003. 132 p.
37. **Gunnar Nurk.** Adsorption kinetics of some organic compounds on bismuth single crystal electrodes. Tartu, 2003, 170 p.
38. **Mati Arulepp.** Electrochemical characteristics of porous carbon materials and electrical double layer capacitors. Tartu, 2003, 196 p.

39. **Dan Cornel Fara.** QSPR modeling of complexation and distribution of organic compounds. Tartu, 2004, 126 p.
40. **Riina Mahlapuu.** Signalling of galanin and amyloid precursor protein through adenylate cyclase. Tartu, 2004, 124 p.
41. **Mihkel Kerikmäe.** Some luminescent materials for dosimetric applications and physical research. Tartu, 2004, 143 p.
42. **Jaanus Kruusma.** Determination of some important trace metal ions in human blood. Tartu, 2004, 115 p.
43. **Urmas Johanson.** Investigations of the electrochemical properties of polypyrrole modified electrodes. Tartu, 2004, 91 p.
44. **Kaido Sillar.** Computational study of the acid sites in zeolite ZSM-5. Tartu, 2004, 80 p.
45. **Aldo Oras.** Kinetic aspects of dATPαS interaction with $P2Y_1$ receptor. Tartu, 2004, 75 p.
46. **Erik Mölder.** Measurement of the oxygen mass transfer through the air-water interface. Tartu, 2005, 73 p.
47. **Thomas Thomberg.** The kinetics of electroreduction of peroxodisulfate anion on cadmium (0001) single crystal electrode. Tartu, 2005, 95 p.
48. **Olavi Loog.** Aspects of condensations of carbonyl compounds and their imine analogues. Tartu, 2005, 83 p.
49. **Siim Salmar.** Effect of ultrasound on ester hydrolysis in aqueous ethanol. Tartu, 2006, 73 p.
50. **Ain Uustare.** Modulation of signal transduction of heptahelical receptors by other receptors and G proteins. Tartu, 2006, 121 p.
51. **Sergei Yurchenko.** Determination of some carcinogenic contaminants in food. Tartu, 2006, 143 p.
52. **Kaido Tämm.** QSPR modeling of some properties of organic compounds. Tartu, 2006, 67 p.
53. **Olga Tšubrik.** New methods in the synthesis of multisubstituted hydrazines. Tartu. 2006, 183 p.
54. **Lilli Sooväli.** Spectrophotometric measurements and their uncertainty in chemical analysis and dissociation constant measurements. Tartu, 2006, 125 p.
55. **Eve Koort.** Uncertainty estimation of potentiometrically measured ph and pK_a values. Tartu, 2006, 139 p.
56. **Sergei Kopanchuk.** Regulation of ligand binding to melanocortin receptor subtypes. Tartu, 2006, 119 p.
57. **Silvar Kallip.** Surface structure of some bismuth and antimony single crystal electrodes. Tartu, 2006, 107 p.
58. **Kristjan Saal.** Surface silanization and its application in biomolecule coupling. Tartu, 2006, 77 p.
59. **Tanel Tätte.** High viscosity $Sn(OBu)_4$ oligomeric concentrates and their applications in technology. Tartu, 2006, 91 p.

60. **Dimitar Atanasov Dobchev**. Robust QSAR methods for the prediction of properties from molecular structure. Tartu, 2006, 118 p.
61. **Hannes Hagu**. Impact of ultrasound on hydrophobic interactions in solutions. Tartu, 2007, 81 p.
62. **Rutha Jäger.** Electroreduction of peroxodisulfate anion on bismuth electrodes. Tartu, 2007, 142 p.
63. **Kaido Viht.** Immobilizable bisubstrate-analogue inhibitors of basophilic protein kinases: development and application in biosensors. Tartu, 2007, 88 p.
64. **Eva-Ingrid Rõõm.** Acid-base equilibria in nonpolar media. Tartu, 2007, 156 p.
65. **Sven Tamp.** DFT study of the cesium cation containing complexes relevant to the cesium cation binding by the humic acids. Tartu, 2007, 102 p.
66. **Jaak Nerut.** Electroreduction of hexacyanoferrate(III) anion on Cadmium (0001) single crystal electrode. Tartu, 2007, 180 p.
67. **Lauri Jalukse.** Measurement uncertainty estimation in amperometric dissolved oxygen concentration measurement. Tartu, 2007, 112 p.
68. **Aime Lust.** Charge state of dopants and ordered clusters formation in CaF_2:Mn and CaF_2:Eu luminophors. Tartu, 2007, 100 p.
69. **Iiris Kahn**. Quantitative Structure-Activity Relationships of environmentally relevant properties. Tartu, 2007, 98 p.
70. **Mari Reinik.** Nitrates, nitrites, N-nitrosamines and polycyclic aromatic hydrocarbons in food: analytical methods, occurrence and dietary intake. Tartu, 2007, 172 p.
71. **Heili Kasuk.** Thermodynamic parameters and adsorption kinetics of organic compounds forming the compact adsorption layer at Bi single crystal electrodes. Tartu, 2007, 212 p.
72. **Erki Enkvist.** Synthesis of adenosine-peptide conjugates for biological applications. Tartu, 2007, 114 p.
73. **Svetoslav Hristov Slavov**. Biomedical applications of the QSAR approach. Tartu, 2007, 146 p.
74. **Eneli Härk.** Electroreduction of complex cations on electrochemically polished Bi(*hkl*) single crystal electrodes. Tartu, 2008, 158 p.
75. **Priit Möller.** Electrochemical characteristics of some cathodes for medium temperature solid oxide fuel cells, synthesized by solid state reaction technique. Tartu, 2008, 90 p.
76. **Signe Viggor.** Impact of biochemical parameters of genetically different pseudomonads at the degradation of phenolic compounds. Tartu, 2008, 122 p.
77. **Ave Sarapuu.** Electrochemical reduction of oxygen on quinone-modified carbon electrodes and on thin films of platinum and gold. Tartu, 2008, 134 p.
78. **Agnes Kütt.** Studies of acid-base equilibria in non-aqueous media. Tartu, 2008, 198 p.

79. **Rouvim Kadis.** Evaluation of measurement uncertainty in analytical chemistry: related concepts and some points of misinterpretation. Tartu, 2008, 118 p.
80. **Valter Reedo.** Elaboration of IVB group metal oxide structures and their possible applications. Tartu, 2008, 98 p.
81. **Aleksei Kuznetsov.** Allosteric effects in reactions catalyzed by the cAMP-dependent protein kinase catalytic subunit. Tartu, 2009, 133 p.
82. **Aleksei Bredihhin.** Use of mono- and polyanions in the synthesis of multisubstituted hydrazine derivatives. Tartu, 2009, 105 p.
83. **Anu Ploom.** Quantitative structure-reactivity analysis in organosilicon chemistry. Tartu, 2009, 99 p.
84. **Argo Vonk.** Determination of adenosine A_{2A}- and dopamine D_1 receptor-specific modulation of adenylate cyclase activity in rat striatum. Tartu, 2009, 129 p.
85. **Indrek Kivi.** Synthesis and electrochemical characterization of porous cathode materials for intermediate temperature solid oxide fuel cells. Tartu, 2009, 177 p.
86. **Jaanus Eskusson.** Synthesis and characterisation of diamond-like carbon thin films prepared by pulsed laser deposition method. Tartu, 2009, 117 p.
87. **Marko Lätt.** Carbide derived microporous carbon and electrical double layer capacitors. Tartu, 2009, 107 p.
88. **Vladimir Stepanov.** Slow conformational changes in dopamine transporter interaction with its ligands. Tartu, 2009, 103 p.
89. **Aleksander Trummal.** Computational Study of Structural and Solvent Effects on Acidities of Some Brønsted Acids. Tartu, 2009, 103 p.
90. **Eerold Vellemäe.** Applications of mischmetal in organic synthesis. Tartu, 2009, 93 p.
91. **Sven Parkel.** Ligand binding to 5-HT_{1A} receptors and its regulation by Mg^{2+} and Mn^{2+}. Tartu, 2010, 99 p.
92. **Signe Vahur.** Expanding the possibilities of ATR-FT-IR spectroscopy in determination of inorganic pigments. Tartu, 2010, 184 p.
93. **Tavo Romann**. Preparation and surface modification of bismuth thin film, porous, and microelectrodes. Tartu, 2010, 155 p.
94. **Nadežda Aleksejeva.** Electrocatalytic reduction of oxygen on carbon nanotube-based nanocomposite materials. Tartu, 2010, 147 p.
95. **Marko Kullapere.** Electrochemical properties of glassy carbon, nickel and gold electrodes modified with aryl groups. Tartu, 2010, 233 p.
96. **Liis Siinor.** Adsorption kinetics of ions at Bi single crystal planes from aqueous electrolyte solutions and room-temperature ionic liquids. Tartu, 2010, 101 p.
97. **Angela Vaasa.** Development of fluorescence-based kinetic and binding assays for characterization of protein kinases and their inhibitors. Tartu 2010, 101 p.

98. **Indrek Tulp.** Multivariate analysis of chemical and biological properties. Tartu 2010, 105 p.
99. **Aare Selberg.** Evaluation of environmental quality in Northern Estonia by the analysis of leachate. Tartu 2010, 117 p.
100. **Darja Lavõgina.** Development of protein kinase inhibitors based on adenosine analogue-oligoarginine conjugates. Tartu 2010, 248 p.
101. **Laura Herm.** Biochemistry of dopamine D_2 receptors and its association with motivated behaviour. Tartu 2010, 156 p.
102. **Terje Raudsepp.** Influence of dopant anions on the electrochemical properties of polypyrrole films. Tartu 2010, 112 p.
103. **Margus Marandi.** Electroformation of Polypyrrole Films: *In-situ* AFM and STM Study. Tartu 2011, 116 p.
104. **Kairi Kivirand.** Diamine oxidase-based biosensors: construction and working principles. Tartu, 2011, 140 p.
105. **Anneli Kruve.** Matrix effects in liquid-chromatography electrospray mass-spectrometry. Tartu, 2011, 156 p.
106. **Gary Urb.** Assessment of environmental impact of oil shale fly ash from PF and CFB combustion. Tartu, 2011, 108 p.
107. **Nikita Oskolkov.** A novel strategy for peptide-mediated cellular delivery and induction of endosomal escape. Tartu, 2011, 106 p.
108. **Dana Martin.** The QSPR/QSAR approach for the prediction of properties of fullerene derivatives. Tartu, 2011, 98 p.
109. **Säde Viirlaid.** Novel glutathione analogues and their antioxidant activity. Tartu, 2011, 106 p.
110. **Ülis Sõukand.** Simultaneous adsorption of Cd^{2+}, Ni^{2+}, and Pb^{2+} on peat. Tartu, 2011, 124 p.
111. **Lauri Lipping.** The acidity of strong and superstrong Brønsted acids, an outreach for the "limits of growth": a quantum chemical study. Tartu, 2011, 124 p.
112. **Heisi Kurig.** Electrical double-layer capacitors based on ionic liquids as electrolytes. Tartu, 2011, 146 p.
113. **Marje Kasari.** Bisubstrate luminescent probes, optical sensors and affinity adsorbents for measurement of active protein kinases in biological samples. Tartu, 2012, 126 p.
114. **Kalev Takkis.** Virtual screening of chemical databases for bioactive molecules. Tartu, 2012, 122 p.
115. **Ksenija Kisseljova**. Synthesis of aza-β^3-amino acid containing peptides and kinetic study of their phosphorylation by protein kinase A. Tartu, 2012, 104 p.
116. **Riin Rebane.** Advanced method development strategy for derivatization LC/ESI/MS. Tartu, 2012, 184 p.

117. **Vladislav Ivaništšev.** Double layer structure and adsorption kinetics of ions at metal electrodes in room temperature ionic liquids. Tartu, 2012, 128 p.
118. **Irja Helm.** High accuracy gravimetric Winkler method for determination of dissolved oxygen. Tartu, 2012, 139 p.
119. **Karin Kipper.** Fluoroalcohols as Components of LC-ESI-MS Eluents: Usage and Applications. Tartu, 2012, 164 p.
120. **Arno Ratas.** Energy storage and transfer in dosimetric luminescent materials. Tartu, 2012, 163 p.
121. **Reet Reinart-Okugbeni**. Assay systems for characterisation of subtype-selective binding and functional activity of ligands on dopamine receptors. Tartu, 2012, 159 p.
122. **Lauri Sikk.** Computational study of the Sonogashira cross-coupling reaction. Tartu, 2012, 81 p.
123. **Karita Raudkivi.** Neurochemical studies on inter-individual differences in affect-related behaviour of the laboratory rat. Tartu, 2012, 161 p.
124. **Indrek Saar.** Design of GalR2 subtype specific ligands: their role in depression-like behavior and feeding regulation. Tartu, 2013, 126 p.
125. **Ann Laheäär.** Electrochemical characterization of alkali metal salt based non-aqueous electrolytes for supercapacitors. Tartu, 2013, 127 p.
126. **Kerli Tõnurist.** Influence of electrospun separator materials properties on electrochemical performance of electrical double-layer capacitors. Tartu, 2013, 147 p.
127. **Kaija Põhako-Esko.** Novel organic and inorganic ionogels: preparation and characterization. Tartu, 2013, 124 p.
128. **Ivar Kruusenberg.** Electroreduction of oxygen on carbon nanomaterial-based catalysts. Tartu, 2013, 191 p.
129. **Sander Piiskop.** Kinetic effects of ultrasound in aqueous acetonitrile solutions. Tartu, 2013, 95 p.
130. **Ilona Faustova**. Regulatory role of L-type pyruvate kinase N-terminal domain. Tartu, 2013, 109 p.
131. **Kadi Tamm.** Synthesis and characterization of the micro-mesoporous anode materials and testing of the medium temperature solid oxide fuel cell single cells. Tartu, 2013, 138 p.
132. **Iva Bozhidarova Stoyanova-Slavova.** Validation of QSAR/QSPR for regulatory purposes. Tartu, 2013, 109 p.
133. **Vitali Grozovski**. Adsorption of organic molecules at single crystal electrodes studied by *in situ* STM method. Tartu, 2014, 146 p.
134. **Santa Veikšina**. Development of assay systems for characterisation of ligand binding properties to melanocortin 4 receptors. Tartu, 2014, 151 p.
135. **Jüri Liiv.** PVDF (polyvinylidene difluoride) as material for active element of twisting-ball displays. Tartu, 2014, 111 p.